Modeling and Design for Electrochemical Carbon Dioxide Capture Systems

by

Ryan Alex Shaw

B.S. Chemical Engineering and Mathematics,
Virginia Polytechnic Institute and State University (2012)
M.S. Chemical Engineering Practice,
Massachusetts Institute of Technology (2016)

Submitted to the Department of Chemical Engineering
in partial fulfillment of the requirements for the degree of

Doctor of Philosophy in Chemical Engineering Practice

at the

MASSACHUSETTS INSTITUTE OF TECHNOLOGY

June 2019

Author Signature redacted
Department of Chemical Engineering
May 1, 2019

Certified by Signature redacted
T. Alan Hatton
Ralph Landau Professor of Chemical Engineering
Thesis Supervisor

Accepted by Signature redacted
Patrick S. Doyle
Singapore Research Professor of Chemical Engineering
Chairman, Department Committee on Graduate Theses

Modeling and Design for Electrochemical Carbon Dioxide Capture Systems

by

Ryan Alex Shaw

Submitted to the Department of Chemical Engineering
on May 1, 2019, in partial fulfillment of the
requirements for the degree of
Doctor of Philosophy in Chemical Engineering Practice

Abstract

So long as fossil fuels remain humanity's primary source of energy, carbon dioxide capture and storage will be needed to mitigate the effects of global climate change. Existing carbon dioxide separation technology is energetically intensive and expensive to employ in brownfield applications.

This thesis describes a novel CO_2 capture technology called Electrochemically-Mediated Amine Recovery (EMAR). EMAR modifies incumbent thermal amine scrubbing, by performing an electrochemical desorption which manipulates the concentration of a cupric competitive complexing agent. Oxidizing copper results in a cupric-amine complex at the anode, releasing CO_2. Reducing this complex at the cathode regenerates amines for capture. This approach is more energy efficient than traditional thermal amine processes and is expected to be less capital intensive to implement.

A proof-of-concept EMAR system has been previously demonstrated and initial system optimization has been previously performed. Contained herein is a significant expansion of that work specifically in the areas of thermodynamics, mass and heat transport, and system design.

Three thermodynamic paths are described for the EMAR process, which establish the total electrochemical work of separation for this and other similar molecular architectures. Electrochemical work, in concert with work of compression and pump work, allow for an ideal process flow scheme as well as optimized operating conditions for the EMAR process to be developed. The thermodynamics suggests employing a cathodic absorber for substantial efficiency improvements.

EMAR cell design is significantly improved by transitioning from a single unit cell to a modular, stacked system. Performance of two stack geometries, series and parallel, is modelled and analyzed. It is demonstrated that the series stack, which is more industrially applicable, shows less severe internal temperature gradients than that of the parallel geometry.

Thesis Supervisor: T. Alan Hatton
Title: Ralph Landau Professor of Chemical Engineering

Dedication

For Shady, our best good girl.

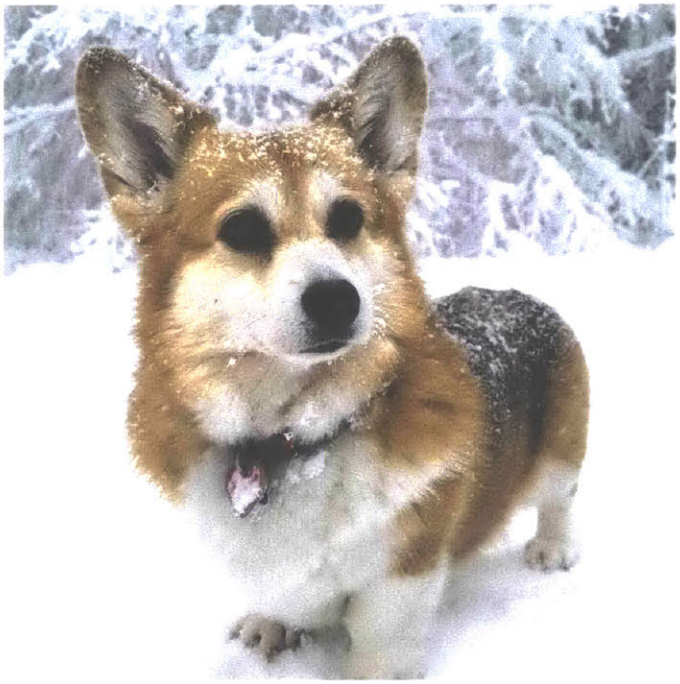

Shady Wiebe Shaw

Acknowledgments

Professor Hatton Professor Hatton has pushed me to be a better engineer and scientist. He has taught me to be more idealistic and made me more open to unique, interesting, and sometimes crazy ideas (some of which are seen in this work). His insistence that I back up my claims with sound chemical engineering principals and that I speak in a more precise manner, forces me to always question my assumptions and has added significantly to the clarity of this work. By working with Dr. Hatton, I feel I have become a better engineer, scientist, and person.

My Committee Drs. Green and Herzog have been a wealth of information and have helped contribute to the success of this work. Professor Green is ever inquisitive and has been a force to keep me in check and ensure I am heading in the right direction. Dr. Herzog is perhaps one of the foremost authorities on CCS and he has helped the EMAR project find its place in a broader CO_2 capture space.

My Labmates It has been a pleasure working with the whole Hatton lab team. In particular, I have had the pleasure of working closely with Sahag Voskian and Miao Wang. Sahag is a brilliant chemist and engineer and I owe much of my understanding of the EMAR process, electrochemistry, and chemistry in general to time spent working with him. On top of that, he is an extremely dedicated coworker and one of the best cooks I know. Miao joined the group at just the right time and has brought an electrochemical rigor not previously seen (and desperately needed) on the EMAR project. He has been a sounding board and adviser for much of the work seen in this thesis, especially the thermodynamics section. Sahag and Miao, it has been an absolute pleasure working with both of you.

My Friends Getting through first year (and the few to follow) would not have been possible, and certainly would not have been as fun, without the friendships that developed early in that process. Catie, Connor, Jennifer, Kassi, Laura, Lisa, Mike, and Nick thank you for all of the homework sessions, friendsgivings, and ski trips. You have made the last five years fly by.

My Family My whole family is owed a debt of gratitude for their patience, love, and support throughout this whole process, without which I am sure I would not have been successful. My parents and grandparents have been a source of love and support and a guiding compass, which has gotten me to this point. My wife, Meg, has shared the good times and the bad times with me for these last seven years. Our little family (Shady included) has kept me sane and loved and for that I am forever grateful. Thank you all so much for your support. I love you.

THIS PAGE INTENTIONALLY LEFT BLANK

Contents

THIS PAGE INTENTIONALLY LEFT BLANK

List of Figures

THIS PAGE INTENTIONALLY LEFT BLANK

List of Tables

Variables Used

Variable	Description	SI Units
A_{max}	Maximum unit cell cross sectional area	m^2
A_{mem}	Membrane area required	m^2
Am_0	Total amine concentration, $Am_0 = C_{Am} + C_{Am(CO_2)_m} + \frac{2}{m}C_{Cu^{II}Am^{2+}_{2/m}}$	$mol \cdot m^{-3}$
C_0	Standard concentration, $1\,M$ or $10^3\,mol \cdot m^{-3}$	$mol \cdot m^{-3}$
C_i	Concentration of species i	$mol \cdot m^{-3}$
$CO_{2,0}$	Total dissolved CO_2 concentration, $CO_{2,0} = C_{CO_2} + mC_{Am(CO_2)_m}$	$mol \cdot m^{-3}$
c_{Cu}	Fraction of copper consumed before regeneration	1
c_p	Constant pressure heat compacity	$J \cdot mol^{-1} \cdot K^{-1}$ or $J \cdot m^{-3} \cdot K^{-1}$
Cu_0	Total copper concentration, $Cu_0 = C_{Cu^{2+}} + C_{Cu^{II}Am^{2+}_{2/m}} \approx C_{Cu^{II}Am^{2+}_{2/m}}$	$mol \cdot m^{-3}$
D_i	Diffusivity of component i	$m^2 \cdot s^{-1}$
$D_{i,eff}$	Effective Diffusivity of component i	$m^2 \cdot s^{-1}$
e	Proton charge (absolute value of electron charge), $1.60218 \times 10^{-19}\,C$	C
e_i	Material i (Copper, plastic, graphite) excess required (flat plate only)	1
E	Potential	V
E°	Standard state potential for a half reaction	V
E^{dev}	Deviation potential (from a state with no CO_2 present)	V
E_{eq}	Equilibrium potential for a half reaction	V
F	Faraday Constant, $96485.3329\,C \cdot mol^{-1}$	$C \cdot mol^{-1}$
f_e	EMAR faradaic efficiency	1
H_{ch}	Channel depth	m
H_m or H_{mem}	Membrane thickness	m
H_{HX}	Thickness of graphite heat exchanger	m
H_{ss}	Thickness of stainless steel end plate	m
H_{Tot}	Total stack height	m
ΔH_{CO_2}	Enthalpy of CO_2 desorption	$J \cdot mol^{-1}$

Variable	Description	SI Units
$H_{f,Cu-Am}$	Heat of formation of Cu-Amine complex, per amine	$J \cdot mol$
I_{max}	Maximum current to EMAR process	1
i	Current density seen in unit cell	$A \cdot m^{-2}$
$\mathbf{i}_l = \begin{bmatrix} i_{l,x} & i_{l,y} \end{bmatrix}^T$	Ionic current density, or liquid current density, vector	$A \cdot m^{-2}$
i_{loc}	Local current density	$A \cdot m^{-2}$
K_0	Prexponentail factor for CO_2/amine binding constant	1
K_{CO_2}	Amine/CO_2 binding constant	1
k_{eff}	Effective themal conductivity	$W \cdot m^{-1} \cdot K^{-1}$
k_l	Liquid thermal conductivity	$W \cdot m^{-1} \cdot K^{-1}$
k_s	Electrode thermal conductivity	$W \cdot m^{-1} \cdot K^{-1}$
$k_{H,i}$	Henry's Law constant for component i	$mol \cdot m^{-3} \cdot Pa^{-1}$
$\tilde{k}_{H,CO_2}$	Dimensionless Henry's Law constant for CO_2, $\tilde{k}_{h,CO_2} = \frac{k_{h,CO_2} P_0}{mAm_0}$	1
$k_{H0,i}$	Standard state Henry's Law constant for component i	$mol \cdot m^{-3} \cdot Pa^{-1}$
$k_{H,elec}$	Electrolyte effect on CO_2 Solubility	1
k_{ij}	Binary interaction parameter for compents i and j	1
L	Channel length	m
M_{CO_2}	Molecular weight of CO_2, $44.01 \times 10^{-3}\, kg \cdot mol^{-1}$	$kg \cdot mol^{-1}$
M_{Cu}	Molecular weight of copper, $62.55 \times 10^{-3}\, kg \cdot mol^{-1}$	$kg \cdot mol^{-1}$
$\dot{m}_{CO_2,e}$	CO_2 emission from flue gas	$kg \cdot s^{-1}$
m_i	Mass of material i (copper, graphite, plastic, etc.) required	kg
m	Number of CO_2 molecules bound by an amine	1
n	Number of electrons participating in an electrochemical reaction	1
$\dot{n}$	Molar flow rate	$mol \cdot s^{-1}$
$\dot{n}_i$	Molar flow rate of species i	$mol \cdot s^{-1}$
$\mathbf{n}$	Inner normal vector	1
$\mathbf{N}_i$	Flux of species i	$mol \cdot m^{-2} \cdot s^{-1}$

Variable	Description	SI Units
n_m	Number of electrons participating in surface reaction m	1
N_{cell}	Total number of unit cells in EMAR system	1
$N_{cell,parallel}$	Total number of unit cells in EMAR system aligned electrically in parallel	1
$N_{cell,series}$	Total number of unit cells in EMAR system aligned electrically in series	1
$N_{cell,stack}$	Total number of unit cells in a stack	1
$N_{cell,stack,max}$	Maximum number of unit cells in a stack	1
N_{stack}	Total number of cell stacks in EMAR system	1
$N_{stack,parallel}$	Total number of cell stacks in EMAR system aligned electrically in parallel	1
$N_{stack,series}$	Total number of cell stacks in EMAR system aligned electrically in series	1
$\dot{n}_{CO_2}$	Molar Flow Rate of CO_2 Captured	$mol \cdot s^{-1}$
$n_{Cu,min}$	Copper moles required at minimum	mol
n_{HX}	Number of cells per heat exchange plate	1
P	Pressure	Pa
P_0	Standard pressure, $10^5\,Pa$ or $1\,Bar$	Pa
P_i	Partial pressure of component i	Pa
$\tilde{P}_{CO_2}$	Dimensionless partial pressure of CO_2, $\tilde{P}_i = \frac{P_i}{P_0}$	1
Q	Heat sink or source term, volumetric flow rate, or state of charge	$W \cdot m^{-3}$ or $m^3 \cdot s^{-1}$ or C
Q_l	Source or sink term in liquid	$A \cdot m^{-3}$
$\mathbf{q}$	Heat Flux	$W \cdot m$
q_0	Inflow heat flux	$W \cdot m^{-2}$
Q_m	Source or sink term in membrane	$A \cdot m^{-3}$
R	Gas Constant, $8.3144598\,J \cdot mol^{-1} \cdot K^{-1}$	$J \cdot mol^{-1} \cdot K^{-1}$
R_i	Reaction rate of species i by volume reaction	$mol \cdot m^{-3} \cdot s^{-1}$
$R_{i,m}$	Reaction rate of species i in electrode reaction m	$mol \cdot m^{-3} \cdot s^{-1}$
$R_{i,tot}$	Total reaction rate of species i	$mol \cdot m^{-3} \cdot s^{-1}$
s_{Cu}	Total copper surface area	m^2
T	Temperature	K
T_0	Standard temperature	K
$\mathbf{u} = \begin{bmatrix} u_x & u_y \end{bmatrix}^T$	Velocity vector	$m \cdot s^{-1}$
$\bar{u}$	Average liquid velocity	$m \cdot s^{-1}$

Variable	Description	SI Units
$u_{mem,i}$	Mobility of component i	$s \cdot mol \cdot kg^{-1}$
$u_{mem,i,eff}$	Effective mobility of component i	$s \cdot mol \cdot kg^{-1}$
ΔV_{cell}	EMAR cell voltage	V
W	Cell width or work	m or J
$\bar{W}$	Molar work, generally per mol CO_2	$J \cdot mol^{-1}$
x_{cap}	Fraction of CO_2 emission captured	1
x_{CO_2}	Carbon dioxide loading, $x_{CO_{2,0}} = \frac{C_{CO_2}+mC_{Am(CO_2)m}}{Am_0} = \frac{CO_{2,0}}{mAm_0}$	1
$x_{CO_{2,0}}$	Effective CO_2 Loading, $x_{CO_{2,0}} = \frac{C_{CO_2}+mC_{Am(CO_2)m}}{Am_0} = \frac{CO_{2,0}}{mAm_0}$	1
x_{Cu}	Copper loading, $x_{Cu} = \frac{2C_{Cu^{II}Am^{2+}_{2/m}}}{mAm_0} \approx \frac{2Cu_0}{mAm_0}$	1
Δx_{Cu}	Copper loading shift	1
x_i	Absorbent loading of component i	1
z	Number of electrons participating in a half cell reaction	1
z_i	Valence (charge) of species i	1
α_{Cu}	Specific surface area of copper foam (porous only)	m^2/m^3
β	Amine-copper or Amine-blocker binding affinity	1
ϵ_l	Electrolyte volume fraction, porous electrode void fraction	1
ϵ_{mem}	Membrane void fraction	1
ε_i	Material i void space (plastic, graphite) required	1
η	Efficiency or overpotential	1 or V
$\nu_{m,i}$	Stoichiometric coefficient for electrode reaction m, negative for ox species, $\sum_{ox} \nu_{ox} S_{ox} + ne^- \Leftrightarrow \sum_{red} \nu_{red} S_{red}$	1
ρ	Density or molar density	$kg \cdot m^{-3}$ or $mol \cdot m^{-3}$
ρ_l	Liquid density	$kg \cdot m^{-3}$
τ_c	Time before switching cycle	s
ϕ_l	Electrolyte potential	V
ϕ_s	Electrode potential	V
$\nabla = \begin{bmatrix} \frac{\partial}{\partial x} & \frac{\partial}{\partial y} \end{bmatrix}^T$	Differential operator	$1/m$

Variable	Description	SI Units
EDA	Ethylenediamine, IUPAC: Ethane-1,2-diamine	
EMAR	Electrochemically Mediated Amine Recovery, pronounced /’ēÂůmÃď’r/	
OCV	Open circuit voltage or open circuit potential	
PFD	Process flow diagram	
SOC	State of Charge	

Chapter 1

Introduction

Executive Summary

Contained herein is a summary of modeling, design, and experimentation on an electrochemical carbon dioxide capture process known as Electrochemically Mediated Amine Recovery or EMAR for short. This thesis builds off of the work of Stern and others and provides a more detailed understanding of the thermodynamics and mass and heat transport phenomena encountered in an EMAR separation process.[1,2] In addition it provides a description and reports the performance of three new generations of EMAR cells and separation apparatuses.

EMAR provides unique advantages over traditional industrial carbon dioxide capture processes. These include increased efficiency due to the targeted nature of electrochemical process and a process flow scheme which may be more easily implemented in a retrofit application. This introductory chapter details the general motivation behind carbon dioxide capture processes and current industrial CO_2 capture techniques. This chapter motivates the modeling, design, and experimental work with the EMAR process described below.

Chapter 2 explores the thermodynamics of four electrochemical architectures, each primarily liquid state, which may be employed in carbon dioxide capture. Two are Electrochemically-Mediated Complexation Separation (EMCS) processes while the remaining two are Electrochemically-Mediated Competitive Complexation Separation (EMCCS) processes. In particular a relationship is established between the state of a liquid stream and that stream's open circuit potential. Thermodynamic paths are established between states, which in concert with the open circuit potential determine the electrochemical work required for a variety of molecular architectures and system geometries. Two categories of molecular architectures, activated absorbent and blocking systems, are described this chapter, followed by three possible system geometries.

Chapter 3 applies the framework established by Chapter 2 to the EMAR process, which is, in the structure established by the previous chapter, a three-stage EMCCS architecture with a solid inactive blocker. It reveals a previously unknown thermodynamic cycle for the the EMAR process, which it uses to establish a minimum thermodynamic work for separation based on key operating conditions. It further suggests ideal process flow schemes for the EMAR process and analyzes, and ultimately rejects, previously considered EMAR geometries.

Chapter 4 builds on the EMAR thermodynamics established in Chapter 3, by detailing a mass and heat transport model. This chapter introduces two possible EMAR stack geometries, parallel and series, and explores the heat conservation within each geometry. Temperature profiles reveal that the parallel geometry results in more severe temperature gradients than that of the series geometry. This chapter further explores overpotential losses and finds that the dominant overpotential in a current EMAR stack is the activation overpotential, which suggests the need for a larger surface area electrode.

While the first four chapters establish a theoretical basis and optimal conditions for the EMAR process, Chapter 5 details EMAR cell design and performance. A brief historical perspective is provided on single unit cell EMAR systems designed by Stern and Eltayeb.[1,2] This is followed by a detailed discussion of multiple unit cell - i.e. stacked - EMAR desorber systems which may be assembled in parallel or series configuration. Experimental results demonstrate the efficacy of these stacked systems and serve to validate the model presented in Chapter 4.

The final chapter frames this work in an economics context in order to establish (1) the costs associated with carbon dioxide removal via the EMAR process and (2) potential markets for the EMAR process. It concludes that most promising market for EMAR technology is that of carbon dioxide separation as a service, specifically in natural gas sweetening. A five forces analysis is completed in order to make strategic suggestions for operation in such a market.

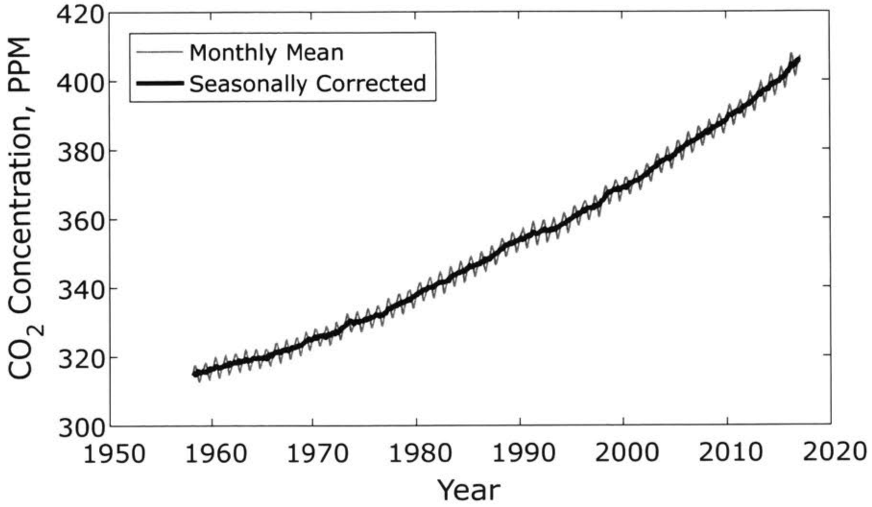

Figure 1-1: CO_2 concentration data from Mouna Loa observatory showing a 25% increase in atmospheric CO_2 since 1960.[3]

Motivation

Climate Change and Regulation

Anthropogenic carbon dioxide emissions have resulted in a 40% increase in atmospheric CO_2 concentration since the industrial revolution, half of which has come in the last 50 years, as demonstrated in Figure 1-1.[4] Carbon dioxide, a greenhouse gas, absorbs infrared ration reflected from the earth's surface which would otherwise be sent to space.[5] As such, there is strong agreement within the scientific community that these greenhouse gas emissions are causing climate change.[6] The result, seen in Figure 1-2, is a sharp increase in global temperature anomalies over the same time 50 year period. An average global temperature increase of 0.8 °C since 1900 is one of many symptoms of this change which also include rising and more acidic oceans, significant loss of arctic sea ice, and a myriad of related climate events. Mitigation of climate change, whose primary cause is anthropogenic CO_2 production, is therefore one of the most important issues the scientific community currently faces.[7]

In 2014 the United States alone emitted more than 5 billion metric tonnes of CO_2. The source of these emissions is primarily the combustion of hydrocarbons from fossil fuel, though other CO_2 sources exist including aluminum and cement production.[9] Figure 1-3 details CO_2 emissions by industry, of which electricity generation and transportation dominate. A significant reduction in these emissions must occur to mediate the climate effects described above.[10,11] It is expected, however, that fossil fuel combustion will increase moderately over the next 30 years before renewables begin to supplant incumbent technologies.[12,13]

Carbon Dioxide Markets and Storage

A significant need thus exists for carbon dioxide capture and usage or storage. In fact, the International Energy Agency suggests that some 100 GW of power plant capacity, representing 0.5 billion metric tonnes of CO_2 production per year, must employ carbon capture and storage (CCS) to ameliorate greenhouse gas emissions .[15] Captured CO_2 may be sold into a variety of markets, as show in Figure 1-4. The dominant space is enhanced oil recovery, where CO_2 dissolves and displaces oil which would otherwise go untapped from an oil well.[16] Oil recovered in such a manner has a lower carbon footprint as most CO_2 injected for enhanced oil recovery remains permanently trapped in the former oil well. Other markets for CO_2 sales include food and beverage.

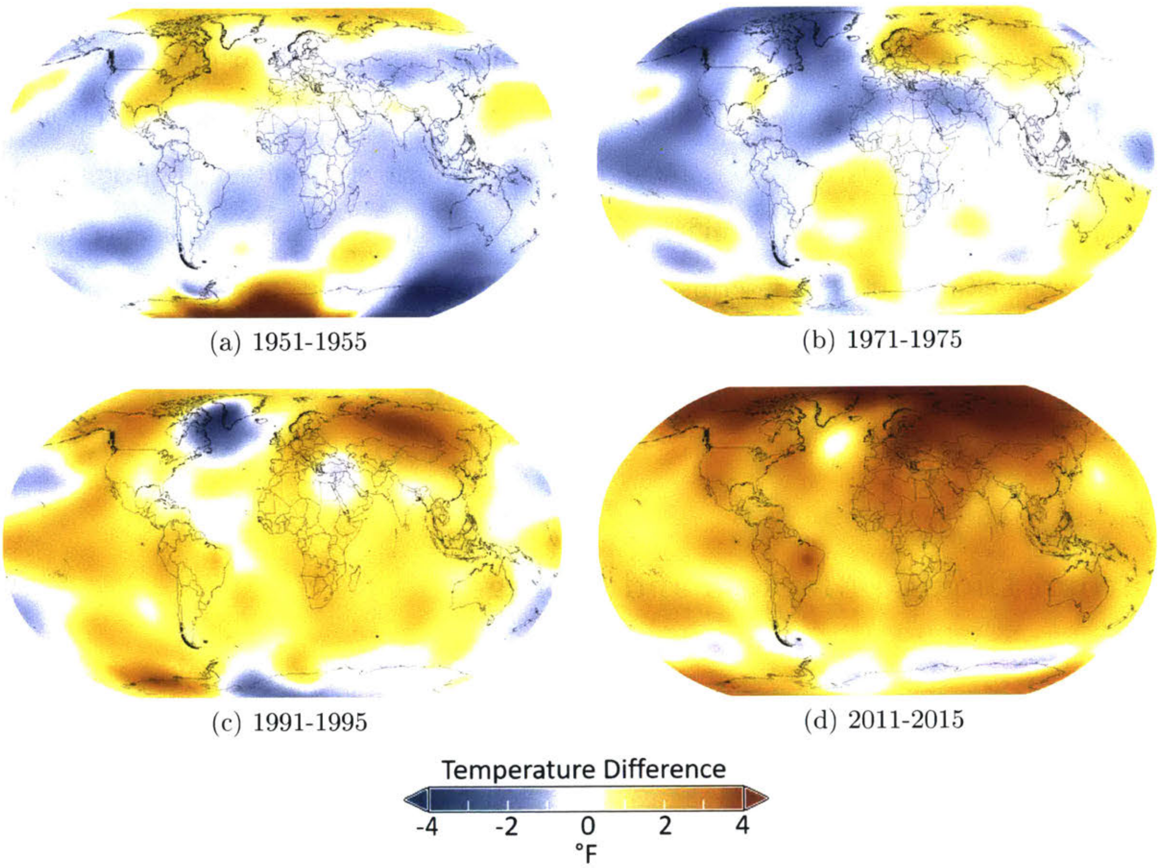

(a) 1951-1955

(b) 1971-1975

(c) 1991-1995

(d) 2011-2015

Figure 1-2: Five year global temperature difference anomalies from a baseline of 1951-1980 for periods starting in 1951, 1971, 1991, and 2011 show a clear trend towards a more severe, hotter climate.[8]

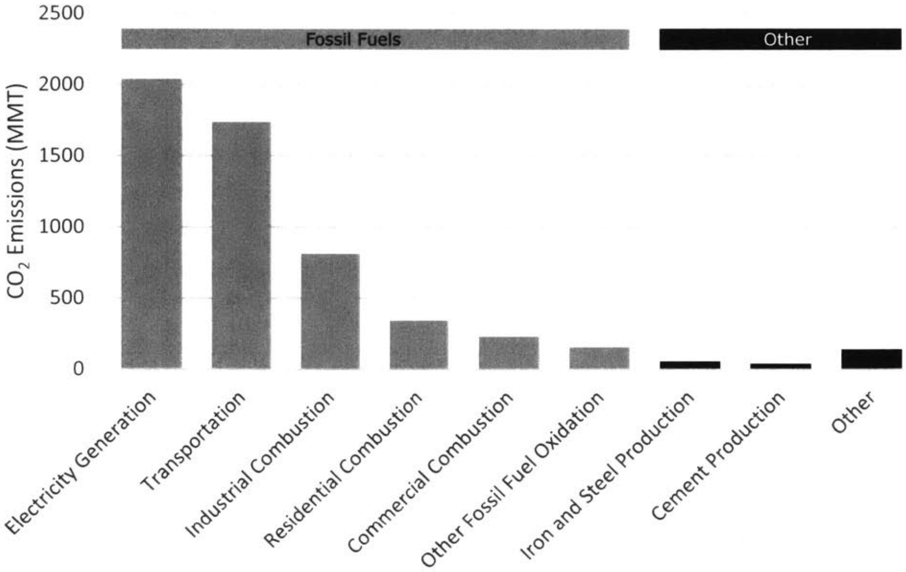

Figure 1-3: CO_2 emissions by US industry in 2014 in megatonnes (Mt)[9]

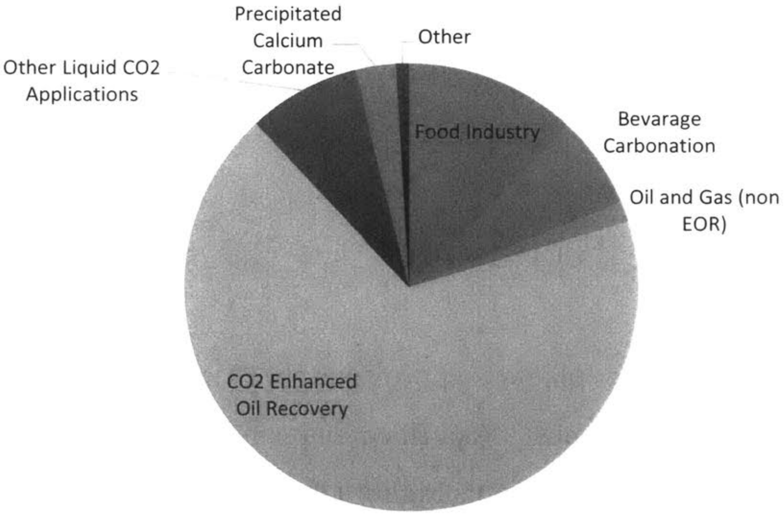

Figure 1-4: Share of 80 megatonnes (Mt) per year market as of 2011 by sector. Market is expected to grow to 140 Mt/year by 2020.[14]

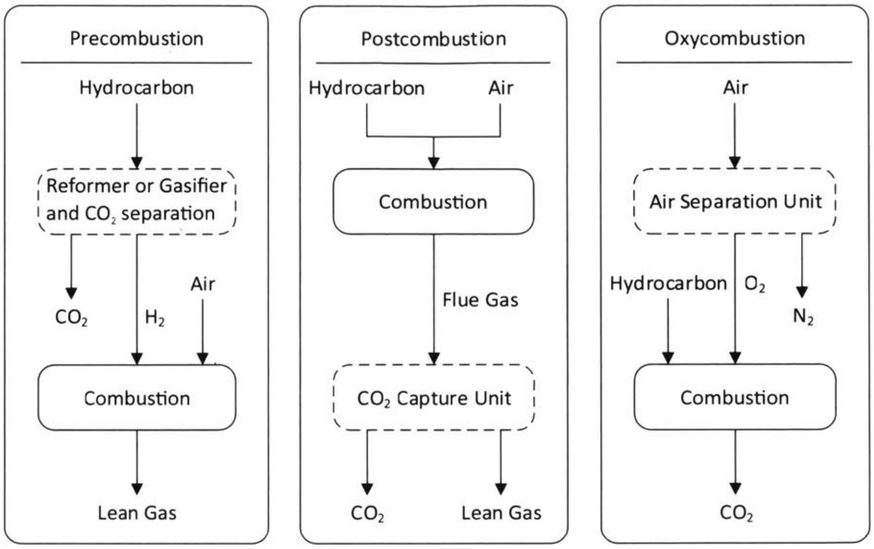

Figure 1-5: Standard options for CO_2 capture from hydrocarbon fuel sources[18]

Still demand for CO_2, 80 - 140 Mt/yr,[14] is a small fraction of emissions to be captured so storage will be required in many cases. Proposed storage technologies include deep saline aquifers and geological storage.[17]

Carbon Capture Techniques

Flue gas from coal fired power plants is approximately 15 mol% CO_2.[18] For most CCS systems, that carbon dioxide must be purified and compressed to pipeline pressures of approximately 150 bar. As shown in Figure 1-5, three strategies exist for capture of CO_2 produced from hydrocarbon combustion: precombustion, postcombustion, and oxycombustion.

Precombustion requires pre-processing of a hydrocarbon stream by gasification or reforming. Though little power may be generated from this step, the hydrocarbon stream is converted to a primarily hydrogen and carbon dioxide stream. The high concentration CO_2 may separated from this stream leaving only hydrogen, whose combustion produces only water.

Oxycombustion on the other hand, removes oxygen from air as a pre-treatment step, so that pure O_2 may be used for oxidation. The resulting product of combustion contains primarily carbon dioxide and water, which may be easily separated.

The most straight forward method is post-combustion. This method deploys a CO_2 capture unit on the flue gas leaving a power plant or industrial process. Of the three methods, it is the only method which has been retrofitted onto an existing power plant, though oxy-fuel combustion retrofits have been proposed.[19] Of the three methods, Post-combustion CCS is considered the standard.[2]

Treatment of the 15% CO_2 flue gas stream may be accomplished through thermal driven,[20] pressure driven,[21] or electrochemical driven[22] methods. Pressure driven methods, which are difficult to employ for atmospheric pressure emissions, include pressure swing adsorption, such as metal organic frame works (MOFS),[23] or membrane separations.[24] The latter cannot efficiently achieve purities sufficient for pipeline conditions and therefore require multiple stages, while the former requires huge sorbent beds due to very low volumetric storage capacities.[25]

The incumbent technology for post-combustion CCS is thermal amine scrubbing, which has been in use industrially since 1930 and is shown in Figure 1-6.[26] The thermal amine process couples a low temperature absorption with a high temperature desorption. In the absorber, amines at approximately 60 °C are exposed to the flue gas stream. The basic amines undergo an exothermic acid/base reaction with the

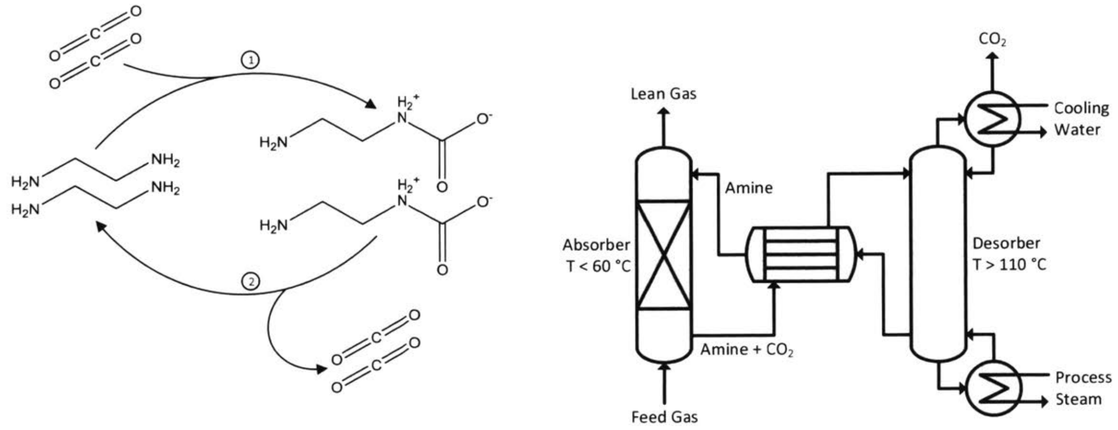

(a) Thermal Amine Chemistry (b) Thermal Amine Process Flow Diagram

Figure 1-6: Thermal amine scrubbing utilizes an amine sorbent to capture CO_2 (reaction 1) from a feed stream. CO_2 is desorbed by heating the amine/CO_2 complex (reaction 2).

moderately acidic CO_2, stripping this and other acid gases from the stream, and forming a CO_2/amine complex. At higher temperatures - roughly 110 °C - entropic effects dominate and the reaction reverses in an endothermic manner, releasing CO_2 and refreshing the amines for additional capture.[26]

EMAR System

Electrochemically Mediated Amine Recovery (EMAR), described in detail throughout this thesis, is a post-combustion process. The EMAR process, which modifies thermal amine scrubbing as shown by Figure 1-7, was first introduced by Stern et al.[27] As in the thermal amine process, in the EMAR process amine absorbents are used at low temperature to extract CO_2 from a feed gas stream. The CO_2 bound sorbent is then fed to the anodic channel of an electochemical cell. Here, copper metal

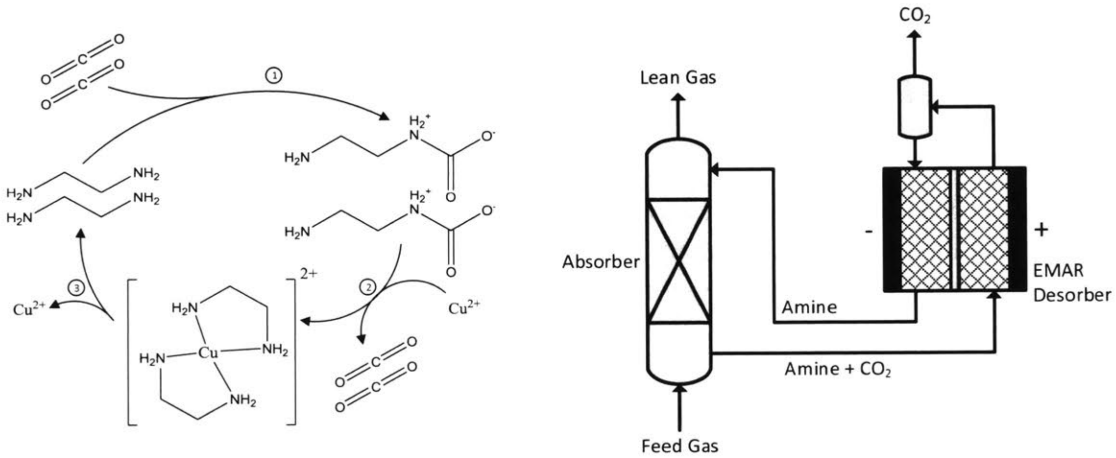

(a) EMAR Chemistry

(b) EMAR Process Flow Diagram

Figure 1-7: Electrochemical Mediated Amine Recover (EMAR) modifies thermal amine scrubbing by replacing the thermal desorption (reaction 2 from Figure 1-6) with an electrochemical desorption. The anodic reaction (reaction 2) oxidizes copper and introduces cupric species to CO_2 bound amine sorbents, which bind the copper and release CO_2. The cathodic reaction (reaction 3) reduces the copper/amine complex, regenearting the amine for capture.

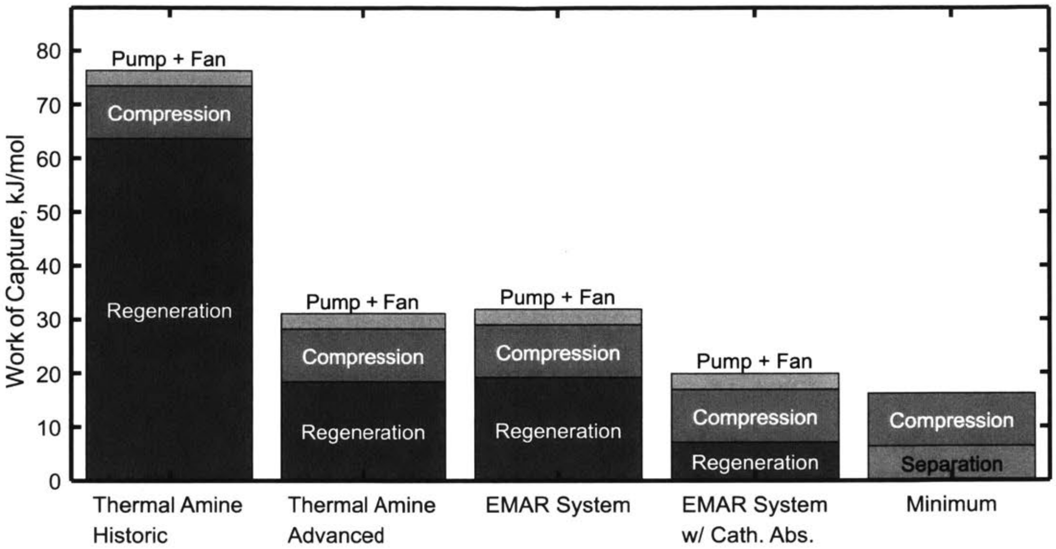

Figure 1-8: Thermodynamic comparison between EMAR process, state of the art thermal amine processes, and traditional thermal amine process for 90% capture of a 15% CO_2 stream and compression to 150 bar.

is oxidized and the resulting cupric ions complex the previously CO_2 bound amines, causing CO_2 release and desorption. After separating the gas and liquid streams, the liquid stream is brought to the cathodic chamber of the electochemical cell where the copper-amine complex is reduced, plating out the copper and refreshing the amines for addition capture in the absorber.

EMAR provides a few key advantages over thermal amine scrubbing. The first is thermodynamic. Figure 1-8 compares the EMAR process to historic thermal amine scrubbing processes, such as the Lubbock plant, which used MEA, and state of the art thermal amine processes proposed by Rochel.[28] Thermodynamically, the EMAR process is twice as efficient at traditional thermal amine processes and of comparable efficiency to state of the art thermal processes which employ complex process flow schemes such as the advanced flash stripper demonstrated by Lin et al.[29] However, as will be seen in Chapter 3, a shift in EMAR architecture from a standard absorber to a cathodic absorber will serve to bring the EMAR thermodynamic efficiency to near that of the thermodynamic minimum. This efficiency boost stems from the targeted nature of electrochemical processes.

EMAR has advantages from a capital standpoint as well. EMAR more easily integrates with existing infrastructure for brownfield installations. Since EMAR is an entirely electrically driven process, it does not require the installation of a reboiler as does the thermal amine process. Further, as will be discussed later, the EMAR process allows for high pressure desorption of CO_2 for compression. The high temperature required for high pressure desorption in the thermal case, generally causes amine degradation, though some amines such as piperazine are resistant to this degradation.[30] High pressure CO_2 release decreases the compression ratio seen in the compressor, thereby decreasing the compressor size and capital cost. Of course, the work of compression is also decreased at the cost of more energy intensive amine regeneration.

THIS PAGE INTENTIONALLY LEFT BLANK

Chapter 2

Thermodynamics of Electrochemical CO_2 Capture Systems

Carbon dioxide, an electrophile, may be bound by a nucleophilic species. Therefore an electrochemical system, which manipulates the nucleophicity of a redox active absorbent or system may be used to selectively capture CO_2. Reduction increases an absorbent's nucleophicity, therefore such a species or system would be activated for absorption at the cathode and deactivated at the anode.[31–33] The first such electrochemical carbon dioxide capture system was proposed in 1988 by DuBois et al.[33]

This chapter explores the thermodynamics of four electrochemical architectures, each primarily liquid state, which may be employed in carbon dioxide capture. In particular a relationship is established between the state of a liquid stream and that stream's open circuit potential. Thermodynamic paths are established between states, which in concert with the open circuit potential determine the electrochemical work required for a variety of molecular architectures and system geometries. Two categories of molecular architectures, activated absorbent and blocking systems, are described below, followed by three possible system geometries.

Modeling Electrochemical Systems

An electrochemical system's thermodynamics are governed by the Nernst Equation given in equation 2.1. Consider the half cell reaction given below, where the oxidative species, Ox, is being reduced to form the reductive species, Red. The Nerst equation defines the equilibrium potential for such a reaction.

$$Ox + ze^- \rightleftharpoons Red$$

$$E_{eq} = E^\circ - \frac{RT}{zF} \ln \left(\frac{a_{Red}}{a_{Ox}} \right) \tag{2.1}$$

If the voltage difference between the electrode (the electron source or sink) and the solution is greater than this equilbrium potenial the anodic reaction - i.e. the formation of the oxidative species, Ox - is favored. If this voltage difference is less, the cathodic reaction - i.e. the formation of the reductive species, Red - is favored.

The Nerst equation will be the basis by which the open circuit potential for the molecular architectures discussed below will be established.

Activated Absorbent vs Blocker

Stern describes two architectures for electrochemcially mediated carbon dioxide capture: Electrochemically-Mediated Complexation Separation (EMCS) and Electrochemically-Mediated Competitive Complexation Separation (EMCCS).[1] In EMCS a redox active absorbent is activated for capture at the cathode and deactivated at the anode. In EMCCS a redox active blocker species whose electrophilicity may be manipulated serves to bind an electrochemically inert absorbent. Since this blocker species becomes a stronger electrophile upon oxidation, the absorbent is bound and deactivated at the anode.

The thermodynamics of each of these systems is described below. Further, the thermodynamics of four possible process geometries are described. The first is a two-stage system, where carrier activation and CO_2 absorption occur simultaneously at the cathode and carrier deactivation and CO_2 desorption occur at the anode. The second is a four-stage system where activation and deactivation, which occur at the cathode and anode respectively, are decoupled from absorption and desorption. Two possible three-stage systems are created by incorporating either a cathodic absorption or anodic desorption in an otherwise four-stage system.

EMCS - Activated Absorbent

The simplest EMCS cycle involves a concerted m electron electrochemical reaction and a homogeneous binding of an activated absorbent, A^{m-}, to m CO_2 molecules. Therefore, for every one electron passed through the EMCS cycle one CO_2 is captured at perfect faradaic efficiency. Examples of this include may include: Scovazzo et al.'s

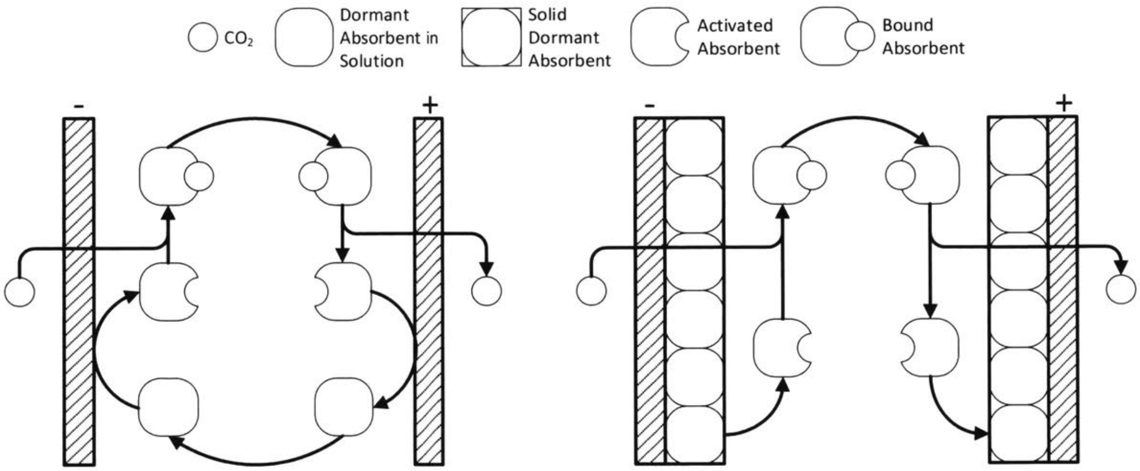

(a) Dormant Absorbent in Solution Architecture

(b) Solid Dormant Absorbent Architecture

Figure 2-1: Two possible EMCS architectures exist: (a) the dormant absorbent remains in solution with the active absorbent, (b) only the active absorbent is in solution.

one electron bipyridine cycle[34] and Gurkan et al.'s two electron quinone process.[22] The open circuit potential for this reaction establishes total work of separation for an EMCS cycle. It will be shown that the strength of binding, defined by binding constant K_{CO_2}, has a strong effect on this open circuit potential.

The EMCS architecture requires that an activated carrier molecule be in solution in order to transport bound carbon dioxide to the anode for release. However, an inactive absorbent may be either in solution or in a solid state. The state of this inactive absorbent will affect the open circuit potential described below. As shown in Figure 2-1, a dormant absorber in solution may be used in a continuous cycle, whereas a solid dormant absorbent will be shuttled from cathode to anode.

Inactive Absorbent in Solution

Consider first an EMCS cycle with an inactive absorbent in solution, like that employed by Scovazzo.[34] The open circuit potential for such as system, as described by the Nernst Equation, is given in equation 2.2a.

$$\begin{array}{lll}
\text{Electrochemical} & \mathrm{A(aq) + me^- \rightleftharpoons A^{m-}(aq)} & (a) \\
 & E = E^\circ - \frac{RT}{mF}\ln\left(\frac{C_{A^{m-}}}{C_A}\right) & \\
\text{Homogeneous} & \mathrm{A^{m-}(aq) + mCO_2(g) \rightleftharpoons A(CO_2)_m{}^{m-}(aq)} & (b) \\
 & K_{CO_2} = \frac{C_{A(CO_2)_m^{m-}}}{C_{A^{m-}}}\left(\frac{P_0}{P_{CO_2}}\right)^m & \\
\hline
\text{Overall} & \mathrm{A(aq) + me^- + mCO_2(g) \rightleftharpoons A(CO_2)_m{}^{m-}(aq)} & (c)
\end{array} \tag{2.2}$$

The state of a stream in such a system is given by the following inputs:

- Total concentration of absorbent - activated, inactivated, or bound
- Fraction absorbents activated or bound (state of charge)
- CO_2 partial pressure
- Stream temperature

The first two conditions are given by equations 2.3 and 2.4 respectively, while the later two conditions will be externally imposed.

$$A_0 = C_A + C_{A^{m-}} + C_{A(CO_2)_m^{m-}} \tag{2.3}$$

$$x_{A'} = \frac{C_{A^{m-}} + C_{A(CO_2)_m^{m-}}}{A_0} \tag{2.4}$$

Notice, the state of charge (SOC) is directly related to the total absorbent concentration and the activated fraction as given in equation 2.5.

$$SOC = m\left(C_{A^{m-}} + C_{A(CO_2)_m^{m-}}\right) = mA_0x_{A'} \tag{2.5}$$

The state of charge as well as the open circuit potential, given by equation 2.2a, define the total work of capture for an EMCS cycle. An approach similar to that taken by Gurkan is presented in Appendix B to arrive at a relationship between the open circuit potential and the parameters which define the state of the system. The result is given in equation 2.6. It is of note that the open circuit potential is not a function of total absorbent concentration for the activated absorbent architecture, this will not be the case for other architectures described.

$$E = E^{\circ} + \frac{RT}{mF}\left[\ln\left(\frac{1-x_{A'}}{x_{A'}}\right) + \ln\left(1 + K_{CO_2}\tilde{P}_{CO_2}^{m}\right)\right] \tag{2.6}$$

where $\tilde{P}_{CO_2} = P_{CO_2}/P_0$.

If we define E_0 as the open circuit potential of a stream with no CO_2 ($P_{CO_2} = 0$), then E_0 is only a function of state of charge. Further, define E^{dev} as the open circuit potential deviation from E_0. As shown in equation 2.7, E^{dev} is a function of only CO_2 partial pressure, not state of charge or total absorbent concentration.

$$E^{dev} = E\left(P_{CO_2}, x_{A'}\right) - E_0\left(x_{A'}\right) = \frac{RT}{mF}\ln\left(1 + K_{CO_2}\tilde{P}^{m}_{CO_2}\right) \tag{2.7}$$

Solid Inactive Absorbent

Now, consider an EMCS system with a solid state inactive absorbent. By assuming a unity activity for the solid species, we modify the Nernst Equation given in equation 2.2a resulting in equation 2.8a.

$$\begin{array}{lll}
\text{Electrochemical} & \mathrm{A(s) + me^- \rightleftharpoons A^{m-}(aq)} & (a) \\
 & E = E^\circ - \frac{RT}{mF}\ln\left(\frac{C_{A^{m-}}}{C_0}\right) & \\
\text{Homogeneous} & \mathrm{A^{m-}(aq) + mCO_2(g) \rightleftharpoons A(CO_2)_m{}^{m-}(aq)} & (b) \\
 & K_{CO_2} = \frac{C_{A(CO_2)_m^{m-}}}{C_{A^{m-}}}\left(\frac{P_0}{P_{CO_2}}\right)^m & \\
\hline
\text{Overall} & \mathrm{A(s) + me^- + mCO_2(g) \rightleftharpoons A(CO_2)_m{}^{m-}(aq)} & (c)
\end{array} \tag{2.8}$$

As before the state of a stream in such a system is given by the following inputs:

- Total concentration of absorbent - activated or bound (state of charge)
- CO_2 partial pressure
- Stream temperature

The total absorbent concentration is given by equation 2.9.

$$A_0 = C_{A^{m-}} + C_{A(CO_2)_m^{m-}} \tag{2.9}$$

Since inactive absorbent is solid in this scenario, the state of charge of is a function of the amount of absorbent which has become activated and entered solution as given by equation 2.10.

$$SOC = m\left(C_{A^{m-}} + C_{A(CO_2)_m^{m-}}\right) = mA_0 \tag{2.10}$$

Appendix B establishes the relationship between the open circuit potential of a stream and its state as given in equation 2.11. Notice that though the open circuit potential relationship varies for the dormant absorbent in solution versus the solid dormant absorbent systems - as given by equations 2.6 and 2.11 respectively - their deviation potentials, given by equations 2.7 and 2.12, are the same. This will be seen for EMCCS systems as well.

$$E = E^{\circ} + \frac{RT}{mF}\left[\ln\left(1 + K_{CO_2}\tilde{P}_{CO_2}^{m}\right) - \ln\left(\frac{A_0}{C_0}\right)\right] \tag{2.11}$$

$$E^{dev} = E\left(P_{CO_2}, A_0\right) - E_0\left(A_0\right) = \frac{RT}{mF}\ln\left(1 + K_{CO_2}\tilde{P}_{CO_2}^{m}\right) \tag{2.12}$$

EMCCS - Redox Blocker

An EMCCS cycle differs from an EMCS cycle in the redox active material. For an EMCCS cycle the redox active material is activated to block a non-redox active absorbent. The simplest EMCCS cycle involves a concerted n electron electrochemical reaction which oxidizes a blocker molecule, B, enabling the blocking of absorbent

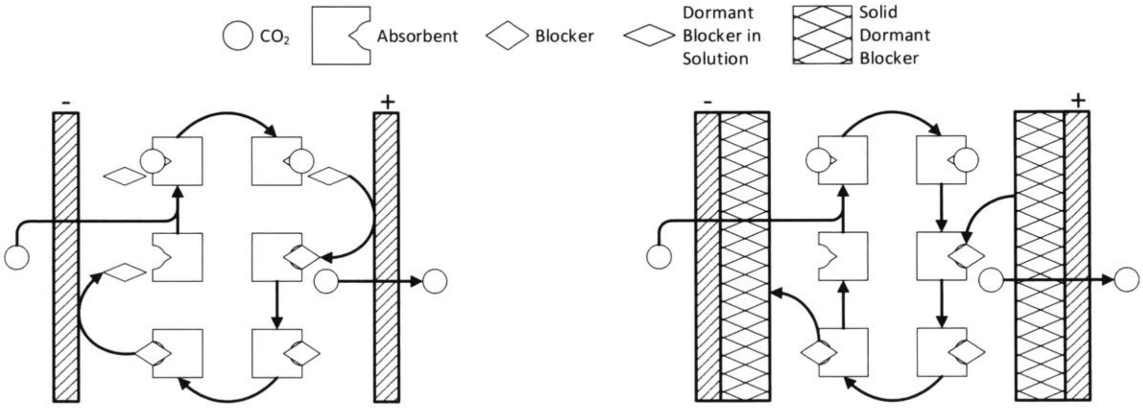

(a) Dormant Blocker in Solution Architecture

(b) Solid Dormant Blocker Architecture

Figure 2-2: Two possible EMCCS architectures exist: (a) the dormant blocker remains in solution with the absorbent and active blocker, (b) only the active blocker and absorbent are in solution.

A. A homogeneous reaction of free absorbent to bind m CO$_2$ molecules may occur in the absence of a blocker. As in the EMCS cycle one electron releases one CO$_2$ molecule.

Similar to the EMCS system, EMCCS may utilize a dormant redox active species which is either in solution or in the solid state. As shown in Figure 2-2, a dormant blocker in solution may be used in a continuous cycle, whereas a solid dormant blocker will be shuttled from anode to cathode.

Inactive Blocker in Solution

A similar approach to that taken for the thermodynamics of an EMCS system may be employed for an EMCCS system. Consider first an inactive blocker which remains in solution. The open circuit potential for such as system, as described by the Nernst

Equation, is given in equation 2.13a.

$$\begin{array}{llr}
\text{Electrochemical} & \mathrm{B^{n+}(aq) + ne^- \rightleftharpoons B(aq)} & \text{(a)} \\
 & E = E^\circ - \frac{RT}{nF}\ln\left(\frac{C_B}{C_{B^{n+}}}\right) & \\
\text{Homogeneous} & \mathrm{A(aq) + mCO_2(g) \rightleftharpoons A(CO_2)_m}(aq) & \text{(b)} \\
 & K_{CO_2} = \frac{C_{A(CO_2)_m}}{C_A}\left(\frac{P_0}{P_{CO_2}}\right)^m & \\
\text{Homogeneous} & \mathrm{\frac{n}{m}A(aq) + B^{n+}(aq) \rightleftharpoons B(A)^{n+}_{n/m}(aq)} & \text{(c)} \\
 & \beta = \frac{C_{B(A)^{n+}_{n/m}} C_0^{n/m}}{C_A^{n/m} C_{B^{n+}}} & \\
\hline
\text{Overall} & \mathrm{B(A)^{n+}_{n/m}(aq) + ne^- + nCO_2(g) \rightleftharpoons B(aq) + \frac{n}{m}A(CO_2)_m(aq)} & \text{(d)} \\
 & & (2.13)
\end{array}$$

The state of a stream in such a system is given by the following inputs:

- Total concentration of absorbent - unbound or bound by CO_2 or an active blocker
- Total concentration of blocker - active or dormant
- Fraction absorbents bound to blocker (state of charge)
- CO_2 partial pressure
- Stream temperature

The first three conditions are given by equations 2.14, 2.15, and 2.16 respectively, while the later two conditions will be externally imposed.

$$A_0 = C_A + C_{A(CO_2)_m} + \frac{n}{m} C_{B(A)_{n/m}} \tag{2.14}$$

$$B_0 = C_B + C_{B^{n+}} + C_{B(A)_{n/m}^{n+}} \approx C_B + C_{B(A)_{n/m}^{n+}} \tag{2.15}$$

$$x_B = \frac{nC_{B(A)_{n/m}^{n+}}}{mA_0} \tag{2.16}$$

This analysis assumes the binding of the blocker to the absorbent is quite strong, i.e. $\beta \gg 1$ in equation 2.13c. The result is that any activated blocker will be bound to an absorber so long as any absorber remains. Notice then that the state of charge (SOC) is directly related to the total activated blocker fraction as given in equation 2.17.

$$SOC = n\left(C_{B^{n+}} + C_{B(A)_{n/m}^{n+}}\right) \approx nC_{B(A)_{n/m}^{n+}} = mx_BA_0 \tag{2.17}$$

Appendix B establishes the relationship between the open circuit potential of a stream and its state as given in equation 2.18.

$$E = E^{\circ} - \frac{RT}{nF}\left[\ln\left(\frac{nB_0}{mx_BA_0} - 1\right) + \ln\left(\beta\left[\left(\frac{A_0}{C_0}\right)\frac{1-x_B}{1+K_{CO_2}\tilde{P}_{CO_2}^m}\right]^{n/m}\right)\right] \tag{2.18}$$

As before, the deviation potential remains the same - solely a function of CO_2 partial pressure.

$$E^{dev} = E\left(P_{CO_2}, A_0, B_0, x_B\right) - E_0\left(A_0, B_0, x_B\right) = \frac{RT}{mF}\ln\left(1 + K_{CO_2}\tilde{P}_{CO_2}^m\right) \tag{2.19}$$

Solid Inactive Blocker

The EMAR system originally described by Stern, and discussed in detail below, which employs cupric ions as the redox active blocker for amine absorbents, utilizes a solid inactive blocker as seen in Figure 2-2(a).[27]

$$
\begin{array}{lll}
\text{Electrochemical} & \mathrm{B^{n+}(aq) + ne^- \rightleftharpoons B(s)} & \text{(a)} \\
 & E = E^\circ - \frac{RT}{nF} \ln\left(\frac{C_0}{C_{B^{n+}}}\right) & \\
\text{Homogeneous} & \mathrm{A(aq) + mCO_2(g) \rightleftharpoons A(CO_2)_m(aq)} & \text{(b)} \\
 & K_{CO_2} = \frac{C_{A(CO_2)_m}}{C_A} \left(\frac{P_0}{P_{CO_2}}\right)^m & \\
\text{Homogeneous} & \mathrm{\tfrac{n}{m}A(aq) + B^{n+}(aq) \rightleftharpoons B(A)_{n/m}{}^{n+}(aq)} & \text{(c)} \\
 & \beta = \frac{C_{B(A)^{n+}_{n/m}} C_0^{n/m}}{C_A^{n/m} C_{B^{n+}}} & \\
\hline
\text{Overall} & \mathrm{B(A)_{n/m}{}^{n+}(aq) + ne^- + nCO_2(g) \rightleftharpoons B(s) + \tfrac{n}{m}A(CO_2)_m(aq)} & \text{(d)}
\end{array}
\tag{2.20}
$$

The Nernst equation given in 2.20a for this electrochemical reaction assumes that the reduced form of the blocking molecule, *B*, is solid and has an activity of 1. As in the previous case, the assumption is made that $\beta \gg 1$ and the state of a stream in such a system is given by the following inputs:

- Total concentration of absorbent - unbound or bound by CO_2 or an active blocker
- Total concentration of active blocker in solution (state of charge)
- CO_2 partial pressure
- Stream temperature

The first two of these conditions are described by A_0 and B_0 below.

$$A_0 = C_A + C_{A(CO_2)_m} + \frac{n}{m} C_{B(A)_{n/m}^{n+}} \tag{2.21}$$

$$B_0 = C_{B^{n+}} + C_{B(A)_{n/m}^{n+}} \approx C_{B(A)_{n/m}^{n+}} \tag{2.22}$$

For convenience, define the blocker loading as given by equation 2.23.

$$x_B = \frac{nC_{B(A)_{n/m}^{n+}}}{mA_0} \approx \frac{nB_0}{mA_0} \tag{2.23}$$

Notice the state of charge (SOC) is directly related to the total activated blocker in solution as given in equation 2.24.

$$SOC = nB_0 = mx_BA_0 \tag{2.24}$$

Appendix B establishes the relationship between the open circuit potential of a stream and its state as given in equation 2.25.

$$E = E^\circ + \frac{RT}{nF}\left[\ln(x_B) + \ln\left(\frac{mA_0}{nC_0}\right) - \ln\left(1 + \beta\left[\left(\frac{A_0}{C_0}\right)\frac{1 - x_B}{1 + K_{CO_2}\tilde{P}^m_{CO_2}}\right]^{n/m}\right)\right] \tag{2.25}$$

As before, the deviation potential remains the same - solely a function of CO_2 partial

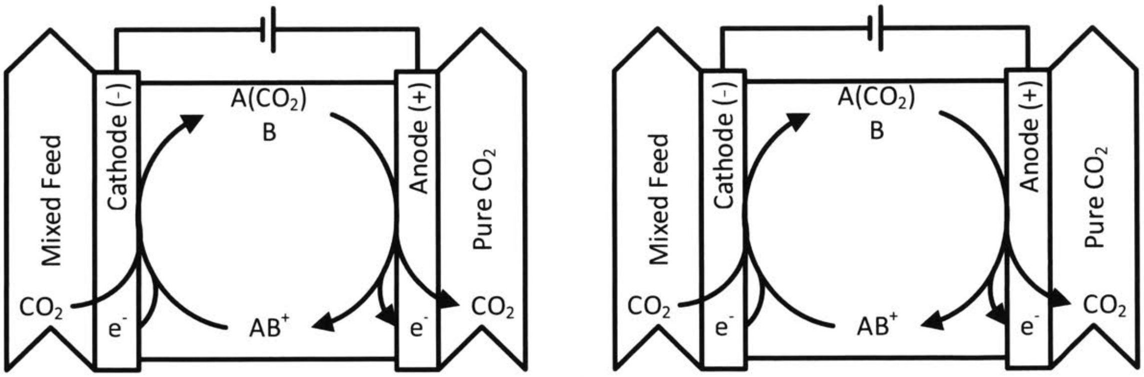

(a) EMCS System (b) EMCCS System

Figure 2-3: Simple Non-flow EMCS (a) and EMCCS (b) cycles.

pressure.

$$E^{dev} = E\left(P_{CO_2}, A_0, x_B\right) - E_0\left(A_0, x_B\right) = \frac{RT}{mF}\ln\left(1 + K_{CO_2}\tilde{P}^m_{CO_2}\right) \tag{2.26}$$

Thermodynamic Minimum Voltage Required for Separation

Notice that E^{dev}- given by equations 2.7, 2.12, 2.19, and 2.26 - is the same for all four systems. Therefore for any of the four architectures, if one considers the simple non-flow system given in Figure 2-3, where fluid in the cathodic absorber and anodic desorber are at the same state of charge, the cathodic and anodic half cell potentials will be given by equation 2.6. The difference between the anodic half cell potential and the cathodic half cell potential is the thermodynamic minimum voltage required for separation, which is given in equation 2.28. See Appendix B for derivation of equation 2.28 from equation 2.6. As expected, higher desorption pressures, $P_{CO_2,anode}$, or lower inlet CO_2 partial pressures, $P_{CO_2,cathode}$, result in higher cell voltage required for capture.

$$E^{dev} = \frac{RT}{mF} \ln\left(1 + K_{CO_2}\tilde{P}^{m}_{CO_2}\right) \tag{2.27}$$

$$\Delta E = E_{anode} - E_{cathode} = E^{dev}_{anode} - E^{dev}_{cathode} = \frac{RT}{mF} \ln\left(\frac{1 + K_{CO_2}\tilde{P}^{m}_{CO_2,anode}}{1 + K_{CO_2}\tilde{P}^{m}_{CO_2,cathode}}\right) \tag{2.28}$$

The minimum work per mole CO_2 captured is a function of the faradaic efficiency, η, and the cell potential, ΔE, and is given by equation 2.30. Some faradaic losses are implicit to electrochemical CO_2 capture systems. These include sub-unity usage of absorbent, particularly at the cathodic absorber, and CO_2 solubility differences at the absorber and desorber, which arise from different partial pressures in this region. These inefficiencies are considered in detail for the EMAR system discussed below, however equation 2.29 gives the most prevalent faradaic loss, namely absorbent usage at the cathodic absorber. The result is equation 2.30, the total work for a system like that given in Figure 2-3.

$$\eta_{cathode} = \frac{K_{CO_2}\tilde{P}^{m}_{CO_2,cathode}}{1 + K_{CO_2}\tilde{P}^{m}_{CO_2,cathode}} \tag{2.29}$$

$$\bar{W} = \frac{F\Delta E}{\eta} \approx \frac{RT}{m}\left(\frac{1 + K_{CO_2}\tilde{P}^m_{CO_2,cathode}}{K_{CO_2}\tilde{P}^m_{CO_2,cathode}}\right)\ln\left(\frac{1 + K_{CO_2}\tilde{P}^m_{CO_2,anode}}{1 + K_{CO_2}\tilde{P}^m_{CO_2,cathode}}\right) \tag{2.30}$$

Increased absorbent affinity, K_{CO_2}, while negatively effecting the cell voltage improves the faradaic efficiency. In fact, if one takes equation 2.30 in the limit as binding affinity approaches infinity, the result is the thermodynamic minimum work required for separation of a small amount of CO_2 from a stream.

$$\lim_{K_{CO_2}\to\infty} \bar{W} = RT\ln\left(\frac{P_{CO_2,anode}}{P_{CO_2,cathode}}\right)$$

The relationship between absorbent affinity and system efficiency is given in Figure 2-4.

Two, Three, and Four-Stage Geometries

When considering a flow system, like the EMAR process discussed below, generally four geometries will be considered. A two-stage system couples a cathodic absorbent activation - or blocker deactivation - with a CO_2 absorption. Similarly, at the anode for a two-stage system a desorption is coupled to an anodic deactivation of the absorbent - or blocker activation. In a four-stage system however the electrochemical steps are decoupled from the homogeneous absorption or desorption of CO_2. Two-stage and four-stage geometries may be combined to create two possible three-stage geometries by including either a cathodic absorption or an anodic desorption in an

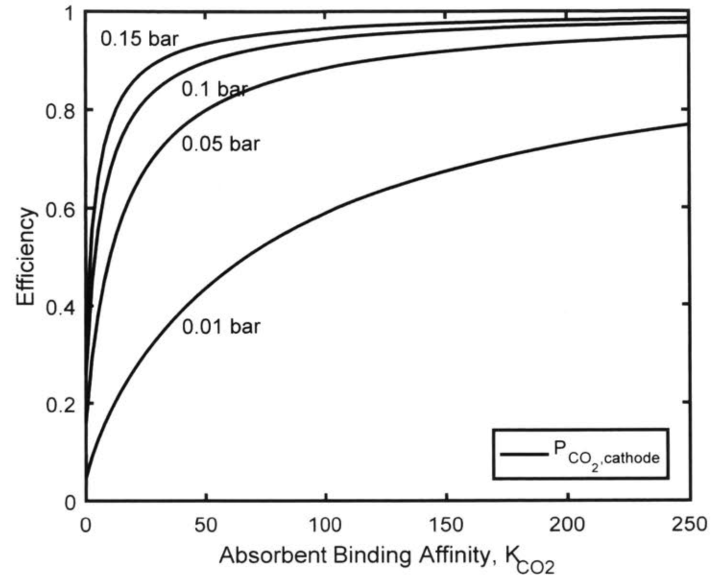

Figure 2-4: Thermodynamic separation efficiency as a function of absorbent binding affinity for a variety of cathodic CO_2 partial pressures shows increasing absorbent affinity increases system efficiency, which asymptotically approaches 1.

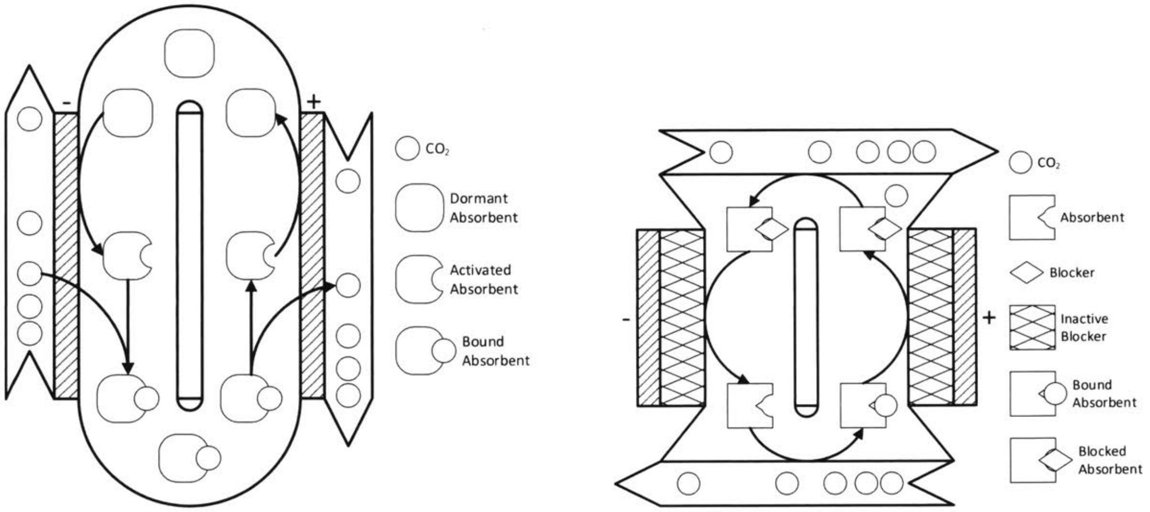

(a) Two Stage EMCS System

(b) Four Stage EMCCS System

Figure 2-5: Flow geometries for both EMCS and EMCCS systems may employ either two, three, or four-stage geometries otherwise four-stage geometry. Examples of two-stage and four-stage geometries are given in Figure 2-5.

Three simple thermodynamic pathways exist for these geometries.

Constant CO_2 Partial Pressure Seen in cathodic absorption or anodic desorption regimes, these paths maintain a constant CO_2 partial pressure while changing both state of charge and total CO_2 concentration in the liquid.

Constant Total CO_2 Concentration Seen in cathodic or anodic regimes, which do not include absorption or desorption, these paths maintain a constant total CO_2 concentration in the liquid while changing both state of charge and partial pressure of CO_2.

Constant State of Charge Seen in non-electrochemical regimes like absorption or desorption, these paths maintain a constant state of charge while changing both CO_2 partial pressure and total CO_2 concentration in the liquid.

A relationship between the open circuit potential and the state of charge of EMCS and EMCCS systems was established for constant CO_2 partial pressure paths by equation 2.27. In order to resolve the other two paths listed above it is necessary to establish a relationship between state of charge, CO_2 partial pressure, and total CO_2 concentration in the liquid. Define total carbon dioxide concentration as

$$CO_{2,0} = C_{CO_2} + mC_{A(CO_2)_m}$$

where C_{CO_2} is the dissolved, unbound carbon dioxide in solution and $C_{A(CO_2)_m}$ is the absorbent bound CO_2 as before. Notice that C_{CO_2} is related to P_{CO_2} by the Henry's

	$x_{CO_{2,0}}$	α	$\tilde{k}_{h,CO_2}$
EMCS with Inactive Absorbent in Solution	$\frac{CO_{2,0}}{mA_0}$	$x_{A'}$	$\frac{k_{h,CO_2}P_0}{mA_0}$
EMCS with Solid Inactive Absorbent	$\frac{CO_{2,0}}{mC_0}$	$\frac{A_0}{C_0}$	$\frac{k_{h,CO_2}P_0}{mC_0}$
EMCCS with Inactive Blocker in Solution	$\frac{CO_{2,0}}{mA_0}$	$1 - x_B$	$\frac{k_{h,CO_2}P_0}{mA_0}$
EMCCS with Solid Inactive Blocker	$\frac{CO_{2,0}}{mA_0}$	$1 - x_B$	$\frac{k_{h,CO_2}P_0}{mA_0}$

Table 2.1: Parameters for carbon dioxide balance given in equation 2.31.

law constant, k_{h,CO_2}, as given by

$$P_{CO_2} = \frac{C_{CO_2}}{k_{h,CO_2}}$$

For convenience we define the following relationships $\tilde{k}_{h,CO_2} = \frac{k_{h,CO_2}P_0}{mA_0}$ and $x_{CO_{2,0}} = \frac{CO_{2,0}}{mA_0}$ for all systems where total absorbent concentration remains constant. For systems where absorbent concentration changes, i.e. EMCS with solid inactive absorbent, define $\tilde{k}_{h,CO_2} = \frac{k_{h,CO_2}P_0}{mC_0}$ and $x_{CO_{2,0}} = \frac{CO_{2,0}}{mC_0}$. As shown in Appendix B the relationship between state of charge, CO$_2$ partial pressure, and total CO$_2$ concentration is given in equation 2.31, whose α parameter is established in Table 2.1. Notice that α in equation 2.31 indicates the systems' state of charge.

$$x_{CO_{2,0}} = \alpha \frac{K_{CO_2}\tilde{P}^m_{CO_2}}{1 + K_{CO_2}\tilde{P}^m_{CO_2}} + \tilde{k}_{h,CO_2}\tilde{P}_{CO_2} \tag{2.31}$$

Equation 2.27 in concert with equation 2.1 allows us to establish a relationship between deviation potential, E^{dev}, and state of charge for which α is a proxy for all three simple paths described above. Figure 2-6 gives an example cycle for a three-stage geometry electrochemical CO$_2$ separation employing an anodic desorption. This ar-

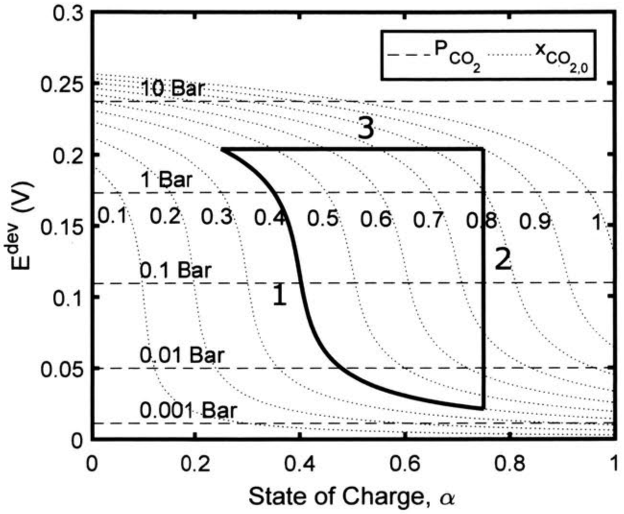

Figure 2-6: E^{dev} as a function of state of charge, α, for an example three-stage electrochemical CO_2 separation. (1) Constant $x_{CO_{2,0}}$ cathodic path. (2) Constant state of charge absorption. (3) Constant partial pressure anodic desorption.

chitecture is similar to the EMAR architecture whose thermodynamics are explored in detail in the following chapters. The total work for separation for an electrochemical cycle is defined by the path integral of the open circuit potential vs state of charge - which was established by equations 2.5, 2.10, 2.17, and 2.24 and is proportional to α - as given by equation 3.14. The result is the total work of separation is proportional to the shaded areas shown in Figure 2-7.

$$W = \oint E \, \mathrm{d}Q = \oint E^{dev} \, \mathrm{d}Q \tag{2.32}$$

Figure 2-7 demonstrates the effect of absorbent affinity for CO_2, K_{CO_2}, and CO_2 solubility as measured by the Henry's law constant, k_{H,CO_2}, on total work of capture for a three-stage system. As shown, increasing K_{CO_2} shifts the deviation potential

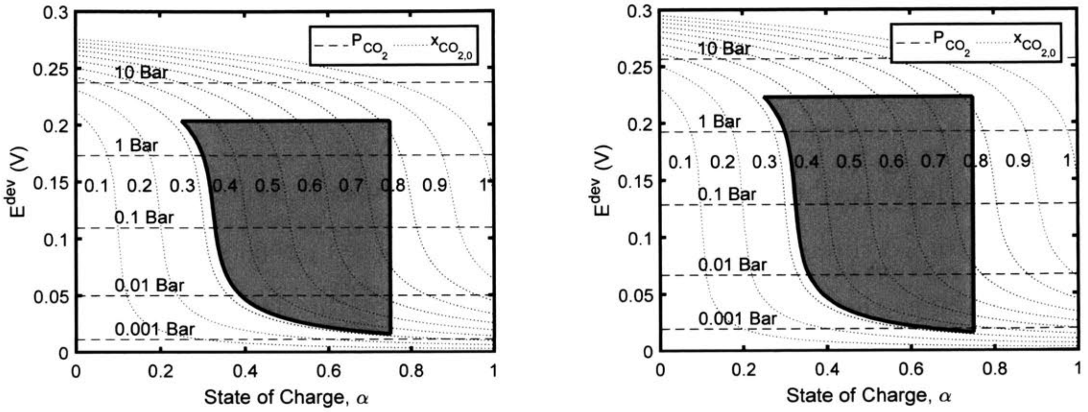

(a) $K_{CO_2} = 500$, $\tilde{k}_{H,CO_2} = 0.025$

(b) $K_{CO_2} = 1000$, $\tilde{k}_{H,CO_2} = 0.025$

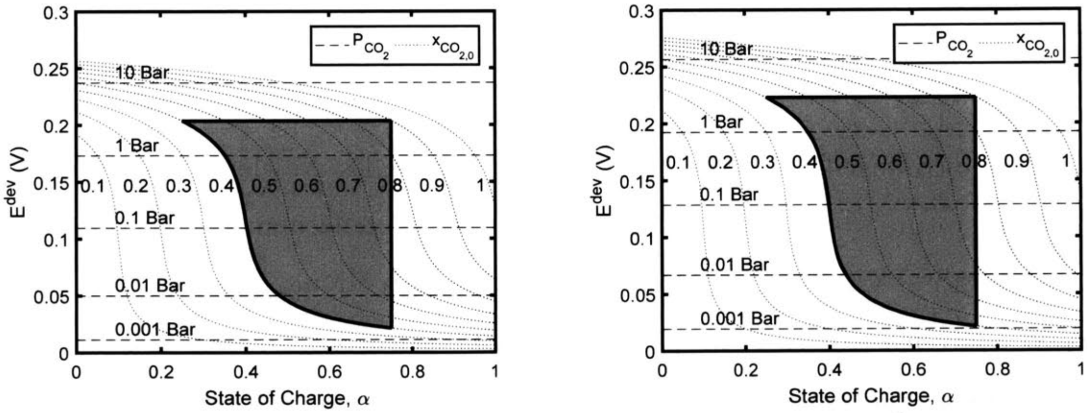

(c) $K_{CO_2} = 500$, $\tilde{k}_{H,CO_2} = 0.05$

(d) $K_{CO_2} = 1000$, $\tilde{k}_{H,CO_2} = 0.05$

Figure 2-7: Effect of absorbent affinity, K_{CO_2}, and CO_2 solubility, $\tilde{k}_{H,CO_2}$, on thermodynamic cycle shows a preference for weaker absorbent affinity and higher Henry's law constant for a three-stage system.

more positive, the result is a slight increase in the integration area and subsequently the work of capture for this particular geometry. This is in contrast to the non-flow system described previously which becomes more efficient at K_{CO_2} increases. Increasing the Henry's law constant brings the cathodic path closer to the anodic path in this geometry, thereby decreasing the work of capture.

Thermodynamics associated with the three stage EMAR geometry is discussed in detail in the following chapter. As noted there the two-stage system is, generally, more efficient than a three or four stage system, owing to the increased carbon dioxide partial pressure in the cathode. This serves to increase the cathodic equilibrium potential closer to that of the anode. EMAR is no exception.

Summary and Conclusions

This chapter introduced a framework for analyzing liquid state electrochemical carbon dioxide capture systems, which utilize a variety of molecular architectures and system geometries. Of particular concern, was the open circuit potential of a given system at a given state and the paths by which such a system traveled between states. With this information one can determine the electrochemical minimum work of capture via a path integral of the open circuit potential with respect to state of charge.

The molecular architectures described employ a concerted m electron electrochemical reaction and include:

Electrochemically-Mediated Complexation Separation (EMCS) in which a redox active absorbent is cathodically activated for capture and anodically deactivated.

Electrochemically-Mediated Competitive Complexation Separation (EMCCS) in which a redox active blocker species whose electrophilicity may be manipulated serves to bind an electrochemically inert absorbent. This blocker is activated via oxidation at the anode and subsequently deactivated via reduction at the cathode.

EMCS architectures explored in this chapter include systems where an inactive absorbent remains in solution as well as systems with solid inactive absorbents. Similarly, EMCCS architectures studied may incorporate a solid inactive blocker or a blocker which remains in solution. While the relationship between state and open circuit potential varies for the four architectures studied, a convenient simplification exists as given by equation 2.27. The deviation potential was defined as the open circuit potential difference between a given state and that same state in the absence of carbon dioxide. It was shown that for all four architectures the deviation potential was the same and was solely a function of CO_2 partial pressure, not state of charge or absorbent concentration. The deviation potential is repeated below for the reader's convenience.

$$E^{dev} = E - E|_{P_{CO_2}=0} = \frac{RT}{mF} \ln\left(1 + K_{CO_2}\tilde{P}^m_{CO_2}\right)$$

System geometries dictate thermodynamic paths taken by these electrochemical systems, which in concert with the equation given above establish the thermodynamic minimum work of capture. The system geometries studied by this chapter include:

Two-Stage which couples a cathodic absorbent activation - or blocker deactivation - with a CO_2 absorption as well as coupling an anodic absorbent deactivation - or blocker activation - with a CO_2 desorption.

Three-Stage which include either a cathodic absorption or an anodic desorption in an otherwise four-stage geometry.

Four-Stage in which the electrochemical steps are decoupled from the homogeneous absorption or desorption of CO_2.

The potential paths taken by each of these system geometries include:

Constant CO_2 Partial Pressure Seen in cathodic absorption or anodic desorption regimes, these paths maintain a constant CO_2 partial pressure while changing both state of charge and total CO_2 concentration in the liquid.

Constant Total CO_2 Concentration Seen in cathodic or anodic regimes, which do not include absorption or desorption, these paths maintain a constant total CO_2 concentration in the liquid while changing both state of charge and partial pressure of CO_2.

Constant State of Charge Seen in non-electrochemical regimes like absorption or desorption, these paths maintain a constant state of charge while changing both CO_2 partial pressure and total CO_2 concentration in the liquid.

In order to determine the open circuit potential along each of these paths equation 2.31 was established. This CO_2 mass balance related state of charge and total CO_2 concentration to CO_2 partial pressure so that equation 2.27 could be used to establish how the deviation potential changes along each of the three above paths. This CO_2

mass balance is repeated below for the reader's convenience.

$$x_{CO_{2,0}} = \alpha \frac{K_{CO_2} \tilde{P}^m_{CO_2}}{1 + K_{CO_2} \tilde{P}^m_{CO_2}} + \tilde{k}_{h,CO_2} \tilde{P}_{CO_2}$$

Here α is a proxy for state of charge and whose explicit definition is given in Table 2.1 for each molecular architecture.

It was shown that for a three-stage system with an anodic desorption, similar to that of the EMAR process discussed in the following chapters, the electrochemical cell employed became more efficient at lower absorbent binding affinities and at higher CO_2 solubilites as measured by the Henry's law constant. This was in contrast to simple, non-flow electrochemical carbon dioxide capture schemes, which as shown in Figure 2-4 improve efficiency upon increasing absorbent binding affinity.

The following chapter will build on the thermodynamic foundation established in this chapter. Specifically, Chapter 3 will analyze the thermodynamics of the EMAR process, an EMCCS architecture with a solid inactive blocker which typically employs a three-stage geometry. This endeavor will rely heavily on equation 2.25, which establish the open circuit potential for a given state, and equation 2.31, which relates three key process variables, namely state of charge, CO_2 loading, and CO_2 partial pressure.

THIS PAGE INTENTIONALLY LEFT BLANK

Chapter 3

EMAR Thermodynamics

Chapter 2 established a relationship between the state of a liquid stream and that stream's open circuit potential, for a variety of electrochemical architectures including Electrochemically-Mediated Complexation Separation (EMCS) and Electrochemically-Mediated Competitive Complexation Separation (EMCCS). That chapter went on to describe three simple thermodynamic paths which an electrochemical system make take while completing a carbon dioxide capture cycle, namely constant CO_2 partial pressure, constant CO_2 concentration, and constant state of charge. The paths were shown to arise naturally from the system geometry which may include two, three, and four-stage systems.

Electrochemically-Mediated Amine Recovery (EMAR) as first proposed by Stern et al. is an EMCCS system that employs a three-stage geometry with an anodic desorption and whose thermodynamic cycle consists of all three paths discussed above. This chapter will explore the thermodynamic cycle of an EMAR process, expanding on the framework introduced in Chapter 2. It will establish the key process variables for an EMAR stream which determine that stream's state. It will also expand upon key parameters for the EMAR system, namely amine binding affinity, K_{CO_2}, and CO_2 solubility, $\tilde{k}_{H,CO_2}$, initially introduced in the previous chapter, which affect the system's efficiency.

In addition to the thermodynamics of the electrochemical EMAR cell, auxiliary unit operations including pumps and compressors will be considered. The result will be an analysis of the total work of carbon dioxide capture for the EMAR process, which will suggest ideal unit operation configurations and operating conditions.

As discussed in Chapter 1 the redox active species in an EMAR cycle is copper, which in its oxidized state complexes with an amine absorbent. EMAR's mechanism given below is therefore similar to that provided by equation 3.1.

$$\begin{array}{lll}
\text{Electrochemical} & \mathrm{Cu^{2+}(aq) + 2\,e^- \rightleftharpoons Cu(s)} & \text{(a)} \\
 & E = E^\circ - \frac{RT}{2F} \ln\left(\frac{C_0}{C_{Cu^{2+}}}\right) & \\
\text{Homogeneous} & \mathrm{Am(aq) + mCO_2(g) \rightleftharpoons Am(CO_2)_m(aq)} & \text{(b)} \\
 & K_{CO_2} = \frac{C_{Am(CO_2)_m}}{C_{Am}} \left(\frac{P_0}{P_{CO_2}}\right)^m & \\
\text{Homogeneous} & \mathrm{\frac{2}{m}Am(aq) + Cu^{2+}(aq) \rightleftharpoons Cu^{II}(Am)_{2/m}{}^{2+}(aq)} & \text{(c)} \\
 & \beta = \frac{C_{Cu^{II}Am^{2+}_{2/m}} C_0^{2/m}}{C_{Am}^{2/m} C_{Cu^{2+}}} &
\end{array} \qquad (3.1)$$

Stern first described the thermodynamics of the EMAR process.[1] Stern's approach however, mistreats the cathodic and anodic paths and overestimates the required work for capture, therefore the framework discussed in Chapter 2 will be used to expand and generalize Stern's work. As shown above, of key importance to any electrochemical CO_2 capture system is the affinity of the absorbent - amine in the case of EMAR - to bind CO_2, given as K_{CO_2} in equation 3.2.

$$K_{CO_2} = \frac{C_{Am(CO_2)_m}}{C_{Am}} \left(\frac{P_0}{P_{CO_2}} \right)^m \tag{3.2}$$

Using the above framework Stern's description is significantly expanded upon for the EMAR process in the sections below.

Key Process Variables

The state of any liquid stream in the EMAR process may be described by the process variables given in Table 3.1.

Total Amine Concentration	$Am_0 = C_{Am} + C_{Am(CO_2)_m} + \frac{2}{m} C_{Cu^{II}Am^{2+}_{2/m}}$
Copper Loading	$x_{Cu} = \frac{2C_{Cu^{II}Am^{2+}_{2/m}}}{mAm_0} \approx \frac{2Cu_0}{mAm_0}$
Effective CO_2 Loading	$x_{CO_{2,0}} = \frac{C_{CO_2} + mC_{Am(CO_2)m}}{mAm_0} = \frac{CO_{2,0}}{mAm_0}$
CO_2 Partial Pressure	$P_{CO_2} = \frac{C_{CO_2}}{k_{H,CO_2}}$

Table 3.1: Process variables with describe the state of a liquid EMAR stream.

The total amine concentration (Am_0) describes the total concentration of all amines in the liquid in any form (bound to carbon dioxide, bound to copper, or unbound). The copper loading (x_{Cu}) describes the fraction of those amines which are bound to copper. With the assumption that amines are in excess and the binding constant between amines and copper, β, is quite high, we have $x_{Cu} \approx \frac{2Cu_0}{mAm_0}$. Similarly the effective carbon dioxide loading ($x_{CO_{2,0}}$) may be defined has the total dissolved CO$_2$ concentration (bound or unbound to amines) normalized by the total amine concentration. Finally, the carbon dioxide partial pressure (P_{CO_2}) of any liquid EMAR stream is related to the concentration of dissolved, unbound CO$_2$ by the Henry's law constant (k_{h,CO_2}).

As shown in Appendix C, x_{Cu}, $x_{CO_{2,0}}$, and P_{CO_2} are related to each other as given by equation 3.3.

$$x_{CO_{2,0}} - \tilde{k}_{h,CO_2}\tilde{P}_{CO_2} = (1 - x_{Cu}) \left(\frac{K_{CO_2}\tilde{P}^m_{CO_2}}{1 + K_{CO_2}\tilde{P}^m_{CO_2}} \right) \tag{3.3}$$

Here $\tilde{P}_{CO_2} = \frac{P_{CO_2}}{P_0}$ is the dimensionless carbon dioxide partial pressure and $\tilde{k}_{h,CO_2} = \frac{k_{h,CO_2}P_0}{mAm_0}$ is the dimensionless Henry's law constant. Solving equation 3.3 for $x_{CO_{2,0}}$ and x_{Cu} is straight forward and is given in the Appendix C. Of key importance, as will be shown later, is solving for $\tilde{P}_{CO_2}$ for which an analytical solution, given in equation 3.4, exists for $m = 1$.

$$\tilde{P}_{CO_2} = \frac{\sqrt{b^2 + 4\tilde{k}_{h,CO_2}K_{CO_2}x_{CO_{2,0}}} - b}{2\tilde{k}_{h,CO_2}K_{CO_2}} \tag{3.4}$$

where $b = K_{CO_2}\left(1 - x_{Cu} - x_{CO_{2,0}}\right) + \tilde{k}_{h,CO_2}$.

Minimum Required Copper Loading Shift and Maximum Desorption Pressure

In order for carbon dioxide to be released from the anode, copper loading must be sufficiently increased to bring the CO_2 partial pressure of the anodic stream up to the pressure of the EMAR Cell, P_{EMAR}. Therefore, for a given desorption pressure, there is a minimum required copper loading shift before which no carbon dioxide will be released from the desorber. Similarly for a given copper loading shift, there is a maximum achievable desorption pressure. Specifically, we require that the effective CO_2 loading of the anodic outlet be less than the effective CO_2 loading of the anodic inlet. Thus, the relationship between desorption pressure and copper loading shift is a direct consequence of equation 3.3 and is given by equation 3.5

$$\begin{aligned} &(1 - x_{Cu,in}) \left(\frac{K_{CO_2} \tilde{P}_{abs}^m}{1+K_{CO_2} \tilde{P}_{abs}^m} \right) + \tilde{k}_{h,CO_2} \tilde{P}_{abs} \\ &\quad > (1 - x_{Cu,out}) \left(\frac{K_{CO_2} \tilde{P}_{EMAR}^m}{1+K_{CO_2} \tilde{P}_{EMAR}^m} \right) + \tilde{k}_{h,CO_2} \tilde{P}_{EMAR} \end{aligned} \tag{3.5}$$

This inequality may be simplified to equation 3.6 for typical conditions experienced in an EMAR cycle. See Appendix C for a detailed derivation of this simplification. The result is fairly intuitive, that we require an anime copper loading shift sufficient to bind the dissolved CO_2 in the anode at desorption pressure less the entering dissolved CO_2.

$$\Delta x_{Cu} \gtrapprox \tilde{k}_{h,CO_2} \left(\tilde{P}_{EMAR} - \tilde{P}_{abs} \right) \tag{3.6}$$

Key Parameters

As shown in equation 3.3, the amine/CO$_2$ binding constant, K_{CO_2}, and the Henry's Law constant, k_{H,CO_2}, are required to determine the state of an EMAR stream. The Henry's Law coefficient for CO$_2$ is a function of temperature and stream composition. The temperature effect may be described by the enthalpy of solution as given in equation 3.7.[35,36] A salting out effect decreases CO$_2$ solubility in aqueous streams containing electrolyte. This composition effect is a function of ionic species present and ionic strength and may be determined using equation 3.8 and Table 3.2 in conjunction.[18,37]

$$\frac{d\left(\ln\left(k_{H,CO_2}\right)\right)}{d\left(1/T\right)} = \frac{\Delta_{mix}H}{R} = 2500\,K \tag{3.7}$$

$$k_{H,elec} = 10^{\sum h_j I_j}, \quad I = \frac{1}{2}\sum C_i z_i, \quad h = h_+ + h_- \tag{3.8}$$

h_+ *(L/g ion)*		h_- *(L/g ion)*	
Na$^+$	0.091	NO$_3^-$	−0.001
K$^+$	0.074	Cl$^-$	0.021

Table 3.2: The salting out effect on CO2 solubility is described using h_+ and h_- values in conjunction with equation 3.8.

Combining the temperature and composition modifications given above results in a general description of the Henry's law coefficient for an EMAR stream given in equation 3.9.

$$k_{H,CO_2} = k_{H0,CO_2} \exp\left(\frac{d\left(\ln\left(k_{H,CO_2}\right)\right)}{d\left(1/T\right)}\left(\frac{1}{T}-\frac{1}{T_0}\right)\right) k_{H,elec} \tag{3.9}$$

In a similar manner the binding constant for the amine/CO$_2$ couple, K_{CO_2}, which is introduced in equation 3.2, is a function of both temperature and composition. In order to decouple this temperature and composition effect, consider the following equilibrium constant for amine/CO$_2$ binding which considers only aqueous species concentration, and is assumed to be a function of only temperature not stream composition.

$$K_{CO_2,aq} = \frac{C_{Am(CO_2)_m}}{C_{Am}C_{CO_2}^m} \tag{3.10}$$

Noting that $C_{CO_2} = k_{h,CO_2}P_{CO_2}$ and combining equations 3.2 and 3.10 we have the following relationship.

$$K_{CO_2} = \frac{C_{Am(CO_2)_m}}{C_{Am}}\left(\frac{P_0}{P_{CO_2}}\right)^m = \frac{C_{Am(CO_2)_m}}{C_{Am}}\left(\frac{k_{h,CO_2}P_0}{C_{CO_2}}\right)^m = K_{CO_2,aq}k_{h,CO_2}^m P_0^m$$

Consider two streams, both at the same temperature (and therefore, both with $K_{CO_2,aq}$ equal), but one without supporting electrolyte and one with supporting electrolyte. Let their binding constants be $K_{CO_2,ref}$ and K_{CO_2} respectively. Using the result from above, we have the following.

$$K_{CO_2} = K_{CO_2,ref}\left(\frac{k_{h,CO_2}}{k_{h,CO_2,ref}}\right)^m = K_{CO_2,ref}\left(k_{H,elec}\right)^m$$

As shown by Stern, $K_{CO_2,ref}$ has a temperature dependence given below.[27]

$$K_{CO_2,ref} = K_0 \exp\left(-\frac{\Delta H_{CO_2}}{RT}\right)$$

The result is the temperature and stream composition dependence of K_{CO_2} as given by

$$K_{CO_2} = K_0 \exp\left(-\frac{\Delta H_{CO_2}}{RT}\right) k_{H,elec} \tag{3.11}$$

Just as in Chapter 2, K_{CO_2} and $\tilde{k}_{H,CO_2}$ will establish the profiles of the thermodynamic paths discussed below.

Open Circuit Potential

Stern described the open circuit voltage (OCV) of an EMAR stream as a function of P_{CO_2} as given in equation 3.12 below.[27]

$$E = E^{\circ} + \frac{RT}{2F}\left[\ln\left(\frac{Cu_0}{C_0}\right) - \ln\left(1 + \frac{\beta}{C_0^{2/m}}\left[\frac{Am_0 - \frac{2}{m}Cu_0}{1 + K_{CO_2}\left(P_{CO_2}/P_0\right)^m}\right]^{2/m}\right)\right] \tag{3.12}$$

This may be expressed as in equation 3.13 using the dimensionless variables and parameters described above. Notice this is simply an instance of equation 2.25 expressed in terms of the key process variables discussed above.

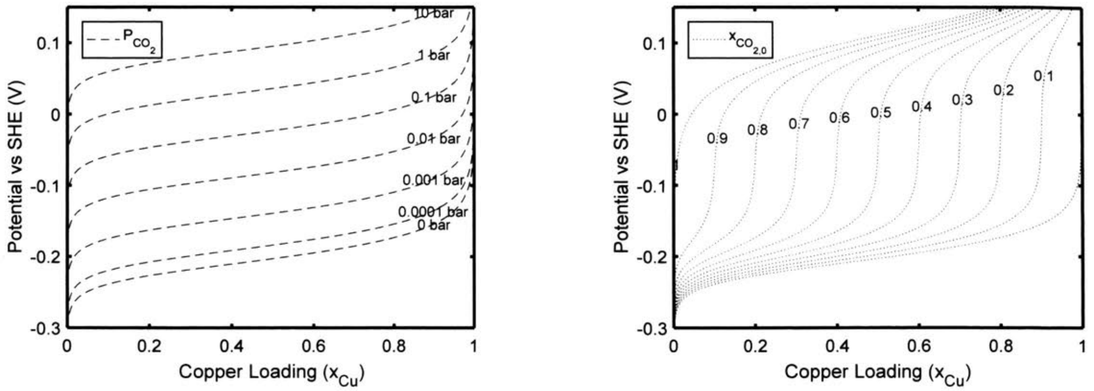

(a) Constant P_{CO_2} (b) Constant $x_{CO_{2,0}}$

Figure 3-1: Open circuit potential versus the standard hydrogen electrode of an EMAR solution as a function of copper loading for: (a) constant carbon dioxide partial pressure, (b) constant effective carbon dioxide loading.

$$E = E^{\circ} + \frac{RT}{2F}\left[\ln\left(x_{cu}\right) + \ln\left(\frac{m\tilde{Am}_0}{2}\right) - \ln\left(1+\beta\left[\frac{\tilde{Am}_0\left(1-x_{Cu}\right)}{1+K_{CO_2}\tilde{P}^{m}_{CO_2}}\right]^{2/m}\right)\right] \tag{3.13}$$

Where $\tilde{Am}_0 = Am_0/C_0$. Note that C_0 is the standard concentration for which β is described in equation 3.1b.

Equation 3.13 may be used to establish constant P_{CO_2} profiles for open circuit potential as a function of copper loading as given in Figure 3-1a. Similarly, equation 3.13 may be combined with equation 3.4 to create constant effective CO_2 profiles for OCV as given by Figure 3-1b. These two may be used in concert to establish a thermodynamic cycle for EMAR, which will define the work of regeneration as given by equation 3.14.

$$W = \oint E \,\mathrm{d}Q = F \cdot Am_0 \oint E \,\mathrm{d}x_{Cu} = F \cdot Am_0 \int_{x_{Cu,min}}^{x_{Cu,max}} (E_a - E_c)\, dx_{Cu} \tag{3.14}$$

where W is the work required for regeneration, Q is the state of charge, $x_{Cu,min}$ and $x_{Cu,max}$ are the anodic inlet copper loading and cathodic inlet copper loading respectively, and E_a and E_c are the open circuit potentials, which change with copper loading, for the anodic and cathodic flows respectively.

Anodic and Cathodic Paths

The EMAR process as shown in Figure 3-2a traverses three states, represented by streams 1, 2, and 3. The anodic channel connects states 1 and 2, call this the anodic path. Similarly, call the cathodic path and the absorber path the paths connecting states 2 and 3 and states 3 and 1 respectively.

Leaving the absorber liquid is in equilibrium with the feed gas stream, which has a CO_2 partial pressure of $P_{abs} = y_{CO_2,feed} \cdot P_{abs,total}$. As this liquid enters the anode copper metal is corroded resulting in cupric ions, which bind amines as shown in equation 3.15. This in turn increases the partial pressure of CO_2, P_{CO_2}, in the liquid.

$$\frac{2}{\mathrm{m}}\mathrm{Am(CO_2)_m(aq)} + \mathrm{Cu(s)} \rightleftharpoons \mathrm{Cu^{II}Am_{2/m}}^{2+}\mathrm{(aq)} + 2\,\mathrm{CO_2(aq)} + 2\,\mathrm{e^-} \tag{3.15}$$

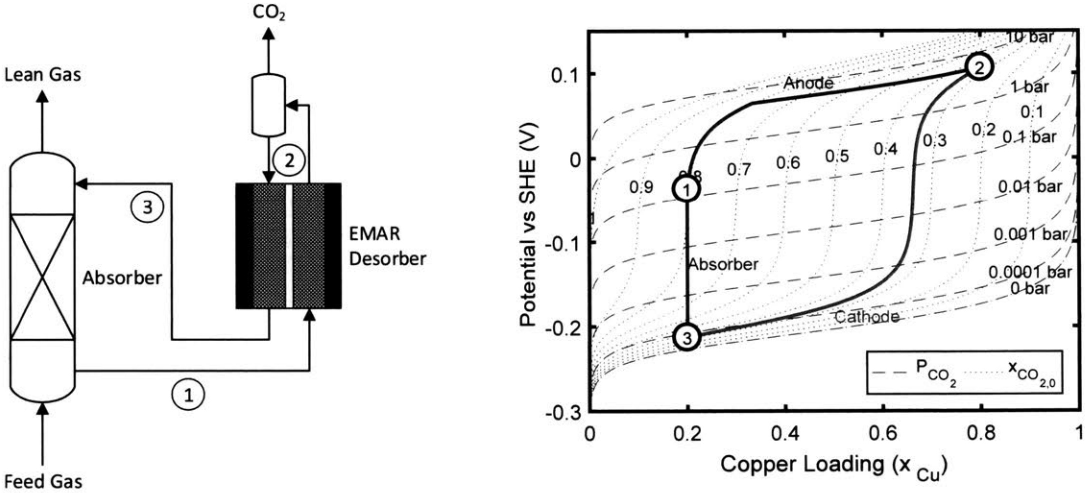

(a) EMAR Process Flow Diagram

(b) EMAR Cycle OCV

Figure 3-2: EMAR thermodynamic cycle expressed as open circuit potential versus the standard hydrogen electrode of an EMAR solution as a function of copper loading at three system states, as shown in (a): (1) exiting the absorber and entering the anode, (2) exiting the anode and entering the cathode, (3) exiting the cathode and entering the absorber. Anodic (1 → 2), cathodic (2 → 3), and absorber paths (3 → 1) are shown in (b).

Let the total pressure of the EMAR cell be P_{EMAR} and note $P_{abs} < P_{EMAR}$ - otherwise we have a pressure swing absorption process. When a copper loading shift occurs sufficient to increase P_{CO_2} to match P_{EMAR}, CO_2 gas begins to evolve and P_{CO_2} remains constant. Carbon dioxide leaving the liquid decreases effective CO_2 loading, $x_{CO_{2,0}}$, as more copper is added. The anodic path therefore has two stages, which are reflected in Figure 3-2b.

Stage 1 Constant effective CO_2 loading path, while partial pressure of CO_2 increases from P_{abs} to P_{EMAR}

Stage 2 Constant partial pressure of CO_2 at P_{EMAR} path, while effective CO_2 loading decreases

The cathodic path is more simple, as no carbon dioxide is evolved. After the stream exiting the anode is stripped of gaseous CO_2 in the gas/liquid separator, the liquid enters the cathode where the electrochemical reaction given in equation 3.16 occurs. The decreasing copper loading decreases P_{CO_2}, while effective CO_2 loading remains constant as no carbon dioxide has entered or left the liquid. Therefore the cathodic path, by contrast to the anodic path, is a single continuous stage.

$$\mathrm{Cu^{II}Am_{2/m}}^{2+}\mathrm{(aq)} + 2\,\mathrm{CO_2(aq)} + 2\,\mathrm{e^-} \rightleftharpoons \frac{2}{\mathrm{m}}\mathrm{Am(CO_2)_m(aq)} + \mathrm{Cu(s)} \qquad (3.16)$$

Liquid leaving the cathode has free amines available to bind CO_2 in the absorber, where no electrochemical reaction occurs. Thus the absorber path increases P_{CO_2} and $x_{CO_{2,0}}$ in the stream at a constant copper loading, i.e. a constant state of charge.

The now completed thermodynamic cycle is given in Figure 3-2.

Work of Regeneration, Compression, and Pumping

The thermodynamic work of amine regeneration and CO_2 release is a function of the path integral of the EMAR cycle as given by equation 3.14. However, two other unit operations draw power in the EMAR process: the pump and the compressor. These unit operations are shown in Figure 3-4a. The compressor increases outlet CO_2 pressure from P_{EMAR} to storage pressure, P_{store}. The pump circulates the EMAR liquid and raises its pressure from absorption pressure (likely atmospheric) to P_{EMAR} before entering the desorber. Pump work per mole of CO_2 captured is given by equation 3.17. For simplicity isothermal compression is assumed to calculate the work of compression per mole of CO_2 captured.

$$\bar{W}_{pump} = \frac{P_{EMAR} - P_{Abs}}{Am_0 \cdot \left(x_{CO_{2,0},anode,in} - x_{CO_{2,0},cathode}\right)} \tag{3.17}$$

By considering the work of regeneration, pumping, and compression, we can analyze the effect of copper loading shift and EMAR desorption pressure, among other variables, on the total work of CO_2 capture. A sample of this analysis is given in Figure 3-3. As seen in Figure 3-3a for a given EMAR desorption pressure, an ideal copper loading shift exists, though the effect of copper loading shift on the total work of the system is minimal. At low copper loading shifts, the electrochemical work of capture is minimized, however pump work is increased significantly especially as the copper loading shift approaches minimum given in equation 3. This asymptotic behavior is

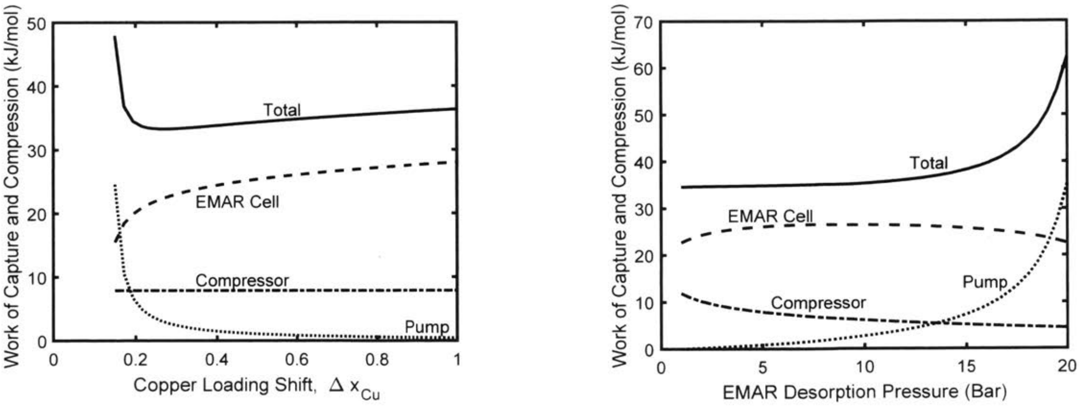

(a) Effect of copper loading shift for desorption at 5 bar.

(b) Effect of desorption pressure for copper loading shift from 20% to 80%

Figure 3-3: Work of capture and compression versus (a) copper loading shift and (b) desorption pressure for EMAR cell, compressor, and pump unit operations.

clear from the denominator of equation 3.17.

EMAR desorption pressure unlike copper loading shift has a significant effect on total work of capture as shown in Figure 3-3b. An increase in EMAR desorption pressure results in an increase in total work of capture, dominated at high desorption pressures by the work of pumping. Not only does a higher desorption pressure require a higher outlet pump pressure, but the additional dissolved CO_2 in the anode - i.e. CO_2 not released by the desorption - requires additional volumetric flow to pass through the pump. These two effects compound each other. Naturally, increasing desorption pressure decreases compression work, not enough however to compensate for the increased pump work. That said, only a minimal thermodynamic penalty is applied on desorption pressures up to 10 bar for the 60% copper loading shift tested.

An analysis similar to that seen in Figure 3-3 may be employed for all desorption pressures and copper loading shifts within the EMAR operating window defined by

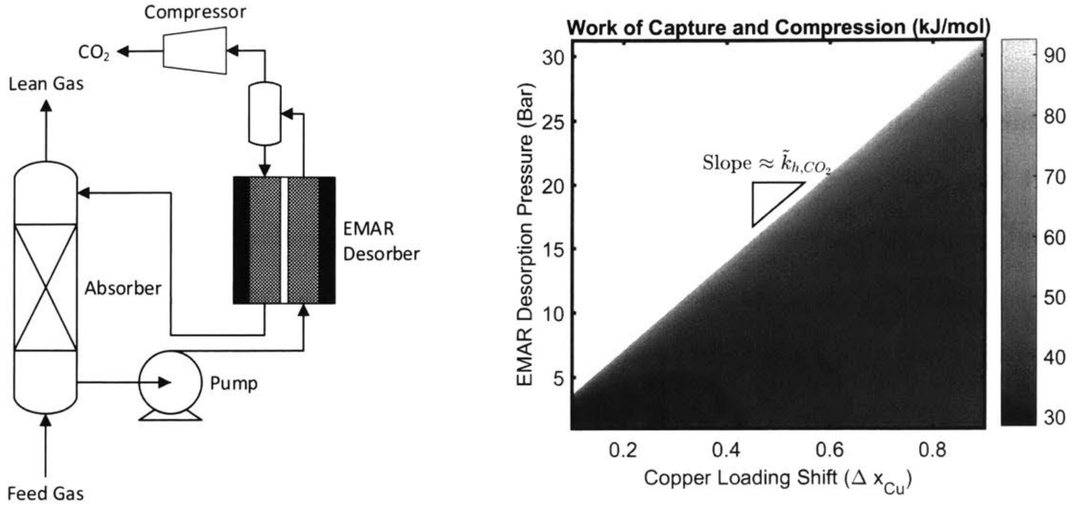

(a) Process flow diagram for EMAR.

(b) Effect of desorption pressure and copper loading shift on total work.

Figure 3-4: For EMAR cycle (a) consisting of EMAR cell, pump, and compressor, (b) total work of capture and compression versus copper loading shift and desorption pressure for EMAR.

equation 3.6. The result is the heat map given in Figure 3-4b. As expected, generally lower copper loading shifts and lower EMAR desorption pressures are preferred form an operational cost standpoint, though very little penalty exists for high copper loading shifts or moderate desorption pressures. We expect capital costs on the other hand to display the opposite behavior from the operational costs, requiring a smaller absorber as copper loading shifts increase and a smaller compressor as desorption pressures increase.

Other Geometries

The simplest possible EMAR geometry, shown in Figure 3-4a, has been considered above. It is worth considering then more complex geometries. The first geometry considered below is a secondary flash, in which physically dissolved CO_2 remaining in the liquid phase after the primary gas liquid separator is removed by a secondary, low pressure flash. This will be shown to be an ineffective approach. What will be shown to be effective is a novel cathodic absorption, which will be presented after the secondary flash geometry.

Secondary Flash

The addition of a secondary flash as seen in the process flow diagram in Figure 3-5a is designed to remove physically dissolved CO_2 remaining in the liquid phase after the primary gas liquid separation. The resulting electrochemical cycle, seen in Figure 3-5b, has one more state than then simple EMAR cycle shown in Figure 3-2b, as the cathodic inlet is now at a lower CO_2 partial pressure than the anodic outlet. A constant state of charge path is taken between these states with CO_2 partial pressure dropping from P_{EMAR} the secondary flash pressure. While this does result in additional CO_2 release - notice the lower effective CO_2 loading after the secondary flash in Figure 3-5b - there is an increase in electrochemical work of capture as evidenced by the increased area between the anodic and cathodic paths.

The secondary flash necessitates two additional unit operations, a pump and a compressor, as shown in Figure 3-6a. The compressor brings the low pressure CO_2 stream up to P_{EMAR}, whereas the pump returns liquid stream to that same pressure. As

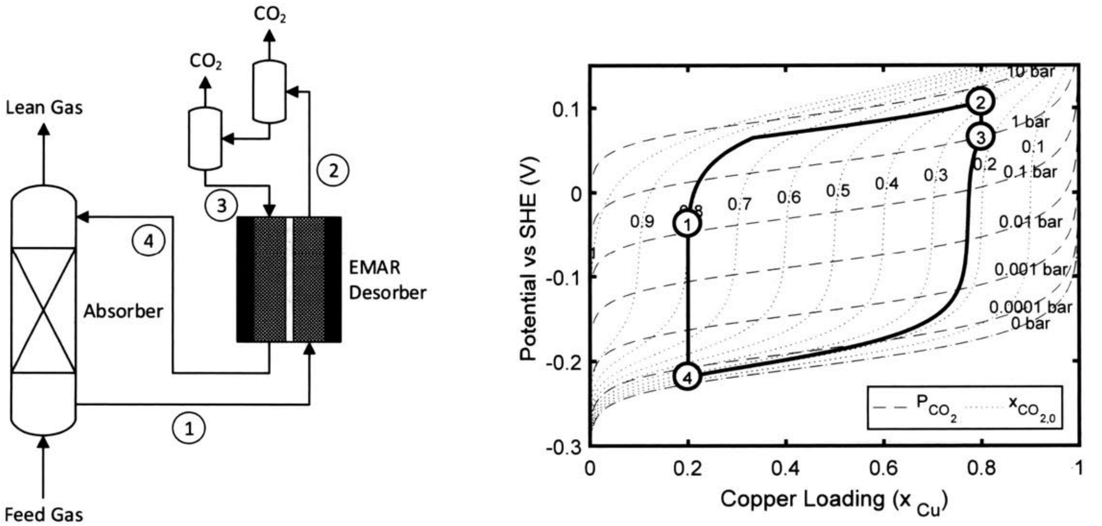

(a) EMAR process flow diagram with low pressure flash

(b) EMAR cycle OCV with low pressure flash

Figure 3-5: EMAR thermodynamic cycle expressed as open circuit potential versus the standard hydrogen electrode of an EMAR solution as a function of copper loading at four system states, as shown in (a): (1) exiting the absorber and entering the anode, (2) exiting the anode, (3) entering the cathode after a second low pressure flash, (4) exiting the cathode and entering the absorber. Anodic $(1 \rightarrow 2)$, cathodic $(3 \rightarrow 4)$, and partial pressure change paths $(2 \rightarrow 3$ and $4 \rightarrow 1)$ are shown in (b).

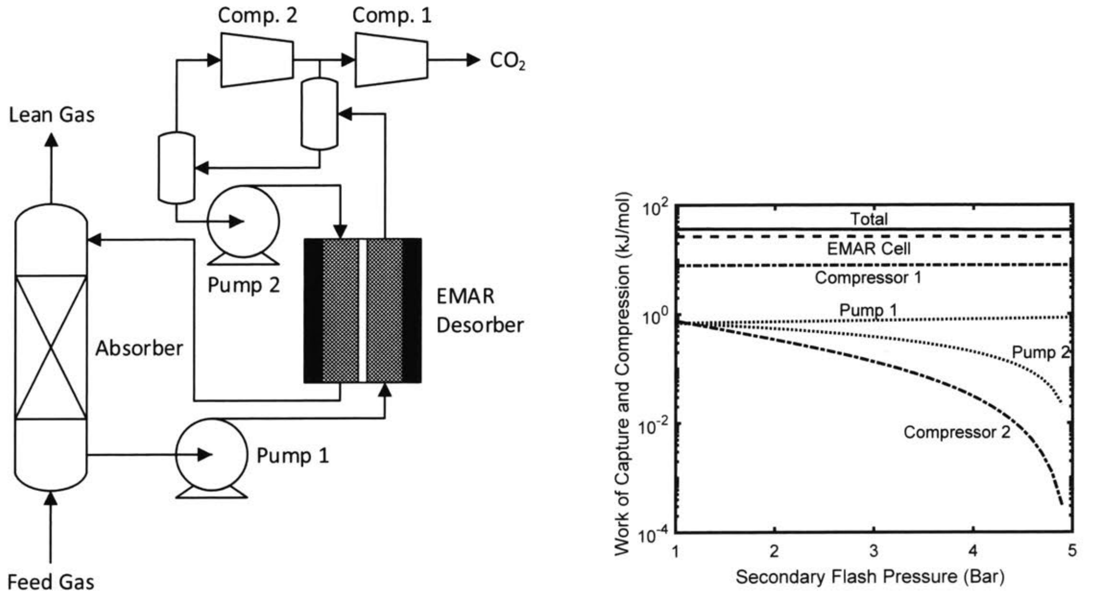

(a) Detailed EMAR process flow diagram with low pressure flash

(b) Effect of secondary flash pressure, given an EMAR pressure of 5 bar

Figure 3-6: The addition of a secondary flash to strip additional, low pressure CO_2 from anode outlet requires slightly more total work than a system without the secondary flash.

discussed above this secondary flash increases the electrochemical work of capture, while releasing additional CO_2, the result is a net little change in the molar electrochemical work of capture for the EMAR cell. However, the additional pump and compressor require addition work as secondary flash pressure decreases. Thus, the addition of a secondary flash serves only to slightly increase operating and capital cost.

Cathodic Absorption

As indication in Chapter 2, transitioning the EMAR cycle from a three-stage system to a two-stage system, through the addition of a cathodic absorber significantly improves the minimum work of capture. This could be accomplished by introducing hollow fibers or some other monolithic membrane absorption structure into the cathodic channel. This would modify the cathodic path, changing it from a constant effective CO_2 loading, $x_{CO_{2,0}}$, path to a path with much higher CO_2 partial pressure. Further, the constant state of charge absorption path would be removed. The result shown, in Figure 3-7, is a shift of the cathodic path towards a much less negative OCV, bringing the cathodic OCV closer to that of the anodic path. The decrease in the electrochemical work of capture significantly increases the efficiency of the EMAR cycle. The EMAR cycle with cathodic absorption is then similar to that presented in Figure 2-3 from Chapter 2. The incorporation of a cathodic absorption may also serve to decrease capital cost through process intensification.

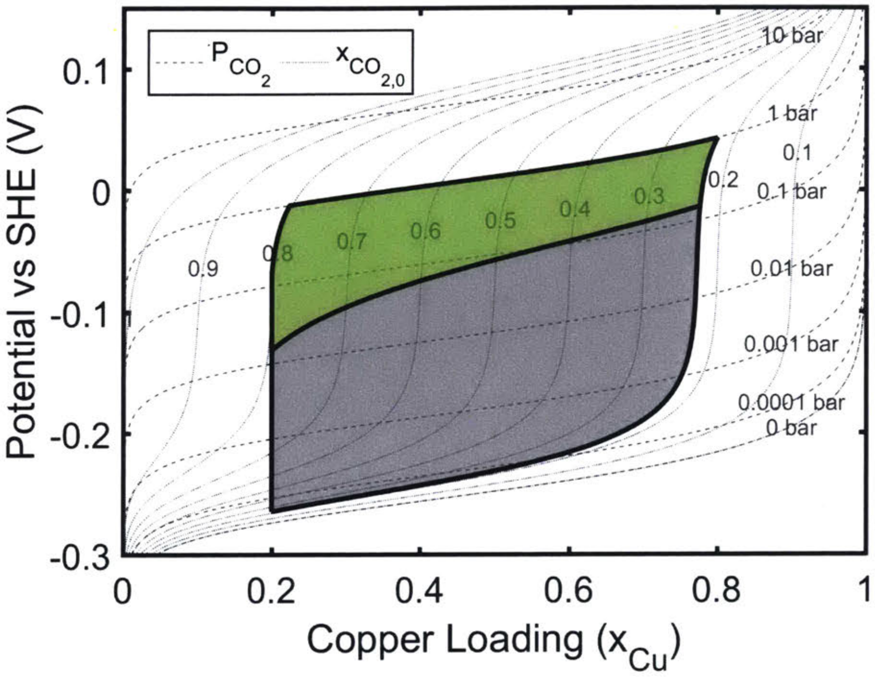

Figure 3-7: Work of EMAR cycle with combined absorber and cathode (green) is notably less than the cycle work with separate absorber and cathode (gray + green).

Summary and Conclusions

This chapter significantly expanded on Stern's thermodynamic analysis of the EMAR process using the thermodynamic framework created in Chapter 2.[27] The four key process variables, three of which are independent, provided below were established to describe the state of an EMAR stream.

Total Amine Concentration	$Am_0 = C_{Am} + C_{Am(CO_2)_m} + \frac{2}{m} C_{Cu^{II} Am^{2+}_{2/m}}$
Copper Loading	$x_{Cu} = \frac{2C_{Cu^{II} Am^{2+}_{2/m}}}{mAm_0} \approx \frac{2Cu_0}{mAm_0}$
Effective CO_2 Loading	$x_{CO_{2,0}} = \frac{C_{CO_2} + mC_{Am(CO_2)m}}{mAm_0} = \frac{CO_{2,0}}{mAm_0}$
CO_2Partial Pressure	$P_{CO_2} = \frac{C_{CO_2}}{k_{H,CO_2}}$

Using results from Chapter 2, the relationship between copper loading, effective CO_2 loading, and CO_2 partial pressure was defined. That relationship is given below.

$$x_{CO_{2,0}} - \tilde{k}_{h,CO_2} \tilde{P}_{CO_2} = (1 - x_{Cu}) \left(\frac{K_{CO_2} \tilde{P}^m_{CO_2}}{1 + K_{CO_2} \tilde{P}^m_{CO_2}} \right)$$

Further, it was demonstrated that stream composition as well as temperature impacts the key process parameters of amine/CO_2 binding affinity, K_{CO_2}, as well as the Henry's law coefficient, k_{H,CO_2}. As demonstrated in Chapter 2, these process parameters have a significant impact on the electrochemical work of separation for a three-stage electrochemical carbon dioxide separations scheme like EMAR.

In order to determine the open circuit voltage (OCV) of an EMAR stream at a given state Stern presented a relationship between OCV and CO_2 partial pressure.[27] A non-dimensional version of that relationship is provided below.

$$E = E^{\circ} + \frac{RT}{2F}\left[\ln\left(x_{cu}\right) + \ln\left(\frac{m\tilde{A}m_0}{2}\right) - \ln\left(1 + \beta\left[\frac{\tilde{A}m_0\left(1 - x_{Cu}\right)}{1 + K_{CO_2}\tilde{P}^{m}_{CO_2}}\right]^{2/m}\right)\right]$$

Stern went on to describe the paths between states in an EMAR cycle as a series of constant carbon dioxide partial pressure paths.[27] This work expanded on that approach by defining three paths, anodic, cathodic, and absorption. The anodic path increased the copper loading, i.e. the state of charge, and consisted of two stages.

Stage 1 Constant effective CO_2 loading path, while partial pressure of CO_2 increases from P_{abs} to P_{EMAR}

Stage 2 Constant partial pressure of CO_2 at P_{EMAR} path, while effective CO_2 loading decreases

After a gas/liquid separation, which did not affect the state of the liquid EMAR stream, the cathodic path decreased the copper loading along a constant effective CO_2 loading path. As a result, the CO_2 partial pressure, and thus the stream's OCV, decreased. Finally, a constant state of charge absorption path increased the EMAR stream's partial pressure to that which entered the anodic channel.

Using this thermodynamic framework it was shown that the total work of separation, i.e. regeneration, compression, and pumping, is dependent upon copper loading shift in the cell as well as desorption pressure. Pump work was especially sensitive to these operating conditions. It was shown that significant penalty is applied to EMAR systems which operate near boundary of the EMAR operating space given by the inequality below.

$$\Delta x_{Cu} \gtrapprox \tilde{k}_{h,CO_2}\left(\tilde{P}_{EMAR} - \tilde{P}_{abs}\right)$$

Two additional EMAR process flows/system geometries were considered by this chapter. It was shown that a secondary flash, which may enable the removal of additional physically dissolved carbon dioxide from the desorber, is less efficient that the traditional EMAR process flow scheme. However, it was demonstrated that pivoting EMAR from a three-stage geometry to a two-stage geometry by incorporating a cathodic absorption significantly improves thermodynamic efficiency of the cycle to say nothing of the potential capital savings from process intensification.

The next chapter will explore transport phenomena with in an EMAR cell. Electrochemical kinetics within the EMAR cell are highly dependent on the OCV established in this chapter. Unlike this chapter however, which describes the EMAR process on a macro-scale, the following chapter explores transport behavior on a micro-scale with specific emphasis on temperature distribution in an EMAR unit cell.

THIS PAGE INTENTIONALLY LEFT BLANK

Chapter 4

Transport Phenomena within an EMAR Cell

Stern showed that the electrochemical kinetics of EMAR are highly temperature sensitive, especially the cathodic reaction as seen in Figure 4-1. It is clear then that temperature excursions, especially cooling, are of concern for the EMAR process. This is compounded by the fact that the overall desorption reaction given below is endothermic - as the absorption was exothermic - with a heat of reaction of 84 kJ/mol for a system using an EDA sorbent.[38]

$$\text{(EDA)CO}_2 \longrightarrow \text{EDA} + \text{CO}_2 \quad \Delta H_{CO_2} = 84\, kJ/mol$$

As demonstrated by Stern, the temperature change in an EMAR cell is a function of the voltage applied, ΔV, and the copper loading shift, Δx_{Cu}, as well as this heat of reaction.[1]

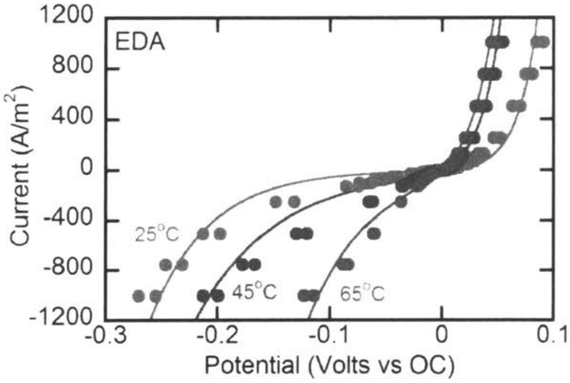

Figure 4-1: Current density as a function of over potential for an EMAR solution at a variety of temperatures reveals temperature has a significant impact on electrochemical kinetics for EMAR. This figure is reproduced from Stern's PhD thesis.[1]

$$\Delta T_{cell} = \frac{Am_0 \left(-\Delta H_{CO_2} + F\Delta V_{cell}\right) \Delta x_{Cu}}{c_p}$$

While the endothermic reaction, denoted by the $-\Delta H_{CO_2}$ term, serves to cool the stream, joule heating, denoted by the $F\Delta V_{cell}$ term, serves to reheat the solution. For moderate unit cell voltages of around 0.5 V this may serve to decrease the temperature of a stream entering the EMAR desorber by 20 °C. For a high voltage of 1.0 V, the joule heating will dominate and increase the stream temperature by about 5 °C.

While we expect the anodic reaction which breaks an amine/CO_2 bond and forms an amine/copper bond to be slightly endothermic, we expect the cathodic reaction to be significantly endothermic, representing the bulk of the required 84 kJ/mol. As the cathodic reaction is the most temperature sensitive, this is of particular concern. Thus, this chapter discusses a coupled mass and heat transfer model for the flat plate EMAR process, which will serve provide better understanding of the heat effects on an EMAR system and allow for optimization.

This model has been designed for a flat plate system in either a parallel or series configuration. Details of the model including system geometry, governing equations, and boundary conditions are discussed below. Further, the results of the model will be compared to experimental results for validation purposes.

System Geometry

As will be discussed in Chapter 5, scaling up of the EMAR process will require assembling the electrochemical system into a stack. Two possible system geometries exist for an EMAR stack shown in Figures 4-2 and 4-3. The two geometries, parallel and series, each have the same unit cell which will be described by the model below. In parallel each copper plate has an external voltage applied to it, alternating from positive to negative. In series potential is applied only at the ends of a stack, making each copper plate bipolar. These bipolar plates undergo anodic and cathodic reactions on either side which carries the current from cell to cell. For n cells in a stack each with a voltage V and current I, the series configuration requires nV total potential and I total current, whereas the parallel configuration requires V total potential and nI total current. Both have the same power requirements.

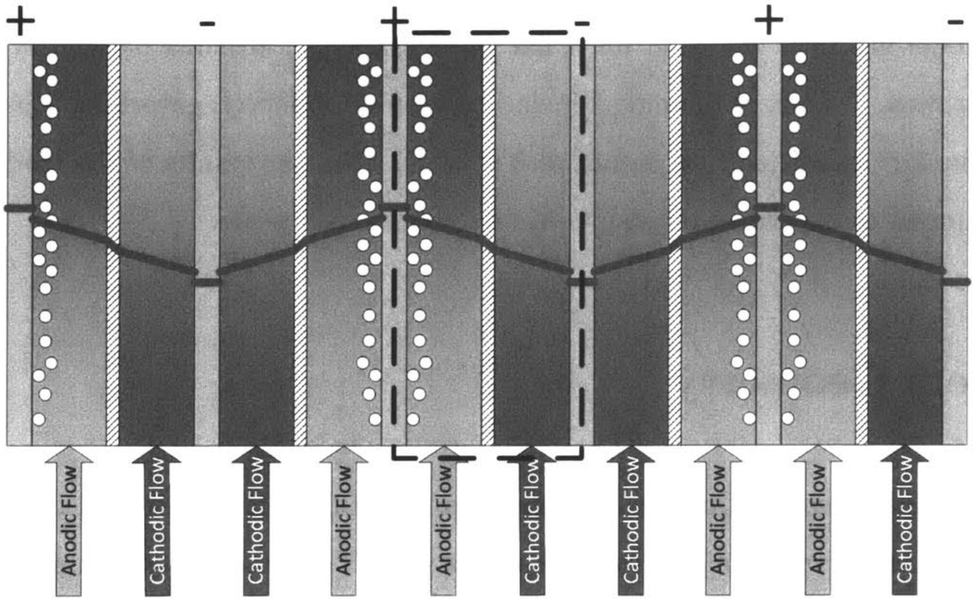

Figure 4-2: Parallel EMAR geometry with voltage shown in maroon and unit cell boxed

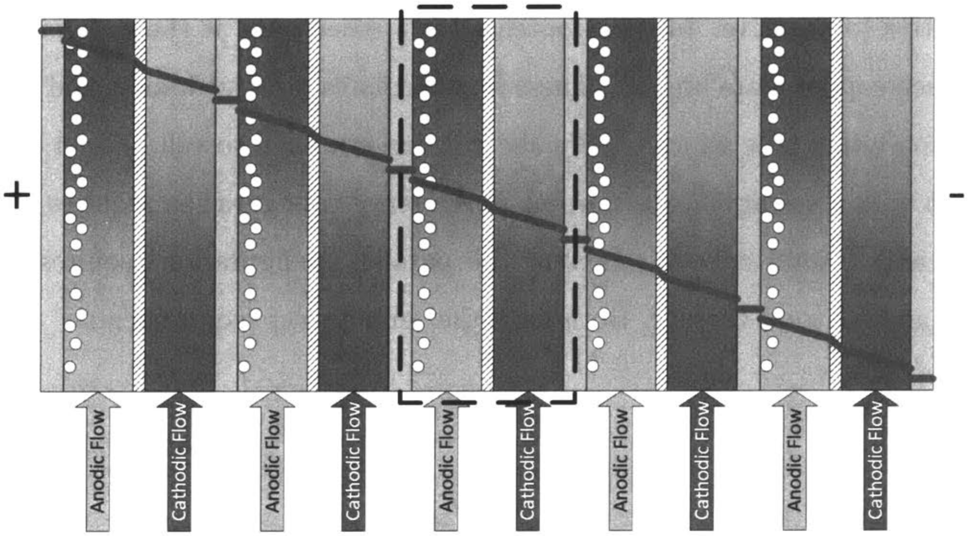

Figure 4-3: Series EMAR geometry with voltage shown in maroon and unit cell boxed

Each unit cell consist of five components, listed from left to right below.

Anode The electrode in which the anodic reaction occurs, increasing the copper loading in the anodic channel and releasing CO_2

Anodic Channel The channel in which EMAR solution is exposed to the anode

Membrane A stagnant separator dividing the anodic and cathodic channels

Cathodic Channel The channel in which EMAR solution is exposed to the cathode

Cathode The electrode in which the cathodic reaction occurs, decreasing the copper loading in the cathodic channel and freeing amines to capture CO_2

The model detailed below will consider the transport phenomena within the anodic and cathodic channels as well as the membrane. The channels will be treated as open, free for liquid to flow through, whereas the membrane will be treated as a stagnant porous separator. The electrodes on the other hand will be treated as boundaries. Notice that the unit cells for each configuration are identical, with the exception of the electrode boundaries. In the parallel conformation both the anode and cathode boundaries are symmetric, whereas the series conformation has a periodic boundary condition at the electrodes. The resulting unit cell geometry including boundaries and regions is given in Figure 4-3.

Model Overview

Generally, an electrochemical transport model can be thought of as a division of applied unit cell potential, ΔV_{cell}, into overpotentials as given below.

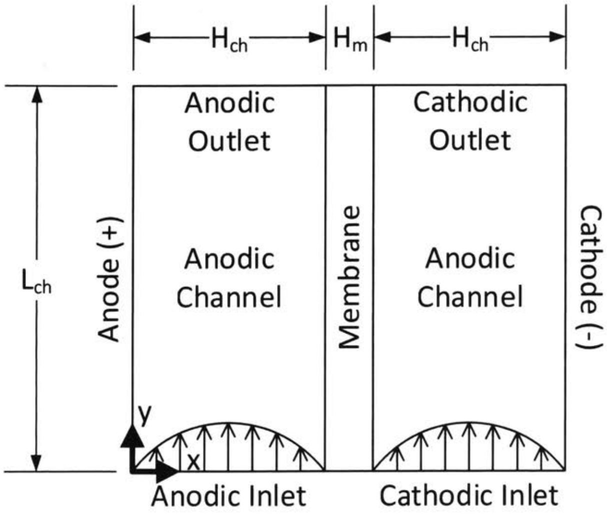

Figure 4-4: Unit cell geometry for EMAR transport model labeling both boundaries and regions.

$$\Delta V_{cell} = \Delta E_{eq} + \eta_{RXN} + \eta_{trans}$$

Chapter 3 discussed the thermodynamic overpotential, ΔE_{eq}, which will be of key importance to this transport phenomena model. Aside from the minimum required potential to complete the separation, electrical energy goes towards driving the electrochemical reaction at the anodic and cathodic boundaries, η_{RXN}, and transporting redox active species or supporting electrolyte through boundary layers or the bulk. This model will lump together transport resistances, which traditionally consider transport though a boundary layer, and ohmic resistances, which consider transport through the bulk, into simply η_{trans} described by species and charge conservation equations.

Boundary conditions will describe η_{RXN} by applying the Butler-Volmer equation to the electrochemical reaction in equation 4.1.

$$\mathrm{AmCu^{2+}(aq)} + 2\,\mathrm{e^-} + (\mathrm{CO_2}) \rightleftharpoons \mathrm{Am}*\,\mathrm{(aq)} + \mathrm{Cu(s)} \tag{4.1}$$

where Am$*$ represents all non-copper bound amines, that is free or bound to CO_2. As in the thermodynamic section, CO_2 will be accounted for as a partial pressure of CO_2, thus the parenthesis above.

Species Considered

This model will explicitly track four chemical species throughout the geometry given by Figure 4-3. These include the two aqueous species given in equation 4.1 as well as cationic and anionic supporting electrolytes. In post processing, we may determine the concentration of other species of interest by considering the amine binding affinity relationship, equation 3.1b from Chapter 3, given below for convenience.

$$K_{CO_2} = \frac{c_{Am(CO_2)_m}}{c_{Am}} \left(\frac{P_0}{P_{CO_2}} \right)^m$$

Applying the definition supplied above, namely $c_{Am*} = c_{Am} + c_{Am(CO_2)_m}$, we may extract the following relationships based solely on amine binding affinity, CO_2 partial pressure, and total non-copper bound amine concentration. Notice, as defined in Chapter 2, $\tilde{P}_{CO_2} = P_{CO_2}/P_0$.

$$c_{Am(CO_2)_m} = \frac{K_{CO_2}\tilde{P}_{CO_2}}{1 + K_{CO_2}\tilde{P}_{CO_2}} c_{Am*} \tag{4.2}$$

$$c_{Am} = \frac{1}{1 + K_{CO_2}\tilde{P}_{CO_2}} c_{Am*} \qquad (4.3)$$

As in Chapter 3 dissolved, unbound CO_2 concentration may be monitored with the Henry's law coefficient and the partial pressure.

Assumptions to be Made

The model described below assumes that the CO_2 partial pressure is maintained at $P_{CO_2,anode}$ throughout the anodic chamber, this is constant with most of the anodic path for the EMAR process shown in Chapter 3. Further it is assumed that total effective CO_2 loading remains constant throughout the cathodic chamber. For convenience we set the CO_2 partial pressure in the membrane to equal that of the anode, though if internal membrane behavior is of interest, this could be replaced with a diffusional model for CO_2. Importantly, as described below a diffusional model is applied to the membrane for the supporting electrolyte and cupric species.

Further, the following additional assumptions are made in this model development

- For the parallel geometry no axial heat transfer occurs along the copper plate
- For the series geometry axial and transverse heat transfer occurs along the copper plate
- No thermal heat loss occurs in the flash tank

Governing Equations

Conservation equations discussed below govern the transport of species, charge, and heat within an EMAR unit cell. These governing equations are divided into two regimes: the channels, which are open and through which convection may occur, and the membrane, which is porous and through with convection does not occur. In total six partial differential equations will be established for each regime. These correspond to four chemical species (amine + amine bound to CO_2, amine bound to copper, cationic supporting electrolyte, and anionic supporting electrolyte), charge, and heat. Species conservation equations in concert with charge conservation establishes an electroneutrality condition, thus electroneutrality and species and charge conservation are linearly dependent.[39] Therefore, for simplicity the cationic supporting electrolyte governing equation will be replaced with an algebraic electroneutrality condition in each of the regimes.

Anodic and Cathodic Channel Governing Equations

For some chemical species i, with the exception of the supporting cation as discussed above, in the anodic or cathodic channels diffusive, migrative, and convective mass transport terms govern its conservation as given in equation 4.4. No generation term exists as it is assumed that all reaction is heterogeneous taking place at an electrode boundary, rather than homogeneously in the bulk. Electroneutrality is also imposed in the bulk as given in equation 4.5, ignoring double layer formation.

$$\nabla \cdot (-D_{i,}\nabla c_i - z_i u_{m,i} F c_i \nabla \phi_l) + \mathbf{u} \cdot \nabla c_i = 0 \tag{4.4}$$

$$\sum z_i c_i = 0 \tag{4.5}$$

Similarly, charge conservation is subjected to diffusive and migrative transport terms. The convective charge transport term, $\mathbf{u}\sum_i z_i c_i$, is neglected as a consequence of electroneutrality. Again no generation term exists. Charge conservation may be also thought of as current continuity. Therefore, equation 4.6 is expressed a current continuity equation as well as charge conservation.

$$\nabla \cdot \mathbf{i}_l = \nabla \cdot \left(F \sum_i z_i \left(-D_i \nabla c_i - z_i u_{m,i} F c_i \nabla \phi_l \right) \right) = 0 \tag{4.6}$$

The Einstein relation describes mobility as a function of diffusivity as given below.[40]

$$u_{m,i} = \frac{z_i}{RT} D_i$$

Unlike species and charge conservation, the governing equation for heat conservation for this system includes a generation term in addition to diffusion and convection. This generation term is a consequence of Joule heating.[41]

$$k_l \nabla^2 T + \rho_l C_{p,l} \mathbf{u} \cdot \nabla T = \mathbf{i}_l \cdot \nabla \phi_l \tag{4.7}$$

In order to minimize model computational cost a parabolic flow profile from channel inlet to channel outlet is imposed, eliminating the need to solve the Navier-Stokes equation. The flow profile, given by equations 4.8 and 4.9, assumes a no slip condition at vertical channel boundaries.

$$u_{anode} = \frac{6\bar{u}}{H_{ch}} x \left(1 - \frac{x}{H_{ch}}\right) \tag{4.8}$$

$$u_{cathode} = \frac{6\bar{u}}{H_{ch}} \left(x - (H_{ch} + H_m)\right) \left(1 - \frac{x - (H_{ch} + H_m)}{H_{ch}}\right) \tag{4.9}$$

$$\bar{u} = \frac{Q}{W \cdot H_{ch}}$$

Membrane Separator Governing Equations

This model assumes a stagnant, porous membrane. As a result, the governing equation for species, charge, and heat established for the anodic and cathodic channels above must be modified by removing the convective terms and correcting for the diffusivity, thermal diffusivity, and mobility in a porous matrix.

The Bruggeman relationship, given below, describes the effective diffusion coefficient of species i in a porous matrix, with a porosity ε.[42] As before the effective diffusion coefficient is related to the effective mobility through the Einstein relation. The thermal diffusivity is related in the same manner.

$$D_{i,eff} = \varepsilon^{3/2} D_i$$

In this regime, electroneutrality still holds. The modified governing equations for species, charge, and heat conservation are given in equations 4.10, 4.11, and 4.12 respectively.

$$\nabla \cdot (-D_{i,eff} \nabla c_i - z_i u_{m,i,eff} F c_i \nabla \phi_l) = 0 \tag{4.10}$$

$$\nabla \cdot \mathbf{i}_l = \nabla \cdot \left(F \sum_i z_i \left(-D_{i,eff} \nabla c_i - z_i u_{m,i,eff} F c_i \nabla \phi_l \right) \right) = 0 \tag{4.11}$$

$$k_{eff} \nabla^2 T = \mathbf{i}_l \cdot \nabla \phi_l \tag{4.12}$$

Boundary Conditions

Inflow Boundary Conditions

Standard Dirichlet boundary conditions are applied to the anodic and cathodic channel entrances with respect to species concentration and temperature. Anodic inlet concentration and temperatures are set as inputs to the model as given below.

$$c_i|_{anode\, inlet} = c_i \left(0 < x < H_{ch}, y = 0\right) = c_{in}$$

$$T|_{anode\, inlet} = T \left(0 < x < H_{ch}, y = 0\right) = T_{in}$$

Cathodic inlet conditions are set to the average of the anodic outlet conditions. This assumes no thermal loss in the flash. As stated previously, we assume flow in the cathodic chamber maintains a constant effective CO_2 loading, which may be calculated from average anodic outlet conditions using equation 3.3 from the previous chapter.

$$\begin{aligned} c_i|_{cathode\,inlet} &= c_i\left(H_{ch} + H_m < x < 2H_{ch} + H_m, y = 0\right) \\ &= \begin{cases} \text{ave}\left(c_i|_{anode\,outlet}\right) = \text{ave}\left(c_i\left(0 < x < H_{ch}, y = L\right)\right) & i \neq \mathrm{CO_2} \\ 0 & i = \mathrm{CO_2} \end{cases} \end{aligned}$$

$$\begin{aligned} T|_{cathode\,inlet} &= T\left(H_{ch} + H_m < x < 2H_{ch} + H_m, y = 0\right) \\ &= \text{ave}\left(T|_{anode\,outlet}\right) = \text{ave}\left(T\left(0 < x < H_{ch}, y = L\right)\right) \end{aligned}$$

The membrane boundary at the inlet is assumed to be impermeable and adiabatic as given below.

$$\mathbf{n} \cdot \left(D_i \nabla c_i\left(H_{ch} < x < H_{ch} + H_m, y = 0\right)\right) = 0$$

$$\mathbf{n} \cdot \left(k \nabla T\left(H_{ch} < x < H_{ch} + H_m, y = 0\right)\right) = 0$$

These boundaries are considered electronically insulating, that is, there is no current across them.

$$\mathbf{n} \cdot \mathbf{i}_l|_{inlet} = \mathbf{n} \cdot \mathbf{i}_l\,(x, y = 0) = 0$$

Outflow Boundary Conditions

Standard Neumann boundary conditions are applied to the anodic and cathodic channel exits as well as the membrane boundary near those exist. Namely, the heat and species diffusive fluxes are set to 0. As before these boundaries are considered electronically insulating, that is, there is no current across them.

$$\mathbf{n} \cdot (D_i \nabla c_i\,(x, y = L)) = 0$$

$$\mathbf{n} \cdot (k \nabla T\,(x, y = L)) = 0$$

$$\mathbf{n} \cdot \mathbf{i}_l\,(x, y = L) = 0$$

Anodic and Cathodic Boundary Conditions

There are 3 separate boundary conditions applied to the anode and cathode boundaries. These include those for concentration, charge (current), and heat. All three of these are coupled, as faradaic reactions involve both current and species and generate (or remove) heat. The rate of faradaic reactions, and therefore, the boundary conditions for concentration and charge are given by the Butler-Volmer equation, provided in Equation 4.13.

$$i_{loc} = i_0 \left[\exp\left(\frac{(1-\alpha)\, nF}{RT} \eta \right) - \exp\left(\frac{-\alpha nF}{RT} \eta \right) \right] \tag{4.13}$$

$$\eta = \phi_s - \phi_l - \phi_{eq}$$

$$\mathbf{n} \cdot \mathbf{i}_l = i_{loc}$$

$$\mathbf{n} \cdot \mathbf{N}_i = \frac{\nu_i i_{loc}}{nF}$$

There is a heat of reaction for both the anodic and cathodic reactions. As stated previously, the cathodic reaction is much more endothermic than the anodic reaction. In addition, there is Joule heating associated with the overpotential at each electrode. The series geometry employs a period boundary condition, which results in heat transfer between electrodes. This heat transfer is approximated assuming the copper plate is a very good conductor. The parallel geometry on the other hand has a symmetric boundary condition and therefore has no heat transfer between electrodes. The boundary conditions for the parallel and series geometry for the anode and cathode are given in Equations 4.14 and 4.15 respectively.

$$\mathbf{n}\cdot(k\nabla T) = (\phi_s - \phi_l - \phi_{eq})\, i_{loc} - \frac{i_{loc}}{F}\left(\Delta H_{CO_2} + H_{f,Cu-Am}\right) + \begin{cases} \frac{k_{Cu}}{H_{Cu}/2}\left(T_{Cu} - T\right) & \text{series} \\ 0 & \text{parallel} \end{cases} \tag{4.14}$$

$$\mathbf{n}\cdot(k\nabla T) = (\phi_s - \phi_l - \phi_{eq})\, i_{loc} + \frac{i_{loc}}{F}\left(H_{f,Cu-Am}\right) + \begin{cases} \frac{k_{Cu}}{H_{Cu}/2}\left(T_{Cu} - T\right) & \text{series} \\ 0 & \text{parallel} \end{cases} \tag{4.15}$$

Where T_{Cu} is the average copper temperature (average of anode and cathode skin temperatures), k_{Cu} is the heat transfer coefficient for copper, and H_{Cu} is the thickness of the copper.

Butler-Volmer Parameters

The exchange current density, i_0, and the electron transfer coefficient, α, are based off of Stern's work.[1] The exchange current density is scaled as shown in Equation 4.16, to account for different concentrations and temperatures at the boundary.

$$i_o \propto (1 - x_{Cu})^{1/2} (x_{Cu})^{3/4} \exp\left(-\frac{E_a}{RT}\right) \tag{4.16}$$

The equilibrium potential for an EMAR solution was solved for in the previous chapter, see equation 3.13. This equilibrium potential is a function of CO_2 partial pressure which as been assumed to be a constant $P_{CO_2,anode}$ for cathode and may be calculated using equation 3.4 from the previous chapter for the cathode. This is under the assumption that effective CO_2 loading does not change along the cathodic path. Equation 4.17 give this equilibrium potential.

$$\phi = \phi^\circ + \frac{RT}{2F}\left[\ln\left(x_{cu}\right) + \ln\left(\frac{m\tilde{A}m_0}{2}\right) - \ln\left(1 + \beta\left[\frac{\tilde{A}m_0\left(1 - x_{Cu}\right)}{1 + K_{CO_2}\tilde{P}^m_{CO_2}}\right]^{2/m}\right)\right] \quad (4.17)$$

Remixing Turns

The geometry shown in Figure 4-4 is, of course, a simplification of the actual geometry of an EMAR cell, which is detailed in Chapter 5. In reality the anodic and cathodic paths are baffled, creating a slightly more tortuous path. It has been assumed in the past that the presence of baffles creates remixing regions for the fluid.[2] In actuality the Reynolds number for fluid in an EMAR cell is quite low, between 1 and 20, securely in the laminar flow regime and nearly in the stokes regime. With inertial forces playing such a minor role, the remixing seen in other, more turbulent, regimes is not seen in the EMAR process.

This is made clear by a CDF model which tracks the fluid velocity and resulting streamlines within an EMAR cell. Figure 4-5 shows the result of applying the Navier-Stokes equation to the series geometry seen in Chapter 5, which demonstrates no remixing.

The baffles in an EMAR cell then serve only to prevent channeling and and provide structure to the membrane separating the anodic and cathodic channels. Therefore,

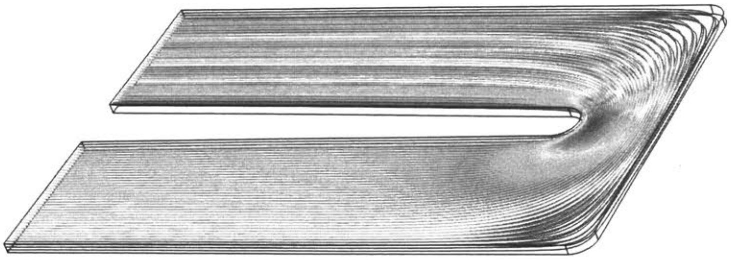

Figure 4-5: Streamlines of fluid passing along an EMAR baffle show no remixing.

no intermediate mixing has been assumed for the EMAR process, despite the presence of baffling.

Solver Method

A finite element approach is employed in the Comsol Multiphysics computing platform. Free-triangular meshing for the regions shown in Figure 4-4, where the y-dimesion has been scaled to account for the large channel length to depth ratio, is assigned. A typical meshing strategy is shown in Figure 4-6, however it is modified as needed when geometrical changes, i.e. path length, are made.

Parameters Used

Table 4.1 gives the parameters used for the model described above. These parameters were meant to reflect the dimensions of EMAR 8.x described in Chapter 5 for all values other than the total length.

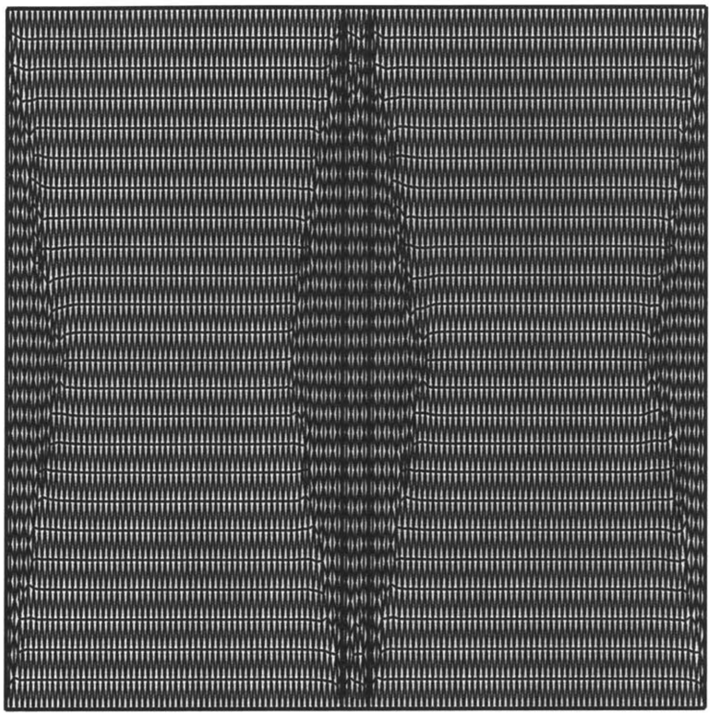

Figure 4-6: Free tiangular meshing scheme employed by model.

Symbol	Name	Value	Reference
$c_{Am,in}$	Inlet amine concentration	$1\ M$	
$c_{NaNO_3,in}$	Inlet supporting electrolyte concentration	$1\ M$	
D_i	Diffusivity coefficient for all species, i	$1 \times 10^{-9}\ m^2 \cdot s^{-1}$	
E_a	Activation energy for electrochemical reaction	$50.7\ kJ \cdot mol^{-1}$	
F	Faraday's constant	$96,485.33\ C \cdot mol^{-1}$	
H_{ch}	Channel thickness	$0.0625\ in$	
H_m	Membrane thickness	$0.005\ in$	
ΔH_{CO_2}	Heat of reaction CO_2-Amine	$-85\ kJ \cdot mol^{-1}$	38
$H_{f,Cu-Am}$	Heat of formation Cu-amine per amine	$20\ kcal \cdot mol^{-1}$	43
i_0	Exchange current density at $x_{Cu} = 0.5$ and $T = 328.16\,K$	$1.45\ A \cdot m^{-2}$	
K_{CO_2}	Amine binding affinity	500	1
$\tilde{k}_{H,CO_2}$	Dimensionless Henry's Law coefficient	0.05	36
L_{ch}	Channel length	$2\ m$*	
Q	Volumetric flow rate	$10\ ml \cdot min^{-1}$	
T_{in}	Inlet temperature	$318.15\ K$	
ΔV_{cell}	Cell voltage	$1.0\ V$*	
W	Channel Width	$0.484\ in$	
$x_{Cu,in}$	Inlet copper loading	0.4	
α	Electron transfer coefficient	0.31	1
ε_m	Membrane void fraction	0.5	
ϕ°	Reference potential	$0.337\ V$	

Table 4.1: Parameters used for EMAR transport model, with references where appropriate. *These inputs may vary as noted in the results below.

Model Results

A summary of results from the model provided above is discussed below. Just as the governing equations are organized by species conservation, charge conservation, and heat conservation, so too are the profiles presented below. Of the three, the temperature profile is most susceptible to system geometry. This results from the fact that the electrode boundary condition either insulates or transmits heat from one electrode to the other, for the parallel and series geometries respectively. The same cannot be said for either mass or charge as there is neither mass flux between electrodes or ionic current (though electric current drives the electrochemical reaction). Still species and voltage profiles are slightly impacted by geometry in that the electrochemical kinetics are dependent on temperature, which is in turn geometry dependent.

Therefore the more simple species and voltage profiles are discussed first, followed by the temperature profiles. Further experimental results are provided to help validate the model.

Species Concentration

As stated previously, species concentration profile only slightly depends on system geometry. The results below are presented for the series geometry, but are similarly a reflection of the parallel configuration. As expected, anodic boundary layers are seen for copper-amine complex formation and amine-CO_2 complex depletion. Correspondingly, cathodic boundary layers exist for free amine generation and copper-amine complex consumption. Supporting electrolyte concentrations show the same

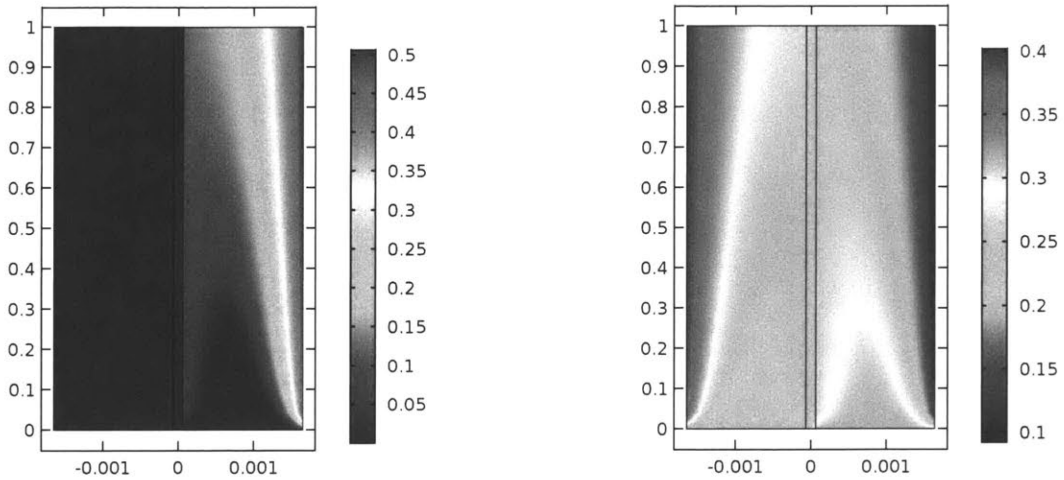

(a) Amine Concentration, $mol \cdot L^{-1}$ (b) Amine-Cu Concentration, $mol \cdot L^{-1}$

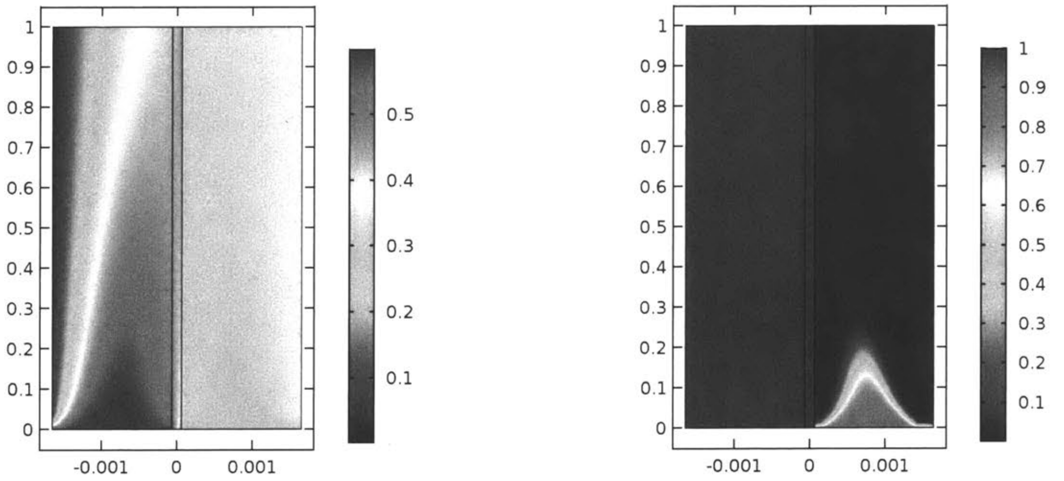

(c) Amine-CO_2 Concentration, $mol \cdot L^{-1}$ (d) CO_2 Partial Pressure, Bar

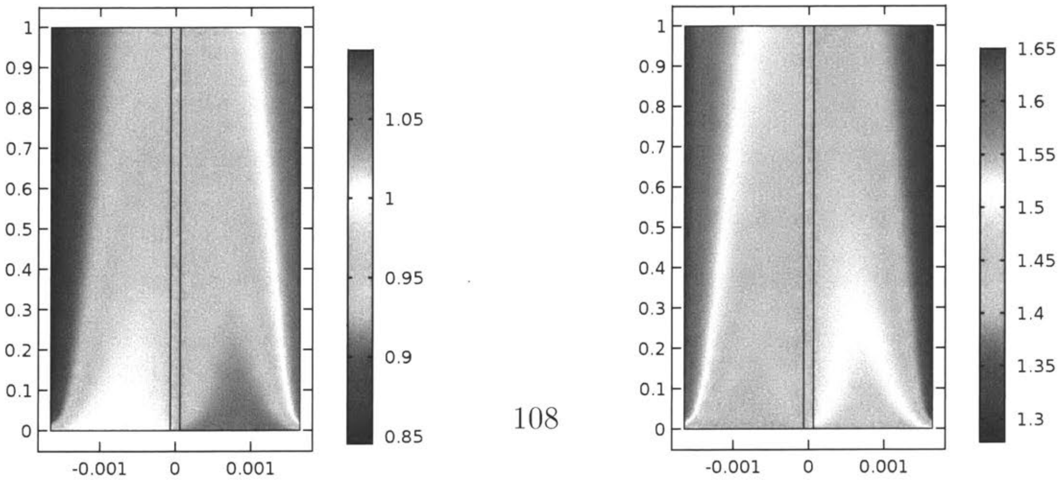

(e) Na^{2+} Concentration, $mol \cdot L^{-1}$ (f) NO_3^- Concentration, $mol \cdot L^{-1}$

Figure 4-7: Concentration profile of all species tracked within an EMAR unit cell, , with anodic electrode on left and cathodic electrode on right.

boundary layer formation. Similar to that seen in the thermodynamic cycle, the cathodic path shows an initially high CO_2 partial pressure which rapidly decreases with decreasing state of charge.

Species conservation governing equations and charge conservation equations are linearly dependent as discussed previously. Therefore, from the results provided in Figure 4-7 we can determine the voltage profile in an EMAR cell. Figure 4-8 shows the electrolyte profile which results from a $\Delta V_{cell} = 1\,V$ simulation where the cathode is set to 0 V. As discussed previously, cell voltage can contribute to thermodynamic, kinetic, or transport overpotential - ohmic losses for this model are lumped into transport overpotentials, and bubble overpotential are ignored - as given below.

$$\Delta V_{cell} = \Delta E_{eq} + \eta_{RXN} + \eta_{trans}$$

As Figure 4-8 shows that the transport overpotential, which is the additional voltage required to drive species through a boundary layer or through the bulk (ohmic overpotential), is very small. The difference between maximum and minimum electrolyte potential is $0.17\,V$, a small fraction of the overall $1.0\,V$. Equilibrium overpotential is discussed in Chapter 3 and is small as well. As a result kinetic overpotentials, η_{RXN}, dominate and may be improved by increased electrode surface area.

As seen in Figure 4-9 anodic and cathodic current densities mirror each other and decrease in absolute value as they move away from the inlet.

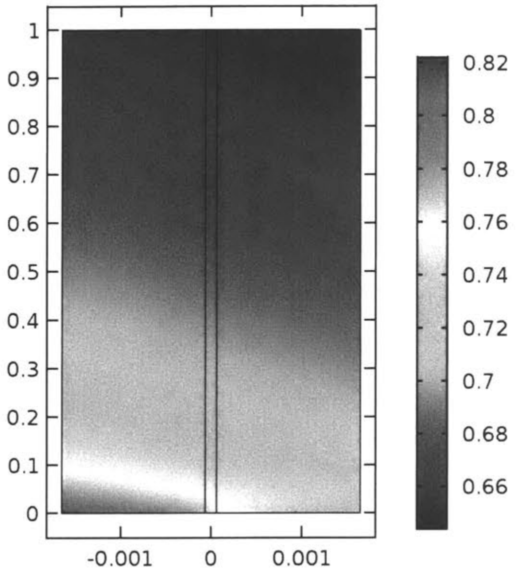

Figure 4-8: Electrolyte potential in an EMAR unit cell, with anodic electrode on left and cathodic electrode on right.

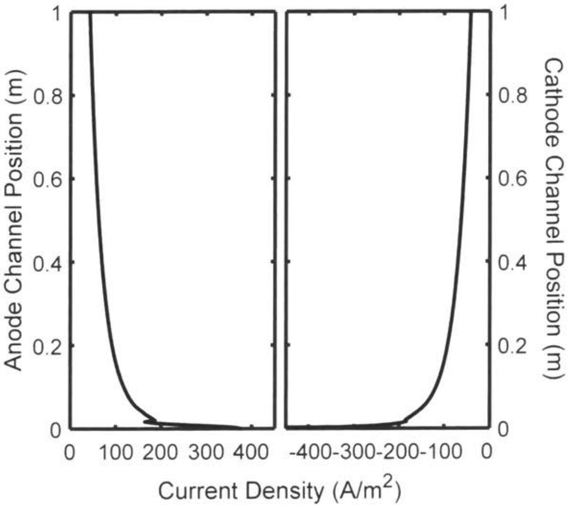

Figure 4-9: Electrode current densities in an EMAR unit cell.

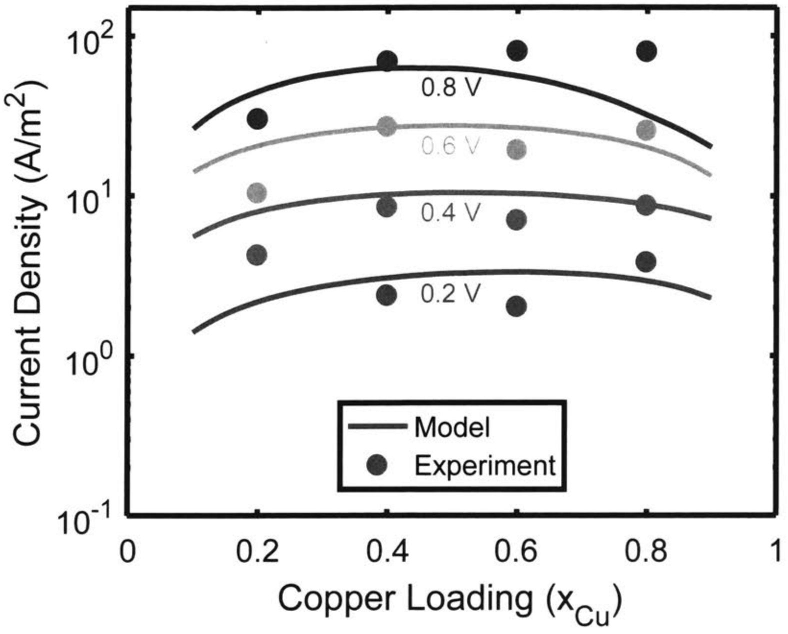

Figure 4-10: Effect of inlet copper loading and voltage on current density in an EMAR cell, as predicted by the transport model and seen experimentally.

Experimental Comparison

Executing this model for a variety of unit cell potentials and inlet copper loadings, under conditions similar to that seen in the EMAR 8.2 apparatus discussed in Chapter 5, reveals additional system behavior and allows for model validation. Figure 4-10 shows the model prediction for unit cell current density at a variety of potentials for a span of copper loading conditions, along with the experimentally measured results. The model and experiment show qualitative agreement and indicate a preference for operation at moderate anodic inlet copper loadings.

The deviation between the model and the experiments seen at high copper loadings and high potentials may be caused by one of several issues.

- At high voltages adverse side reactions, especially cathodic side reactions, may consume faradaic efficiency and inflate current density. This particular experiment was run using a sodium nitrate supporting electrolyte which may undergo the following side reaction.

  $$\mathrm{NO_3{}^-(aq) + H_2O + 2\,e^- \rightleftharpoons NO_2{}^-(aq) + 2\,OH^-(aq)}$$
  $$\mathrm{Cu^{2+}(aq) + OH^-(aq) \rightleftharpoons Cu(OH)_2(s) \rightleftharpoons CuO(s) + H_2O}$$

  Further credence is given to this mechanism when one looks at Figure 5-14 from Chapter 5, which shows a cathodic electrode which has formed a copper oxide layer
- At high copper loadings, EMAR fluid has very low CO_2 capacity which may have been desorbed by as much as 5% during the course of a high copper loading experiment. The result would be a decreased CO_2 partial pressure and a significant decrease in anodic open circuit potential, driving up the current density, but decreasing the faradaic efficiency.
- At high voltages with large CO_2 degassing rates it is possible that the anodic boundary layer is disrupted by bubble induced advection, decreasing the transport overpotential. The result would be an increase in current density, without a change in faradaic efficiency.

Figure 4-11 shows the effect that this inlet copper loading has on anodic and cathodic overpotentials. As Stern predicts, cathodic overpotentials dominate at all but very high copper loadings.[1]

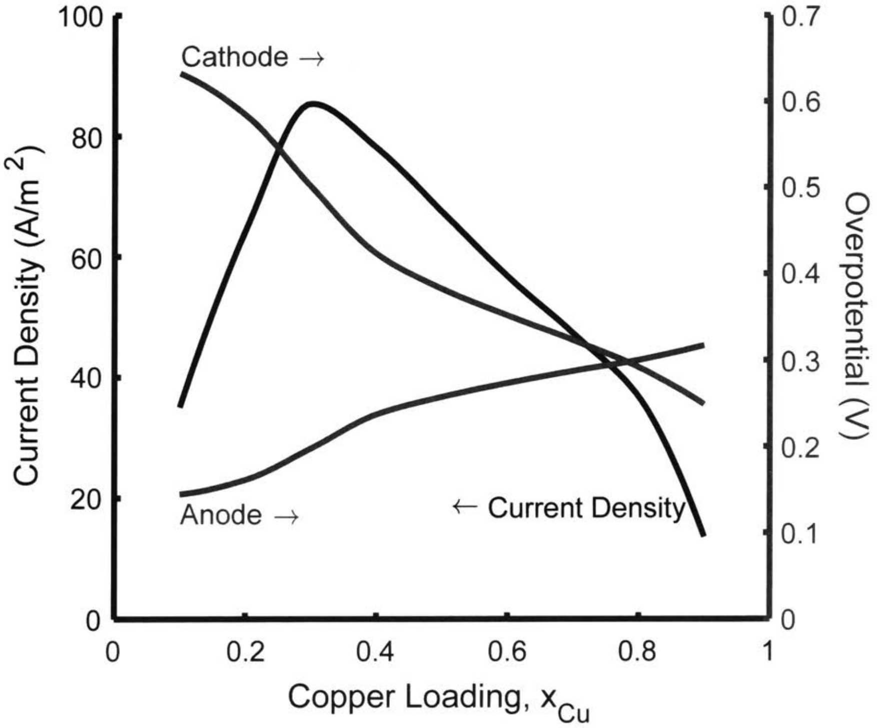

Figure 4-11: Effect of inlet copper loading current density and anodic and cathodic overpotential

Temperature

Unlike the species and voltage profiles, the temperature profiles are highly dependent system geometry. For the parallel geometry, differing anodic and cathodic kinetic overpotentials as well as current distributions result in varied cooling due to heat of reaction or Joule heating at boundaries. In this geometry no heat transfer occurs between electrodes and it is assumed no axial heat transfer occurs along the copper plate. In this sense, the parallel geometry represent the most severe possible conditions for temperature gradients. Conversely, the series geometry which has a periodic boundary condition and allows for both axial and transverse heat is the least sever condition. This is reflected in the temperature profiles shown in Figure 4-12.

As discussed previously the overall temperature change seen in flow through the desorber is given by

$$\Delta T_{cell} = \frac{Am_0 \left(-\Delta H_{CO_2} + F\Delta V_{cell}\right) \Delta x_{Cu}}{c_p}$$

For most cell voltages, ΔT_{cell} is negative and thus the stream cools as in Figures 4-12a and 4-12b. However, if $\Delta V_{cell} > \Delta H_{CO_2}/F$, which for the case of EDA is $\Delta V_{cell} > 0.88\,V$, a stream entering the desorber will increase in temperature. The model predicts this behavior as seen in Figures 4-12c and 4-12d.

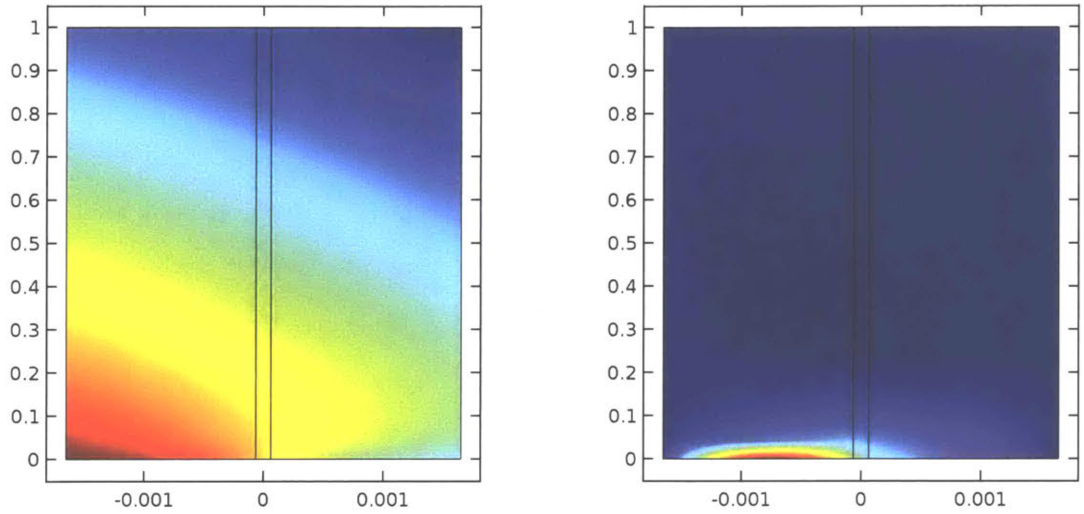

(a) Parallel Geometry, Cell Voltage = 0.5 V

(b) Series Geometry, Cell Voltage = 0.5 V

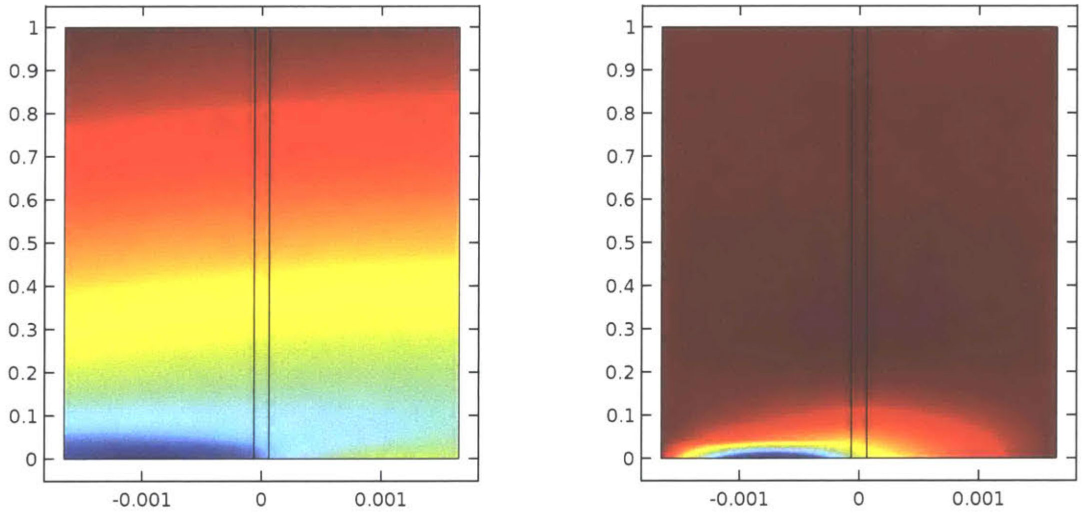

(c) Parallel Geometry, Cell Voltage = 1.0 V

(d) Series Geometry, Cell Voltage = 1.0 V

Figure 4-12: Temperature distribution profiles (red indicating hot, blue indicating cold) show a more severe temperature distribution within an EMAR unit cell for the parallel geometry as compared to the more homogeneous series geometry at both moderate (0.5 V) and high (1.0 V) operation. The three regions shown in each figure from left to right are: anodic channel, membrane, cathodic channel.

Summary and Conclusions

Chapter 3 established the thermodynamic minimum work of separation for an EMAR cycle. This chapter expanded on that work by considering the transport phenomena encountered in an EMAR unit cell. Particular emphasis was placed on heat conservation, as EMAR kinetics, especially cathodic reaction kinetics, where shown by Stern to be particularly temperature sensitive. An endothermic desorption combined with a system that behaves nearly adiabatically - a result of scale up - presents the opportunity temperature excursion zones within an EMAR cell. This is mitigated slightly by Joule heating, a function of cell voltage, with will serve to reheat the system.

A transport model was built which considered two possible EMAR stack geometries, parallel and series shown in Figures 4-2 and 4-3. Of the two, parallel represented the most severe possible conditions for temperature gradients as a symmetric boundary condition precluded heat transfer between electrodes and no axial heat transfer was assumed along the copper plate. On the other hand, the series geometry represented the least severe temperature gradient condition as axial and transverse heat transfer occurred through the copper electrodes.

In addition to heat conservation, the transport model tracked current and four species concentrations, namely the copper-amine complex, non-copper bound amine, supporting anion electrolyte, and supporting cation electrolyte. Further, species concentration of CO_2 bound amine and free amine was inferred using equations 4.2 and 4.3 in conjunction with amine-CO_2 binding affinity, K_{CO_2}, and CO_2 partial pressure, P_{CO_2}. Boundary conditions were established which reflected an EMAR unit cell and heat transfer conditions described above. Of note, anodic and cathodic boundary conditions were established using the kinetics investigated by Stern.[1]

The result was a model which showed the formation of anodic and cathodic boundary layers and indicated the dominate overpotential was kinetically driven. This leads to the conclusion that EMAR cells may be improved in the future by increasing electrode surface area, since transport resistances represented only a minor overpotential loss. As expected the parallel geometry shows more extreme temperature gradients than the series geometry. Further, at a moderate cell voltage of 0.5 V the desorption stream cooled while passing through the EMAR cell, while at a high voltage of 1.0 V the desorption stream slightly increased in pressure.

Chapter 5 will detail the EMAR stack design and control scheme for which this model was built. It will also provide a brief history of past EMAR cell designs as well as suggestions for future work which should consider the results from this transport model.

THIS PAGE INTENTIONALLY LEFT BLANK

Chapter 5

Cell and System Design for the EMAR Process

The previous chapters have established the thermodynamic and transport behavior of the EMAR process. This chapter will detail previous efforts made to produce a working proof of concept EMAR device as well as current efforts to scale up and make more robust the EMAR desorber and the process flow scheme which supports the desorber.

First, the process flow scheme within which an EMAR cell operates will be introduced. Specifically the control scheme, which sets flows to the EMAR desorber and controls auxiliaries, as well as the system's process automation, which facilitates experimental work for the EMAR process, will be dissected.

This chapter will then shift focus to the EMAR desorber itself. The anatomy of an EMAR cell will provide the context through which two types of designs will be discussed: single cell and stacked systems. Single cell systems were previously constructed by first Stern, followed by Mystic River Engineering under the guidance of Eltayeb. A brief history of these single cell systems is provided. The bulk of this chapter is dedicated to the design, construction, and testing of stacked EMAR systems, whose geometry was introduced in Chapter 4.

Specifically, two stacked geometries will be discussed: parallel and series. The parallel configuration requires low voltage, high current operation, whereas the series configuration allows for high voltage, low current operation. The internals of EMAR stacks based on these two geometries are discussed. A brief introduction will be made to a system which employs an absorber which may scale to match the desorption capacity of the EMAR desorber stack.

Finally, this chapter will provide experimental results based on the two EMAR stack geometries. These experiments will serve to verify the efficacy of the model developed in Chapter 4, use test the EMAR stack design, and explore the behavior of the EMAR process on a larger scale. A brief description of an EMAR experiment will be provided as well.

EMAR Process Flow Scheme and Process Automation

An EMAR process requires at minimum an EMAR cell, a flash tank, an absorber, and pumps to transport fluid between these units. The design and function of the electrochemical cell are provided in detail below. Therefore, this section will describe

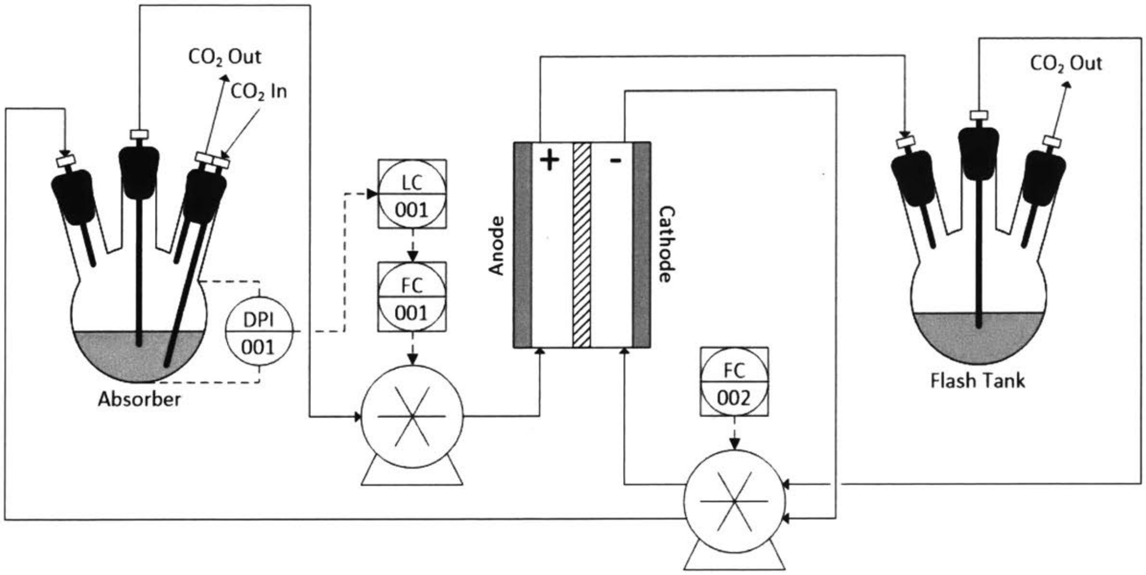

Figure 5-1: Process flow diagram for EMAR experimental apparatus.

the auxiliary components required to operate an EMAR process as well as that process's automation. Figure 5-1 gives the current, at the time of this writing, process flow diagram for the EMAR process. The absorber, which consist of a three neck flask fitted with gas and liquid ports, receives an amine flow from the cathodic outlet of the EMAR cell. In the absorber, amines freed by the cathode, are contacted by carbon dioxide and bound. Excess CO_2 is vented off while CO_2 loaded amines are sent to the anodic channel of an EMAR cell. After CO_2 release in the anode, the gas liquid mixture is disengaged in the flash tank, which like the absorber is a three neck flask. Liquid leaving the flash tank is feed to the cathode, refreshing amines for capture, before returning the stream to the absorber.

Flows are controlled by two peristaltic pumps: FC001 and FC0002. FC001 is a single head pump whose flow is manipulated by a level controller on the absorber. Level in the absorber is determined via a standard bubbler configuration, by measuring the

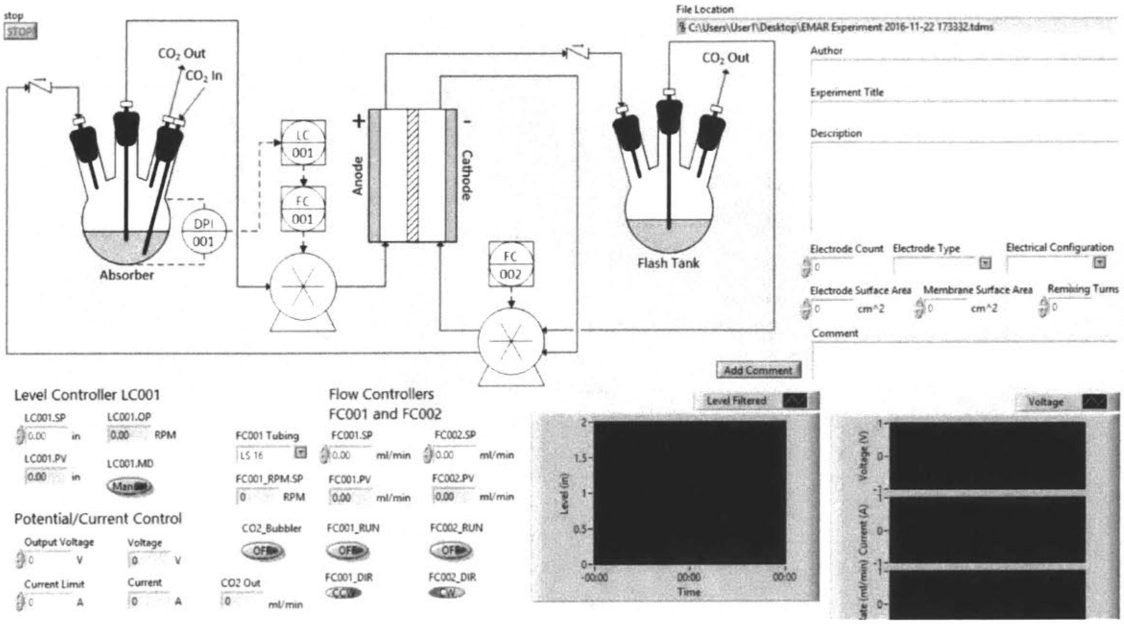

File Location
C:\Users\User1\Desktop\EMAR Experiment 2016-11-22 173332.tdms

Author

Experiment Title

Description

Electrode Count 0
Electrode Type
Electrical Configuration
Electrode Surface Area 0 cm^2
Membrane Surface Area 0 cm^2
Remixing Turns 0
Comment

Level Controller LC001
LC001.SP 0.00 in
LC001.OP 0.00 RPM
LC001.PV 0.00 in
LC001.MD Manual

Potential/Current Control
Output Voltage 0 V
Voltage 0 V
Current Limit 0 A
Current 0 A

Flow Controllers FC001 and FC002
FC001 Tubing LS 16
FC001.SP 0.00 ml/min
FC002.SP 0.00 ml/min
FC001_RPM.SP 0 RPM
FC001.PV 0.00 ml/min
FC002.PV 0.00 ml/min
CO2_Bubbler OFF
FC001_RUN OFF
FC002_RUN OFF
CO2 Out 0 ml/min
FC001_DIR CCW
FC002_DIR CW

Figure 5-2: A screen shot of the EMAR process control and automation system built in LabVIEW.

pressure difference between inlet CO_2, which enters at the bottom of the flask, and outlet CO_2. The detuned level controller, LC001, serves to maintain a mass balance in the system without requiring excess flow rate excursion in FC001 in response to system disturbances or calibration differences between FC001 and FC002. FC002 is a two headed pump which controls both cathodic inlet and cathodic outlet flows. As both of these flows are liquid this two headed configuration ensures equal inlet and outlet flows in the cathode, i.e. no bulk liquid crossover from the separator. With three of the four EMAR cell streams controlled all degrees of freedom are satisfied, and anodic outlet stream which is a gas-liquid mixture remains uncontrolled.

The whole EMAR process is controlled, automated, and recorded within LabVIEW. A screen shot of this governing program is given in Figure 5-2. A National Instruments DAQ as well as a number of serial ports are used to monitor and control all

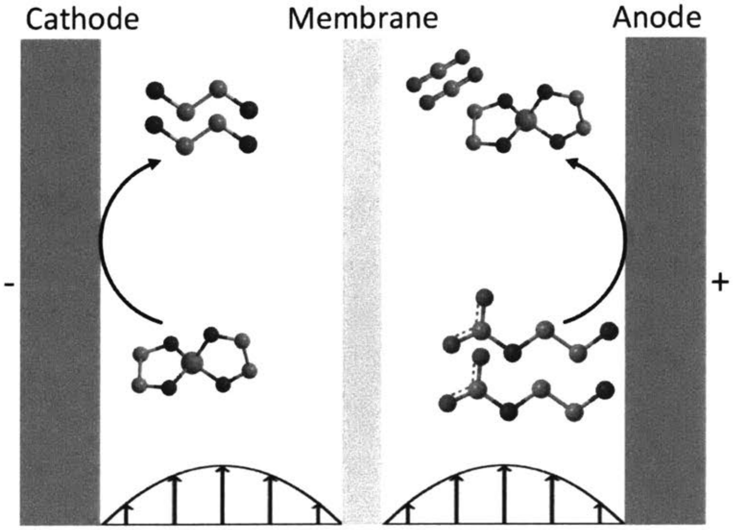

Figure 5-3: An EMAR unit cell consist of (from right to left) an anode, an anodic channel, a membrane, a cathodic channel, and a cathode.

of the components see in Figure 5-1, which include: pump direction, run status, and flow rate, differential pressure level indication, gas flow status and rate, applied potential, and applied current. The LabVIEW program acquires and automatically stores process data and controls all fields shown in white on Figure 5-1. Further, the system is fully automated, allowing for experimental recipes to be loaded and executed. A second phase of this design will allow for automated cell polarity and anodic/cathodic flow switching, to be used during long time frame cycleability experiments.

Anatomy of an EMAR Cell

An EMAR unit cell, shown in Figure 5-3, consists of 5 regions.

Anode A copper electrode where a positive potential is applied, oxidizing copper and driving the release of CO_2.

Anodic Channel A channel through which EMAR fluid from the absorber flows and is exposed to the anodic desorption before being sent to a flash tank for CO_2 removal.

Membrane A separator which serves to disrupt the transfer of CO_2 released at the anode to the cathode where it could otherwise be reabsorbed.

Cathodic Channel A channel through which EMAR fluid from the flash tank flows and is exposed to the cathodic amine regeneration before returning to the absorber for CO_2 capture.

Cathode A copper electrode where a negative potential is applied, reducing the copper-amine complex and regenerating amines for capture.

Initial EMAR designs by Stern and Eltayeb, discussed below, employed a single unit cell geometry and therefore had only one of each of the five regions. However, scale up of electrochemical systems requires a shift from a single unit cell geometry to a stacked cell geometry like that given in Figure 5-8. As will be discussed below stacked electrochemical systems may be operated in a series configuration, which requires high voltage but low current, or in a parallel configuration, which requires a high current but low voltage.

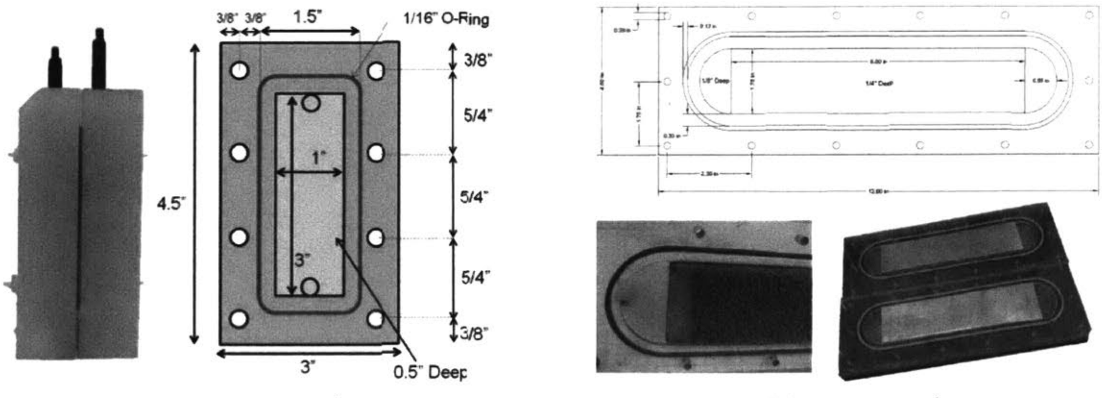

(a) EMAR 2.0[1]

(b) EMAR 3.0[1]

Figure 5-4: EMAR 2.0 and EMAR 3.0 we designed by Stern. This figure is reproduced from Stern's PhD thesis[1]

Single Cell EMAR Designs

The first proof of concept EMAR design, which was a single unit cell system, was reported by Stern et al. in 2013.[27,44] That reported design was EMAR 4. What follows is brief history of single cell EMAR designs, beginning with Stern's original work. Other systems discussed in this section are those designed under the management of Eltayeb and Shaw (author).[2]

EMAR 2 and EMAR 3

EMAR 2 consisted of two polypropylene support structures, which were both chemically inert and electrically insulating. These support structures contained 0.5 inch channel cuts which each housed a typically porous electrode. Support structures with a membrane separator where bolted together and sealed via a racetrack o-ring. As seen in Figure 5-4a inlet flows entered from a port in the bottom of the polypropylene support and exited from the top, ensuring a liquid full channel. EMAR 2 suffered primary by way of its large channel depth, which resulted in high ohmic resistances upon operation. Further, the relatively small electrode size, as compared to the systems that will be discussed below, minimized the copper loading shift possible for this system.[1]

EMAR 3 employed a similar geometry to EMAR 2, replacing the polypropylene supports with the slightly less chemically stable but easier to machine polycarbonate. The channel depth was significantly decreased, while the channel surface area was significantly increased. EMAR 3 allowed for both flat plate and porous electrode operation. This design however suffered from leaking primarily from the port, not seen in Figure 5-4b, which provided current to the electrodes.[1] This issue would be solved in EMAR 6 which would utilize a modified compression fitting to seal a current collecting stem. Both EMAR 2 and EMAR 3 employed a Nafion membrane which would be replaced with porous polypropylene or filter paper in future generations.

EMAR 4 and EMAR 5

EMAR 4 and EMAR 5 represented a significant design shift for the EMAR process. Instead of utilizing a support structure which doubled as a flow channel, EMAR 4, seen in Figure 5-5a, employed an aluminum chassis which acted also as a current collector for the electrodes. For EMAR 4, two flat copper plates are laid in electrical contact with two aluminum chassis. Two silicon or Teflon gaskets with a porous polypropylene membrane in between separated the two electrodes and created the anodic and cathodic flow paths. The aluminum supports were then bolted together utilizing insulating washers and bolt covers, thereby preventing a short between the

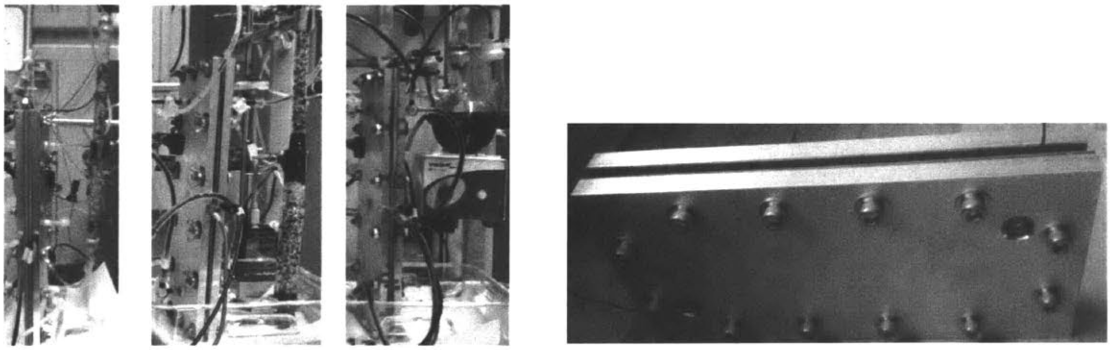

(a) EMAR 4.0[1]

(b) EMAR 5.0[2]

Figure 5-5: EMAR 4.0 was designed by Stern and EMAR 5.0 was designed by Mystic River Engineering under Eltayeb management. This figure is reproduced from Stern's PhD thesis and Eltayeb's PhD thesis.[1,2]

two current collectors. As before, flows entered from the bottom and exited from the top. This geometry, while not as simple to seal as the racetrack o-ring geometry offered a few key advantages over EMAR 3. Namely the silicon or Teflon gaskets could be cut into different shapes thereby allowing for different channel thicknesses and flow fields, both of which were fixed in EMAR 3. Further this more robust design did not suffer from the current collector leaking that EMAR 3 experienced.[1]

Still, EMAR 4 was not without its downsides. Lack of membrane support resulted in flow field disruptions as the membrane collapsed towards one electrode or the other. This was corrected using an inert filler which provided nucleation sites for dendrite growth. Further the electrical connection was poor and required frequent manipulation and the liquid ports leaked at times.[2]

EMAR 5, designed by engineering consulting firm Mystic River Engineering under Eltayeb's management and seen in Figure 5-5b, improved on EMAR 4's design by introducing a more robust, leak free geometry. No longer was the aluminum chassis used as a current collector. Instead it was electrically insulated from the copper plate electrodes using a silicon rubber backing. Current was brought to the electrodes via a brazed copper wire connection, which removed the need for solder. The customized gasket/flow channels separated by a porous polypropylene membrane remained and allowed for design flexibility. The gasketed flow channel design employed by this and the previous EMAR generation, had a significant flaw in that the comprehensibility of the channel meant that channel with was strongly a function of torque ratio. This design was utilized for the bulk of Eltayeb's work.[2]

EMAR 6

EMAR 6, also designed by Mystic River Engineering under Eltayeb's management, represented another significant shift in EMAR cell design. As seen in Figure 5-6, EMAR 6 employed multiple electrically insulated electrodes exposed to both the anodic and cathodic channels. It kept the gasket/flow channel design, but entirely changed the method of supplying current to the cell. Current was provided via posts which passed through an insulating support layer - which itself held the electrodes in place and insulated - and through a modified compression fitting which provided the seal. This current collector configuration would be used heavily in subsequent EMAR designs. Again, an aluminum chassis provided structural support, while allowing for access to the current supply posts as well as to compression fittings used for liquid flow.

By independently supplying current to each of four electrode pairs, this novel design allowed for discretized, axial resolution for the current density at each electrode. This allowed the user to more precisely determine the effect of channel depth and flow field

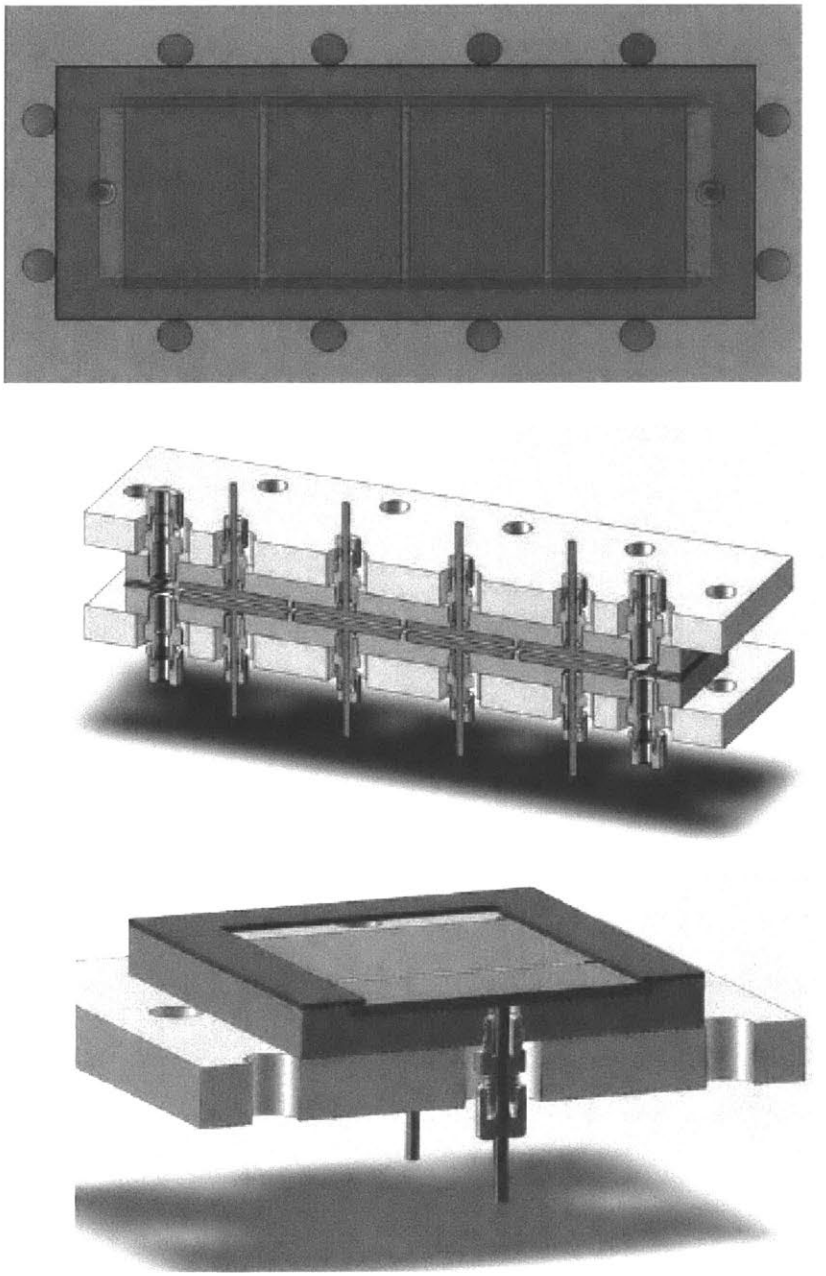

Figure 5-6: EMAR 6.0 was designed by Mystic River Engineering under Eltayeb management. It incorporated multiple insulated electrodes which allowed for axial current density resolution. This figure is reproduced from Eltayeb's PhD thesis[2]

on faradaic current. Still, EMAR 6 was not without it's flaws. It's modular flexibility resulted in a difficult to assemble system and the gasket/channel flow architecture was prone to leaks as it had been in the previous designs. Further, the compressibility of the flow channel remained a source of significant variability in this EMAR stack, as it had for EMAR 4 and 5. For this reason, all future EMAR designs would employ a racetrack o-ring system seen in EMAR 2 and EMAR 3.

EMAR 7

EMAR 7, designed by Mystic River Engineering under Shaw's (author) management, was the first, and to date the only, EMAR cell designed to operate a high EMAR desorption pressures - up to 12 bar. As shown in Figure 5-7, this design employed two polyether ether ketone (PEEK) support structures each with interlocking racetrack o-rings. As in EMAR 3, a flat plate electrode was inserted into a channel cut into the support structures and secured using inert PEEK screws. A replaceable silicone electrode backing allowed for manipulation of the channel depth. As in the EMAR 6 system, current was carried to the electrodes via a post sealed using a modified compression fitting.

The compact design of EMAR 7 allowed for this system to be applied to novel electrochemical systems, where only small liquid quantities were available, for example ionic liquid based systems. Further, the small flow channel width minimized channeling. The system's small size however made it unfeasible for use on scaled-up EMAR processes which will be discussed below.

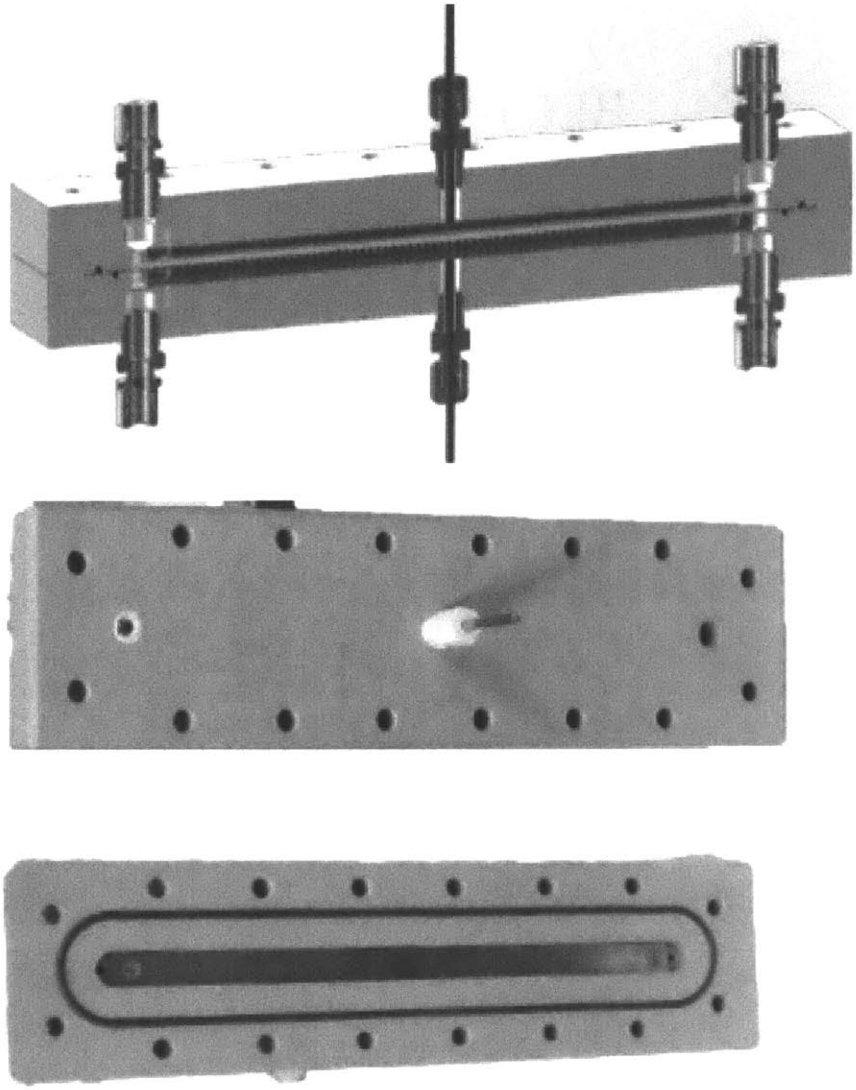

Figure 5-7: EMAR 7.0 was designed by Mystic River Engineering under Shaw's (author's) management. It allowed for high pressure EMAR experimentation. This figure is reproduced from Eltayeb's PhD thesis[2]

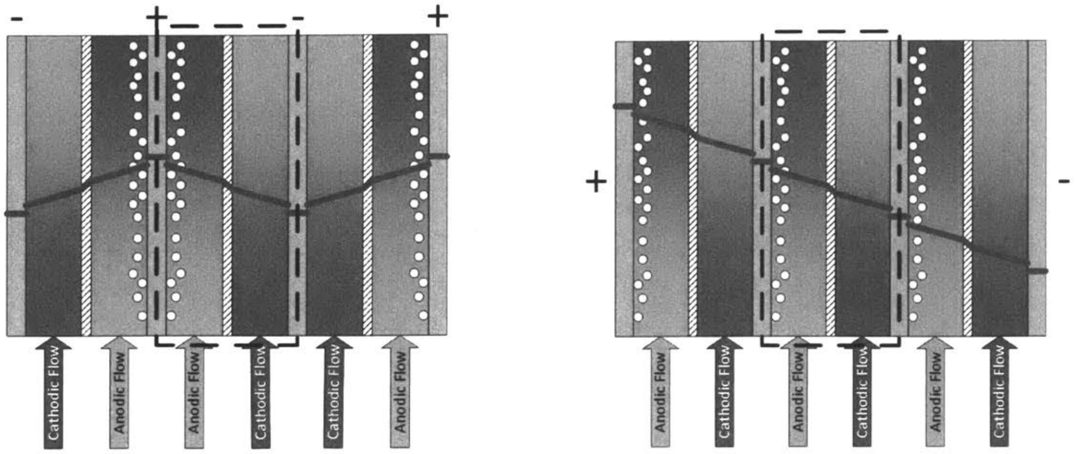

(a) Parallel Configuration

(b) Series Configuration

Figure 5-8: EMAR stack configurations arranged parallel and series, with voltage profile shown in maroon and unit cell boxed in center.

Stacked EMAR Designs

In order to scale up the EMAR process, EMAR designs starting with EMAR 8.x transitioned from a single unit cell to a stack geometry. As discussed previously, the EMAR process may be arranged in an electrochemical stack in two different configurations: parallel and series. Figure 5-8 shows the configuration and voltage profile for each of these geometries. A parallel configuration alternates voltage between consecutive mono-polar copper plates. Each plate then acts as either an anode or cathode, with the same anodic or cathodic flow on either side. A series configuration on the other hand cascades voltage from one side of the stack to another, with each copper plate acting as a bipolar plate. Each plate in the series geometry then acts as an anode on one side and a cathode on the other.

Notice, each geometry has the same unit cell. Consider a stack of n unit cells, in which a single unit cell with cell voltage V_{cell} draws a current of i_{cell}. As seen in Figure 5-8a, in the parallel configuration the stack will require a voltage of V_{cell} and a current of nI_{cell}. The series configuration, shown in Figure 5-8b, on the other hand will require a voltage of nV_{cell} and a current of I_{cell}. While the parallel stack operates at a low voltage and the series at a low current, they both operate at the same total power, $nV_{cell}I_{cell}$.

With this in mind, EMAR 8.x was designed as a stack to operate in either parallel or series configurations. The manifold structure described below directs flows and currents as prescribed by Figure 5-8.

EMAR 8.x

The EMAR 8.x stack in either configuration is consists of alternating copper plates and membrane separators, which may be either porous polypropylene or filter paper. The copper plates are placed in polycarbonate channel supports, which strategically manifold flow appropriately to cathodic and anodic flow channels. Copper plates have polypropylene baffles attached with adhesive which as discussed in Chapter 4 provide support to the membrane separator and prevent channeling. The resulting active surface area for electrochemical reaction per electrode face is approximately 70 cm^2, approximately matching that for the previous EMAR designs.

EMAR 8.1 is a parallel configuration. As seen in Figure 5-8a, for the parallel configuration anodic flows must be sent to both sides of an anode - similarly for a cathode and cathodic flows. The support plate show in Figure 5-9a accomplishes that task. Consider an anodic flow entering the bottom left of that support plate, while ca-

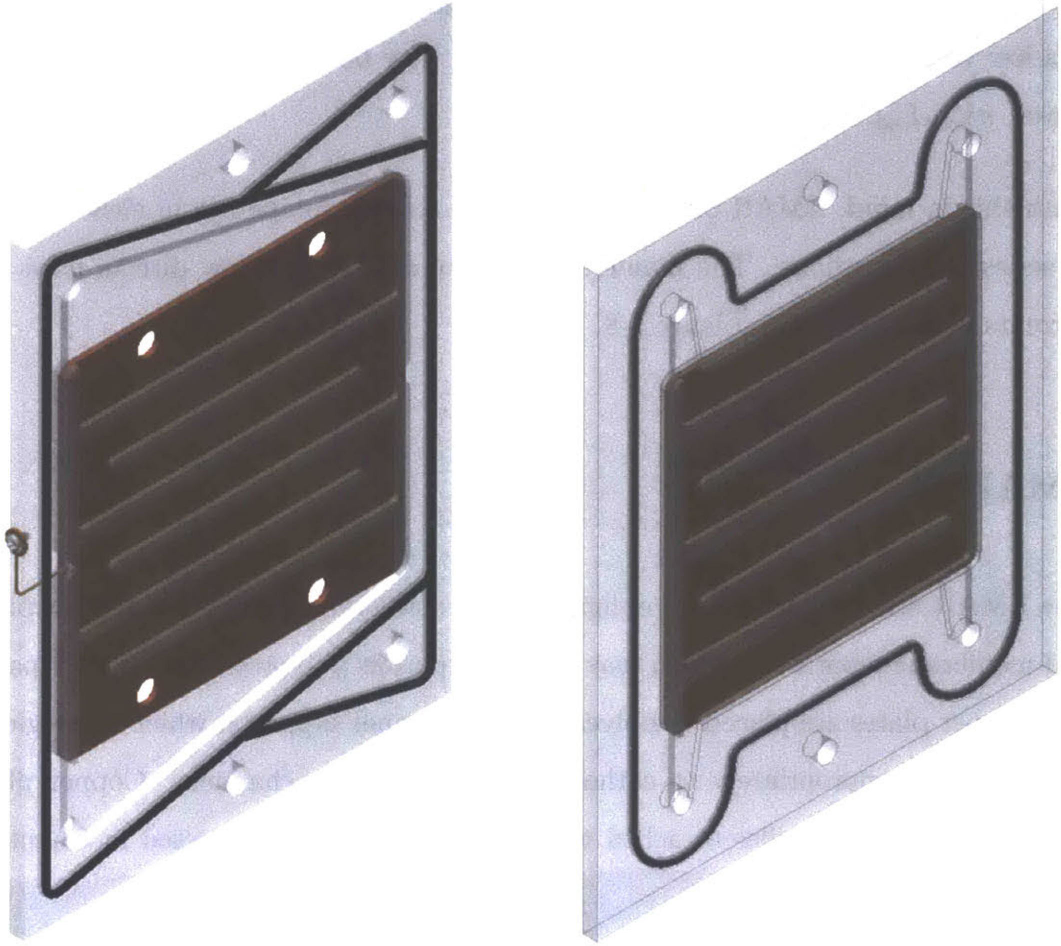

(a) EMAR 8.1 Parallel Plate (b) EMAR 8.2 Series Plate

Figure 5-9: EMAR 8.x can be run in as a stack either series or parallel configuration. Plates strategically manifold flows such that anodic streams are exposed to anodes and cathodic streams are exposed to cathodes.

thodic flows enter the bottom right. Anodic flows would be exposed to both sides of the electrode while following up to the exit on the top left. Cathodic flows one the other hand will bypass the anode entering a cathode - rotated 180 degrees from that shown in Figure 5-9a. In this configuration, current is supplied via a side port.

EMAR 8.2 on the other hand is a series configuration. As seen in Figure 5-8b, for the series configuration anodic flows must be sent to one side of a bi-polar plate while cathodic flows are sent to the other. The support plate show in Figure 5-9b accomplishes that task. Consider an anodic flow entering the bottom left of that support plate. That anodic flow would be exposed to the front facing side of the electrode before exiting from the top left. Similarly a cathodic flow entering the bottom right this support plate would be exposed the the rear facing side of the electrode seen in Figure 5-9b. Unlike the parallel configuration no current need be supplied except at the end plates which employ a modified geometry.

Appendix A provides engineering drawings for EMAR 8.1 and 8.2 support plates, copper plates, end plate, baffles, and support structure.

Figure 5-10 shows how the support plates shown in Figure 5-9 may be manifolded in to an EMAR stack. This manifold bears similarity to a flat plate heat exchanger in that one stream , without loss of generality the anodic stream, enters the bottom left of the stack and is exposed to all anodes before leaving from the top left, similarly for the cathodic flows and the right. The result is a compact system which appropriately segregates anodic and cathodic flows and provides far more electrode surface are than previous designs with a simple scale-up method.

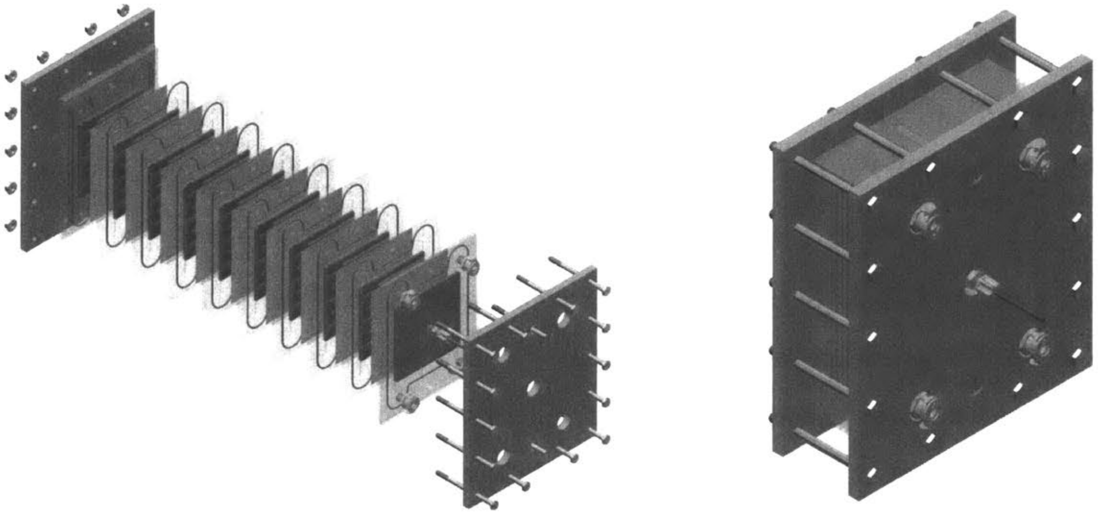

(a) EMAR 8.x Stack Exploded View (b) EMAR 8.x Stack

Figure 5-10: An EMAR 8.x stack consists of alternating electrode plates and membranes strategically manifolded in a geometry similar to that of a flat plate heat exchanger. It may be easily scaled up by adding additional electrodes to the stack.

EMAR 9

EMAR 8.x outperforms the three neck flask used as an absorber and shown in Figure 5-1. That is, the electrochemical desorber desorbs significantly more CO_2 than the absorber may uptake. Therefore EMAR 9, rather that redesigning the desorber, incorporates a sub-pilot scale absorber as shown in Figure 5-11.

EMAR Experimental Work

EMAR 8.x discussed above has been the focus of experimental work used to verify the efficacy of the model developed in Chapter 4, use test the design, and explore

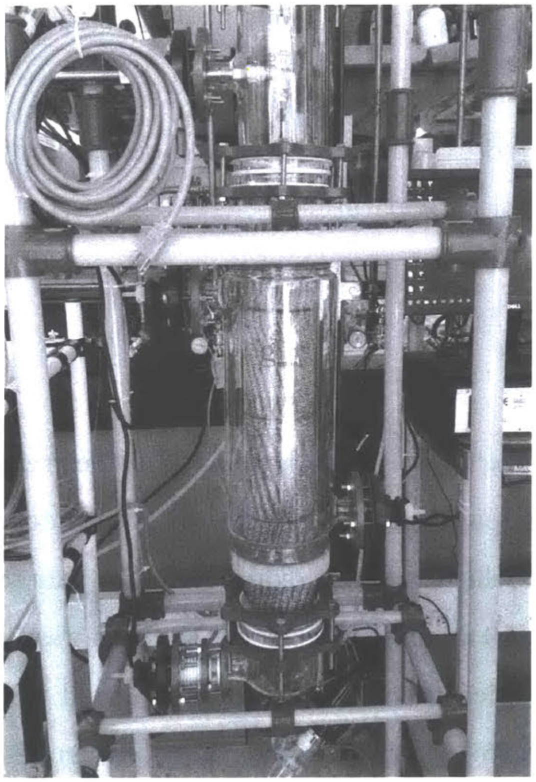

Figure 5-11: Absorber for EMAR 9.0

the behavior of the EMAR process on a larger scale. Below is a description of the typical experimental methods used in testing EMAR 8.x as well as a summary of the results seen from this experimental work, some of which is introduced in other chapters as well.

Experimental Method

In preparing for an EMAR experiment, care must be taken in electrode preparation, stack assembly, and solution preparation.

Electrode Preparation

Prior to assembly in a stack, electrodes have their baffles removed and are polished with a medium grit sandpaper to a bright finish. Electrodes are then exposed to a 0.1 M nitric acid bath, which removes oxides or other contaminants from previous experiments, for at least 10 minutes. Electrodes are then washed with deionized water before being promptly dried with a paper towel to avoid oxidation. Polypropylene baffles are then adhered to both sides of the copper electrodes in the manner seen in Figure 5-12 using super glue or a similar adhesive. Electrodes with baffles are then placed in polycarbonate channel supports and an o-ring is added to the support's racetrack. In the parallel configuration, copper wires which supply the current are connected to the copper plate and the channel supports by two set screws seen in Figure 5-9a. End plate electrodes are prepared in nearly the same manner except baffles are placed on only one side and a current providing rod is connected to the opposite side of the baffles. See Appendix A for more details.

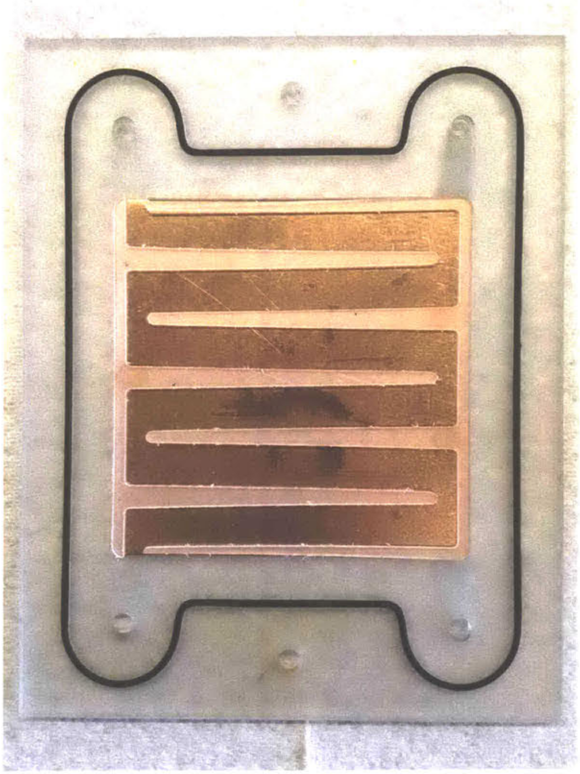

Figure 5-12: EMAR 8.2 electrode with baffles and support plate.

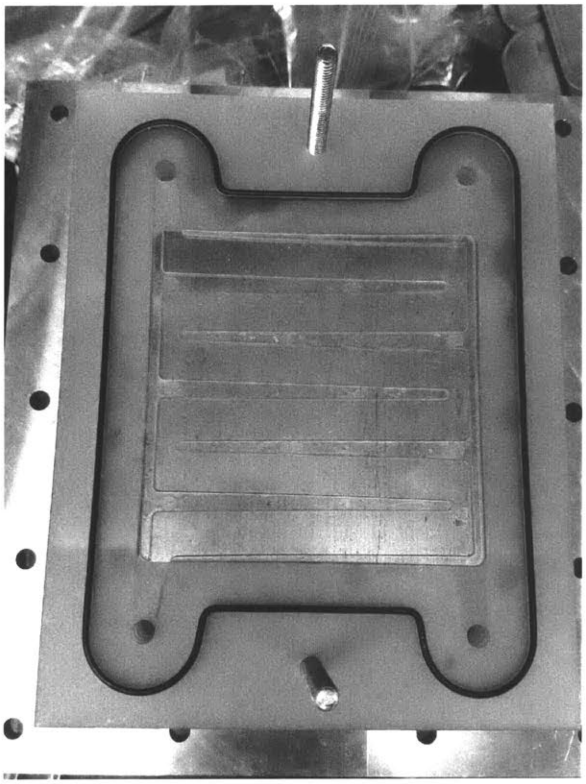

Figure 5-13: EMAR 8.2 stack being assembled along guide bolts.

Stack Assembly

The stack is assembled via a layer-by-layer method in which polycarbonate channel supports are stacked one on top of the other with a separator in between. Guide bolts - the flat head machine screws in Figures 5-10a and 5-13, are used to ensure all stacks line up appropriately. The separator may be one or more sheets of either porous polypropylene or filter paper. The 14 bolts on the periphery of the EMAR stack in Figure 5-10b are tightened to a torque of 10 lb.in per unit cell. Therefore if a stack consists of five unit cells - four bipolar electrodes and two end plates - each of the 14 bolts is tightened to a torque of 50 lb.in.

Species	Concentration
Ethylenediamine	$1 - 2\ M$
Copper Nitrate	$0.1 - 0.8\ M$
Sodium Nitrate	$1 - 2\ M$

Table 5.1: Typical EMAR solution concentrations. Notice, one cupric ion binds 2 EDA molecules so 0.2 M copper nitrate in a 1 M EDA solution corresponds to 40% loading.

Solution Preparation

An EMAR solution consists of water, amine (typically EDA), copper salt, and supporting electrolyte. Generally the copper salt is picked to compliment the supporting electrolyte. For example cupric nitrate would be used if the supporting electrolyte chosen was sodium nitrate. Table 5.1 shows typical EMAR solution compositions.

After the solution has been prepared, it is saturated with carbon dioxide by bubbling until the pH reaches near neutral. In the event that the feed gas to the absorber is a mixture rather than pure CO_2, the EMAR solution should be pre-saturated with the same mixture rather than pure CO_2 - this will influence the final pH.

EMAR Operation

With the EMAR solution pre-saturated, the absorber is filled an flows are started. Figure 5-14 shows EMAR 8.2 in operation, with the absorber and FC001 on the right and the flash and FC002 on the left. The control scheme discussed previously allows for a variety of experiments to be run including modification of voltage, current, and flow rates all in an automated fashion. Yet to be automated for this system is the polarization and flow channel switch that must occur to maintain a copper balance

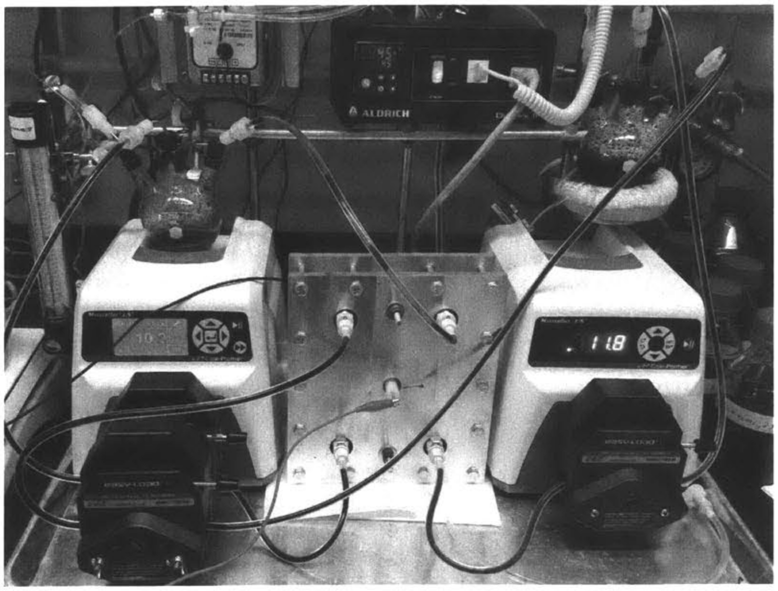

Figure 5-14: EMAR apparatus showing absorber and anodic flows on the right and cathodic flows and flash tank on left.

during long term operation. This switch may be easily done manually as the quick disconnects which provide flows to the stack come with automatic shut off upon disconnect.

Post Experiment Tear Down

After an experiment is completed the system is drained, water washed, and drained again before taking apart the stack. The cathode seen in Figure 5-15 is frequently seen to have a uniform oxide layer formation upon tear down. This is most common after experiments utilizing sodium nitrate supporting electrolyte. The following reaction mechanism is proposed to explain the oxide formation.

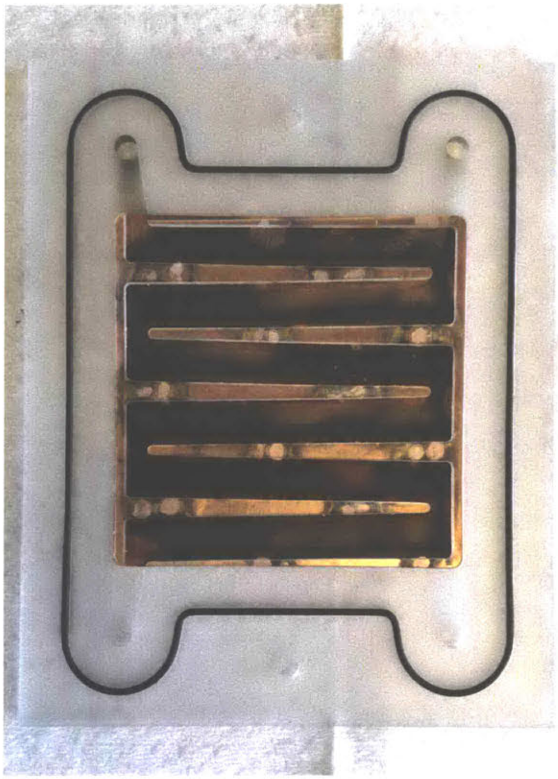

Figure 5-15: EMAR 8.2 electrode showing an oxide layer after operation.

$$\mathrm{NO_3^-(aq) + H_2O + 2\,e^- \rightleftharpoons NO_2^-(aq) + 2\,OH^-(aq)}$$
$$\mathrm{Cu^{2+}(aq) + OH^-(aq) \rightleftharpoons Cu(OH)_2(s) \rightleftharpoons CuO(s) + H_2O}$$

In these cases the electrode is sanded and cleaned with nitric acid in the manner discussed in the electrode preparation step.

Experimental Results

Detailed below is a summary of experimental results seen by EMAR 8.x. These results serve to validate the transport model discussed in Chapter 4 as well as expand our knowledge of the EMAR process and validate the design and construction of the EMAR 8.x experimental stack. Experimental work focuses primarily on EMAR 8.2, the series stack, as series is not only easier to assemble, but more industrially relevant. Still, data showing the efficacy of EMAR 8.1, the parallel stack, is provided.

Copper Loading Effect

In order to validate the model detailed in Chapter 4 a suite of copper loading experiments were completed. The EMAR solutions seen in Table 5.2 where produced and saturated with 1 Bar CO_2.

After saturation, a polarization experiment was completed for each of the solutions. At a flow rate of 10 ml/min using a 5 unit cell stack in series EMAR unit cell voltage was increased in steps from 0.2 volts per unit cell (1.0 V total) to 0.8 volts per unit cell (4.0 V total). Each of these steps were allowed to proceed to steady state and the

Species	Concentration
Ethylenediamine	1 *M*
Copper Nitrate	0.1, 0.2, 0.3, 0.4 *M*
Sodium Nitrate	1 *M*

Table 5.2: Solutions used for copper loading experiment. Notice, one cupric ion binds 2 EDA molecules so 0.1 *M* copper nitrate corresponds to 20% loading.

current was measured. Figure 5-16 gives the resulting current density as a function of unit cell voltage and copper loading.

This experiment shows, as the model predicts, that the EMAR process under these conditions is kinetically limited. This is seen by noting the nearly exponential increase in current density as voltage increases linearly. If we were in a transport limited regime a limiting current density would have been seen a high voltages, this was not the case. Instead, exponential Butler-Volmer kinetics dictated the current density of the stack.

Still, the model and experiment do not entirely agree. The model predicts a preference for moderate inlet copper loading which was not seen experimentally. Reasons for this dependency are discussed in detail in Chapter 4.

Supporting Electrolyte Effect

In order to better understand the effect electrolytes have on the EMAR process, two EMAR solutions, seen in Table 5.3, were produced.

As before, the chloride based and nitrate based solutions we saturated with 1 Bar CO_2 and a polarization experiment was completed for each of the solutions. At a flow rate of 10 ml/min using a 5 unit cell stack in series EMAR unit cell voltage was

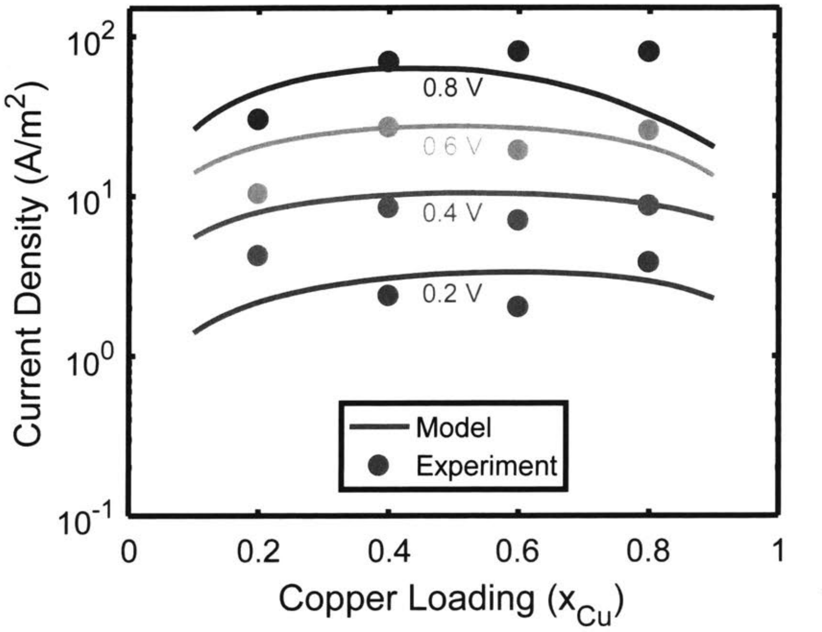

Figure 5-16: Effect of inlet copper loading and voltage on current density in an EMAR cell, as predicted by the transport model and seen experimentally.

Species	Concentration	Species	Concentration
Ethylenediamine	1 M	Ethylenediamine	1 M
Copper Nitrate	0.2 M	Copper Chloride	0.2 M
Sodium Nitrate	1 M	Sodium Chloride	1 M

Table 5.3: Solutions used for supporting electrolyte experiment.

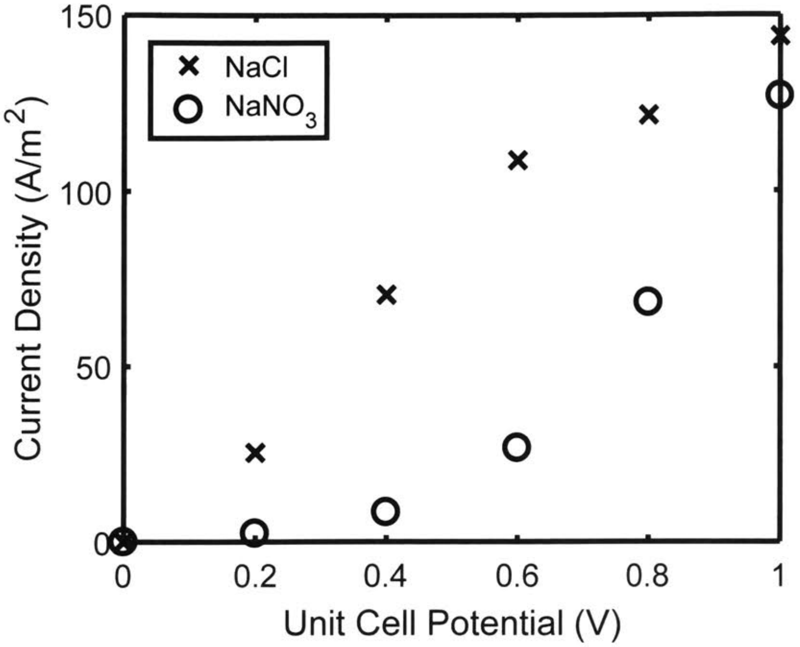

Figure 5-17: Effect of two supporting electrolytes, sodium chloride and sodium nitrate, on EMAR stack current density.

increased in steps from 0.2 volts per unit cell (1.0 V total) to 1.0 volts per unit cell (5.0 V total). As before, the system was allowed to reach steady state at each step. Figure 5-17 gives the resulting polarization curve for both the nitrate and chloride solutions.

Whereas the nitrate solution shows a kinetically limited polarization profile, the chloride solution indicates a transport limitation. This can be seen in the exponential relationship current density and unit cell potential for the nitrate solution and a limiting current density for the chloride system. Stern first noted the kinetic enhancement of chloride supported systems.[1]

The increased kinetics are not without their downsides however. Faradaic efficiency

Species	Concentration
Ethylenediamine	1 M
Copper Nitrate	0.2 M
Sodium Nitrate	1 M

Table 5.4: Solutions used for reversibility experiment.

for the chloride system was 50% lower than that of the nitrate system - down from 50% to 25%. Further, metallic copper particles were seen leaving the anodic chamber. This is likely a function of chloride stabilization of cuprous ions.[45] The following adverse side reaction is proposed.

$$\mathrm{Cu(s)} \rightleftharpoons \mathrm{Cu^{+}(aq)} + \mathrm{e^{-}}$$
$$2\,\mathrm{Cu^{+}(aq)} \rightleftharpoons \mathrm{Cu^{2+}(aq)} + \mathrm{Cu(s)}$$

It is worth noting, that as discussed previously, the nitrate system has its own adverse side reaction which results in the oxide seen in Figure 5-15. The EMAR process remains in need of a supporting electrolyte with the enhanced kinetics of the the chloride system, the faradaic efficiency of the nitrate system, and which minimizes adverse side reactions.

Reversibility

As discussed in Chapter 3, the EMAR process transports the copper blocker from the anode to the cathode. Therefore, upon anode depletion the process must be reversed, switching anodic and cathodic flows as well as applied potential. To that end, a reversibility study was completed for the EMAR 8.2 stack. An EMAR solution, given in Table 5.4, was prepared and saturated with 1 Bar CO_2.

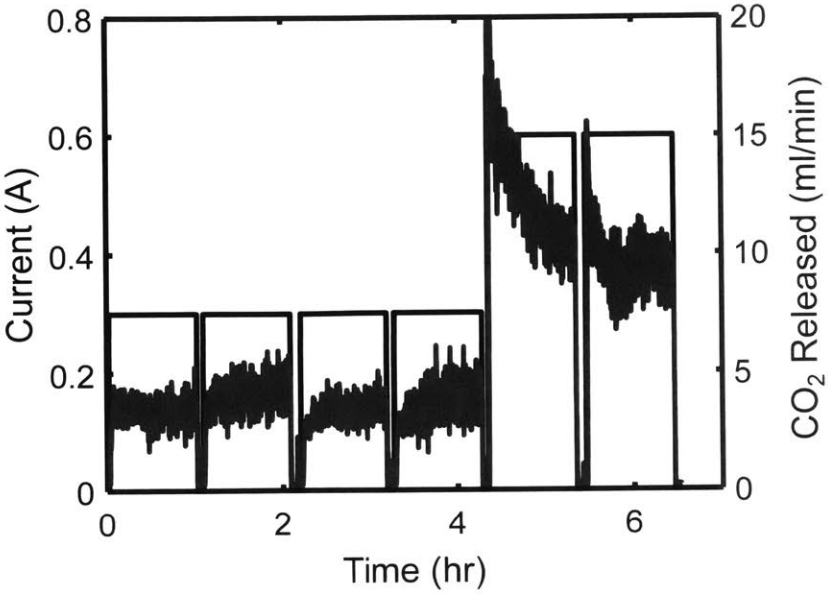

Figure 5-18: Reversibility of EMAR stack, shows fairly consistent faradaic efficiency over time.

The EMAR process was set to operate a series of one hour constant current experiments. After each hour, the anodic and cathodic flows were switched as was the polarization. As shown in Figure 5-18, the EMAR process showed no faradaic efficiency loss over multiple cycles.

Superficial Velocity Effect

The previously described experimental work has focused on the easier to assemble and more industrially relevant EMAR 8.2 series stack. The following experimental approach, however, tests the efficacy of the EMAR 8.1 parallel stack. The EMAR solution given in Table 5.5 was produced and saturated. In the same manner as the

Species	Concentration
Ethylenediamine	1 M
Copper Nitrate	0.25 M
Sodium Nitrate	1 M

Table 5.5: Solutions used for superficial velocity experiment.

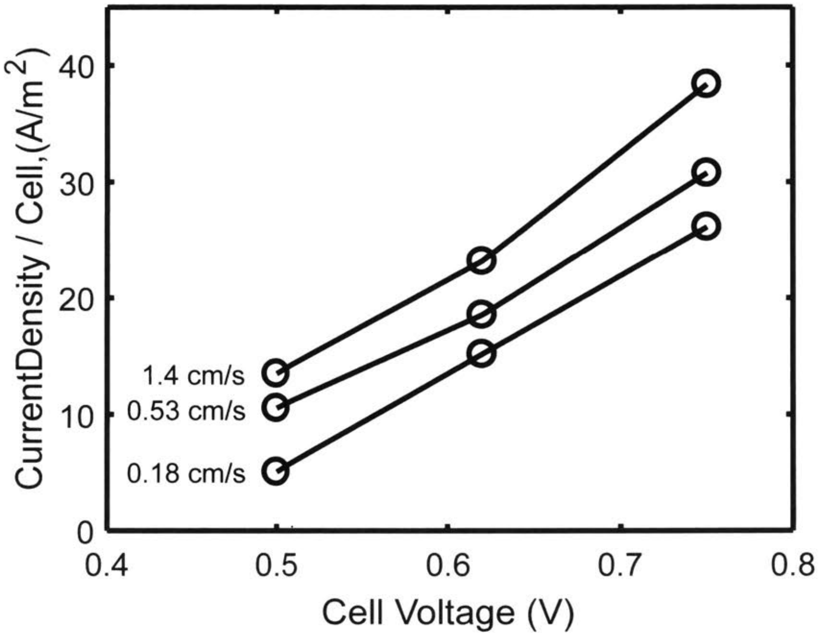

Figure 5-19: Effect of superficial velocity on EMAR 8.1 stack.

previous experiments, the EMAR 8.1 stack was loaded into the EMAR apparatus. A suite of experiments was completed, varying flow rate - and subsequently superficial velocity - as well as cell voltage.

As one may expect, increasing superficial velocity diminishes transport boundary layers and as a result diminishes transport overpotentials. Further, the decrease in residence time which accompanies the increase in superficial velocity minimizes the total copper loading shift, which decreases the thermodynamic overpotential, as seen in Chapter 3. As shown in Figure 5-19 these two factors work in concert to increase current density in the EMAR 8.1 cell in response to increasing superficial velocity.

Summary and Conclusions

Previous chapters established the thermodynamic and transport behavior of the EMAR process. This chapter detailed how those theoretical approaches where implemented on a lab scale. The process flow scheme which supports the EMAR desorber and controls the experimental apparatus, was first introduced before detailing the design and construction of a variety of EMAR cells. Two types of EMAR cells were discussed, single cell systems and stacked systems.

EMARs 2 through 7 were single cell systems, previously introduced by Stern and Eltayeb.[1,2] EMAR 2 and EMAR 3, designed by Stern, where o-ring sealed systems with fixed channel depths. These designs suffered minor leaks and were less flexible that the EMAR designs which would follow. EMAR 4 was designed by Stern as well, and incorporated a flexible gasket channel which was more adaptable than previous systems. Mystic River Engineering under Eltayeb management, improved on the EMAR 4 design, making a more robust EMAR 5. EMAR 6 was a single cell, multi-electrode design which allowed for resolution into the anodic and cathodic current density profiles. EMAR 7, designed by Mystic River Engineering under Shaw (author) management, allowed for high pressure EMAR cell operation.

Two stacked system designs were discussed: a parallel systems - EMAR 8.1 - and series system - EMAR 8.2. The parallel configuration requires high current, low potential operation, where as the stack system allows for low current, high potential operation. Both systems employ a manifold geometry, similar to that of a flat plate heat exchanger, which allows for simple desorption scale up. EMAR 9, which incorporates an pack column absorber to match the desorption capacity of EMAR 8.x, was briefly introduced.

The efficacy of EARM 8.x's design and construction was tested through a suite of experiments. These experimental results serve also to validate the transport model discussed in Chapter 4 as well as expand our knowledge of the EMAR process. This work demonstrated the effect of inlet copper loading on the EMAR process. It showed that chloride based supporting electrolytes demonstrate transport limited behavior, which is in contrast to nitrate based supporting electrolytes which show kinetic limited behavior. Further, it was shown that the EMAR stack does not exhibit a decrease in faradaic efficiency over a limited reversibility study.

Chapter 6

Capstone Chapter: The Economics of EMAR

This chapter provides a methodology to approximate the capital expenses associated with the EMAR electrochemical desorption system. It specifically describes a full scale EMAR stack geometry as well as the bill of materials which would result from that geometry. This chapter then provides a summary of the work by Miao Wang and Dr. Emre Gençer who expand on this methodology in a detailed manner in order to approximate the total cost of CO_2 avoided should EMAR be employed on a 500 MW power plant. It is shown that the total cost per metric ton of CO_2 avoided would likely run between \$60 and \$75.

In light of this estimate, this chapter briefly analyses potential markets for the EMAR process. It concludes that most promising market for EMAR technology is that of carbon dioxide separation as a service, specifically in natural gas sweetening. A five

Symbol	Name	Price Range
Cu	Copper	\$6.0 - \$6.5 / kg
ss	Stainless Steel	\$2.5 - \$3.0 / kg
gr	Graphite	\$1.5 - \$2.0 / kg
pl	Plastic	\$1.0 - \$1.5 / kg
mem	Membrane	\$1 - \$50 / m^2

Table 6.1: Components of Bill of Materials and approximate prices

forces analysis is completed in order to make strategic suggestions for operation in such a market.

It should be emphasized that the analysis in this chapter applies specifically to the three-stage EMAR process seen through this thesis. As suggested in previous chapters an EMAR process which employs a cathodic absorption would bring down operating cost substantially through thermodynamic efficiency gains and potentially capital costs through process intensification. We therefore expect a two-stage EMAR process to be competitive in more markets than just those analyzed below.

EMAR Capital Expenses Model

The objective of this portion of the costing analysis is to determine the quantity of five materials, which are assumed to make up the majority of the cost of materials of an EMAR stack. These materials and their approximate prices are given in Table 6.1. Further, to provide an estimation of the footprint of an EMAR desorber system geometry and size is determined.

Figure 6-1 gives the calculation architecture that is employed. Calculations are made in two phases: (1) a geometry independent analysis and (2) an analysis that depends

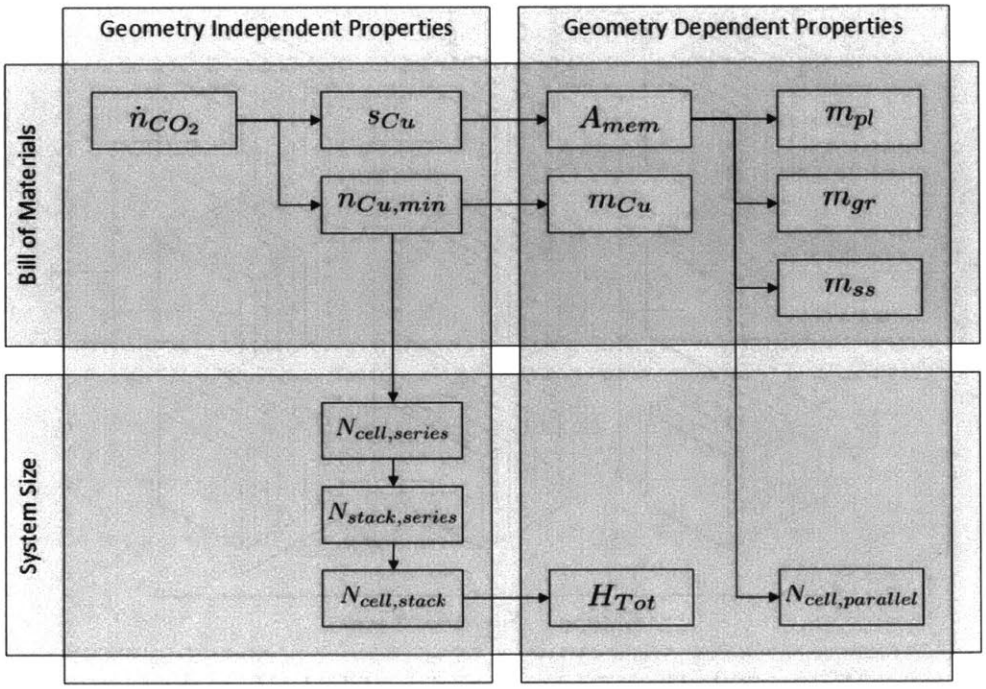

Figure 6-1: Calculation order to determine bill of materials and system size

on one of two system geometries - flat plate or porous. While figure 6-1 gives the calculation order, it is important to note that the inputs are not shown in this figure. They are instead discussed in the "Independent/Decision Variables" section below.

Note on Electrical Orientation of Stacks

As shown in Figure 6-2 an EMAR stack consists of many EMAR unit cells and EMAR stacks may be aligned in series and in parallel. As discussed below, EMAR unit cells are aligned electrically in series in a stack. The following relationships come directly from Figure 6-2 and will be useful for the analysis below.

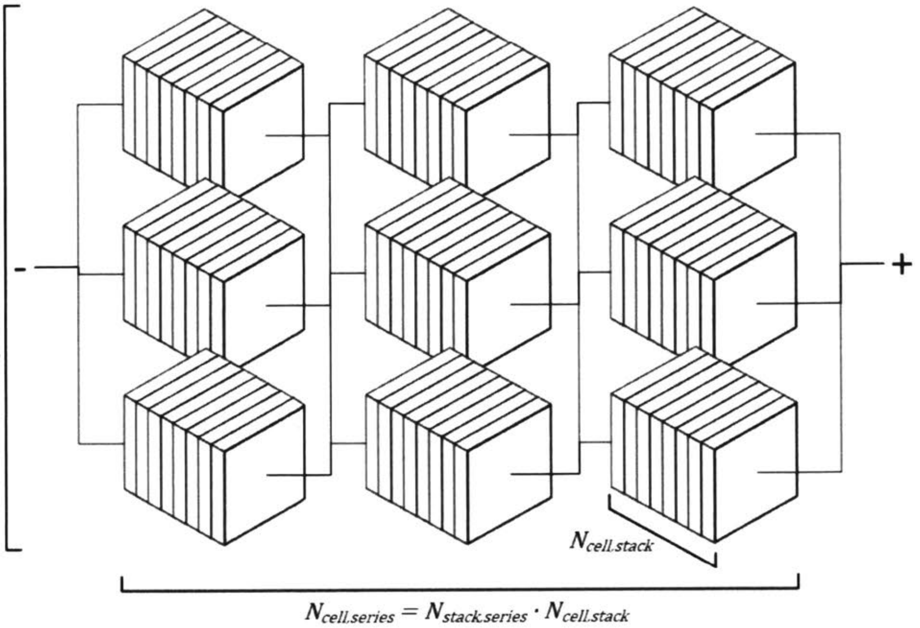

Figure 6-2: Electrical orientation of EMAR stacks

$$N_{cell} = N_{cell,series} \cdot N_{cell,parallel} = N_{stack,series} \cdot N_{stack,parallel} \cdot N_{cell,stack} = N_{stack} \cdot N_{cell,stack} \tag{6.1}$$

$$N_{cell,series} = N_{stack,series} \cdot N_{cell,stack}, \qquad N_{cell,parallel} = N_{stack,parallel} \tag{6.2}$$

Independent/Decision Variables

This cost model takes in the following independent variables to establish the total materials requirement.

Symbol	Description
A_{max}	Maximum unit cell cross sectional area
c_{Cu}	Fraction of copper consumed before regeneration
e_i	Material i (Copper, plastic, graphite) excess required (flat plate only)
f_e	EMAR faradaic efficiency
H_{mem}	Membrane thickness
H_{ch}	Channel thickness
H_{HX}	Thickness of graphite heat exchanger
H_{ss}	Thickness of stainless steel end plate
I_{max}	Maximum current to EMAR process
i	Current density seen in unit cell
$\dot{m}_{CO_2,e}$	CO_2 emission from flue gas
$N_{cell,stack,max}$	Maximum number of unit cells in a stack
n_{HX}	Number of cells per heat exchange plate
x_{cap}	Fraction of CO_2 emission captured
α_{Cu}	Specific surface area of copper foam (porous only)
ε_i	Material i void space (plastic, graphite) required
τ_c	Time before switching cycle

Table 6.2: Independent/Decision variables used

Geometry Independent Properties

A number of properties of an EMAR stack are independent of the cell geometry. These properties are established below and are used to determine the geometry dependent properties described in the following section.

Molar Flow Rate of CO_2 Captured, $\dot{n}_{CO_2}$

$$\dot{n}_{CO_2} = \frac{\dot{m}_{CO_2,e} \cdot x_{cap}}{M_{CO_2}} \tag{6.3}$$

Total Copper Surface Area, s_{Cu}

$$s_{Cu} = \frac{\dot{n}_{CO_2} \cdot F}{i \cdot f_e} \tag{6.4}$$

Minimum Copper Required, $n_{\mathrm{Cu},min}$

At minimum we require enough copper to last for the switching time length, plus a safety buffer.

$$n_{Cu,min} = \underbrace{\frac{\dot{n}_{CO_2} \cdot \tau_c}{2 \cdot f_e}}_{\text{Copper shift}} \cdot \underbrace{\left(1 + 2 \cdot \left(\frac{1 - c_{Cu}}{c_{Cu}}\right)\right)}_{\text{Buffer}} \tag{6.5}$$

Number of Cells in Series, $N_{cell,series}$, Stacks in Series, $N_{stack,series}$, and Cells per Stack, $N_{cell,stack}$

We require a minimum number of cells in series in order to bring the amperage to or below the maximum amperage established above.

$$N_{cell,series} = \left\lceil \frac{i \cdot s_{\mathrm{Cu}}}{I_{max}} \right\rceil = \left\lceil \frac{\dot{n}_{CO_2} \cdot F}{I_{max} \cdot f_e} \right\rceil \tag{6.6}$$

$$N_{stack,series} = \left\lceil \frac{N_{cell,series}}{N_{cell,stack,max}} \right\rceil \tag{6.7}$$

$$N_{cell,stack} = \left\lceil \frac{N_{cell,series}}{N_{stack,series}} \right\rceil \tag{6.8}$$

Switching Time Considerations

Consider a EMAR desorption system which needs to be regenerated after a time period of τ_c and which takes a time of τ_s to reach steady state after switching. Further, assume this is done such that EMAR stacks are reversed and regenerated in a staggered manner, rather than all at once. For convenience, this staggered regeneration should occur within stacks that are electrically in parallel. In that case, the fraction of up-time a given stack will see is $\tau_c / (\tau_c + \tau_s)$. We will therefore require τ_s/τ_c stacks more than the minimum required, to allow for down time. There is therefore factor of $1 + \tau_s/\tau_c$ seen in both the membrane area and the copper requirements, which propagates to all of the bill of materials and the number of stacks in parallel.

Geometry Dependent Properties

The following sections describe two geometries and from these geometries and the parameters and variables given above establish the bill of materials and remaining system size parameters.

Flat Plate Geometry

Figure 6-3 shows the unit cell geometry used for a flat plate system in this model. A unit cell consists of two copper plates, two flow channels, and a membrane. The membrane separates the anodic and cathodic flows, which occur in and are sealed by the plastic flow channels. The stack is assumed to be electrically in series, therefore

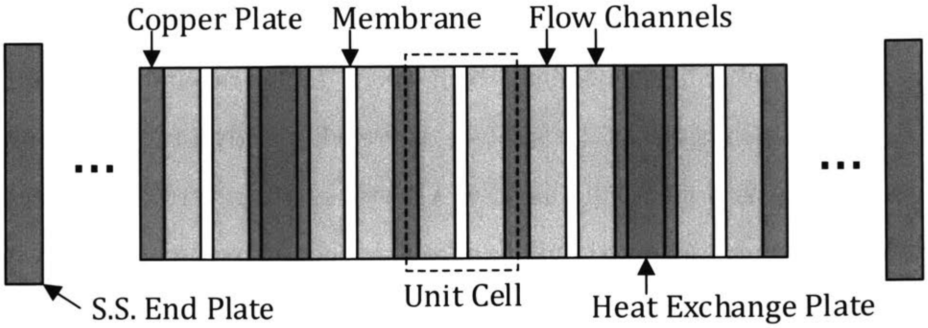

Figure 6-3: Flat plate stack geometry

each copper plate acts a bi-polar separator acting as a cathode on one side and an anode on the other. Graphite heat exchangers, which allow the stacked to be heated, are placed in the stack an interval specified in Table 6.2.

Per Figure 6-1 we have the following relationships which describe the bill of materials for a flat plate EMAR desorber.

$$A_{mem} = \left(1 + \frac{\tau_s}{\tau_c}\right) \cdot s_{Cu} \tag{6.9}$$

$$m_{Cu} = \left(1 + \frac{\tau_s}{\tau_c}\right) \cdot n_{Cu,min} \cdot (1 + e_{Cu}) \cdot M_{Cu} \tag{6.10}$$

$$m_{pl} = 2 \cdot A_{mem} \cdot H_{ch} \cdot (1 + e_{pl}) \cdot (1 - \varepsilon_{pl}) \cdot \rho_{pl} \tag{6.11}$$

$$m_{gr} = \frac{A_{mem} \cdot H_{HX} \cdot (1 + e_{gr}) \cdot (1 - \varepsilon_{gr}) \cdot \rho_{gr}}{n_{HX}} \tag{6.12}$$

$$m_{ss} = 2 \cdot H_{ss} \cdot A_{mem} \cdot (1 + e_{ss})\, \rho_{ss} \tag{6.13}$$

Per Figure 6-1 we have the following relationships which describe the stack size and number of stacks in parallel for a flat plate EMAR desorber.

$$H_{Cu} = \frac{n_{Cu,min} \cdot M_{Cu}}{2 \cdot \rho_{Cu} \cdot s_{Cu}} \tag{6.14}$$

$$H_{Tot} = N_{cell,stack} \cdot \left(2 \cdot H_{Cu} + 2 \cdot H_{ch} + H_{mem} + \frac{H_{HX}}{n_{HX}} \right) + 2 \cdot H_{ss} \tag{6.15}$$

$$N_{stack,parallel} = \left\lceil \frac{A_{mem}}{N_{stack,series} \cdot A_{max}} \right\rceil \tag{6.16}$$

Porous Geometry

Figure 6-4 shows the unit cell geometry used for a porous system in this model. A unit cell consists of two flow channels, each filled with porous copper, and a membrane. As in the flat plate case, unit cells are assembled electrically in series. A thin, bipolar, inert plate separates anodes and cathodes from adjacent unit cells. Graphite heat exchangers, which allow the stacked to be heated, are placed in the stack an interval specified in Table 6.2.

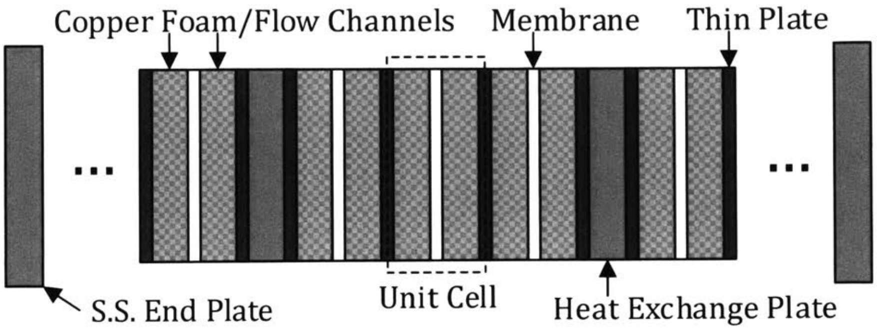

Figure 6-4: Porous stack geometry

Per Figure 6-1 we have the following relationships which describe the bill of materials for a porous EMAR desorber.

$$A_{mem} = \left(1 + \frac{\tau_s}{\tau_c}\right) \cdot \frac{s_{Cu}}{\alpha_{Cu} \cdot H_{ch}} \tag{6.17}$$

$$m_{Cu} = \left(1 + \frac{\tau_s}{\tau_c}\right) \cdot n_{Cu,min} \cdot M_{Cu} \tag{6.18}$$

$$m_{pl} = 2 \cdot A_{mem} \cdot H_{ch} \cdot (1 + e_{pl}) \cdot (1 - \varepsilon_{pl}) \cdot \rho_{pl} \tag{6.19}$$

$$m_{gr} = \frac{A_{mem} \cdot H_{HX} \cdot (1 + e_{gr}) \cdot (1 - \varepsilon_{gr}) \cdot \rho_{gr}}{n_{HX}} \tag{6.20}$$

$$m_{ss} = 2 \cdot H_{ss} \cdot A_{mem} \cdot (1 + e_{ss})\, \rho_{ss} \tag{6.21}$$

Per Figure 6-1 we have the following relationships which describe the stack size and number of stacks in parallel for a flat plate EMAR desorber.

$$H_{Tot} = N_{cell,stack} \cdot \left(2 \cdot H_{ch} + H_{mem} + \frac{H_{HX}}{n_{HX}}\right) + 2 \cdot H_{ss} \tag{6.22}$$

$$N_{stack,parallel} = \left\lceil \frac{A_{mem}}{N_{stack,series} \cdot A_{max}} \right\rceil \tag{6.23}$$

Cost of CO_2 Avoided - Initial Results

Miao Wang, a PhD candidate in the Hatton Group, with assistance from Dr. Emre Gençer, a Research Scientist with MIT Energy Initiative, has significantly expanded on the above material, to provide a detailed cost estimate for the entire EMAR process. They consider both operating and capital expenses for the whole cycle as it would be incorporated into a 500 MW coal fired power plant in order to approximate the total cost of CO_2 avoided. This analysis, which will be presented in a forth coming publication, allows for an apples-to-apples comparison between EMAR and other carbon dioxide capture technologies. The following is a brief summary of Wang's analysis and has been included below with his permission.

The cost of carbon capture is determined on a cost of CO_2 avoided bases as given in equation 6.24, where cost of energy, COE, and CO_2 emissions are given with the same basis (say $\$/(kW \cdot hr)$ and $tonne/(kW \cdot hr)$ respectively).

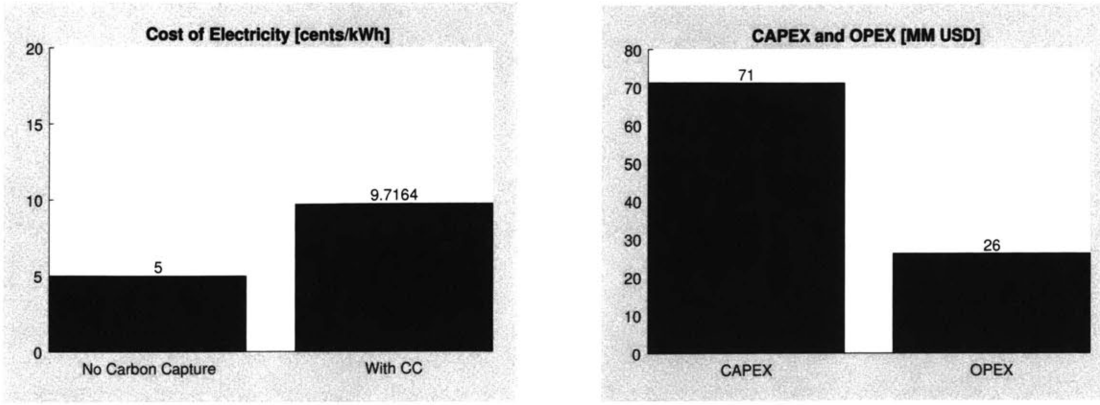

(a) Cost of electricity with and without CO_2 capture

(b) Comparison of CAPEX and OPEX on a yearly basis using a 14% levelized capital charge factor

Figure 6-5: Cost considerations for EMAR Capture

$$\text{Cost of } CO_2 \text{ avoided} = \frac{COE_{\text{with capture}} - COE_{\text{without capture}}}{CO_2 \text{ emissions with capture} - CO_2 \text{ emissions without capture}} \tag{6.24}$$

As shown in Figure 6-5a a typical EMAR installation is estimated to raise the cost of electricity from a base case of $\$0.05/(kW \cdot hr)$ to $\$0.097/(kW \cdot hr)$ - the difference being the numerator of equation 6.24. Of that, roughly 75% of the cost comes from capital expenditures rather than operating expenditures as seen in Figure 6-5b. Capital expenditures are estimated at roughly $500 million, whereas operating expenses are estimated at $25 million per year for the 500 MW power plant.

Wang's analysis shows membrane costs, which are relatively unknown compared to other major capital expenditures, represent a significant cost driver for such a process. The impact of this capital cost driver is given in Figure 6-6. On the operating side, four parameters dominate: desorption pressure, copper loading shift,

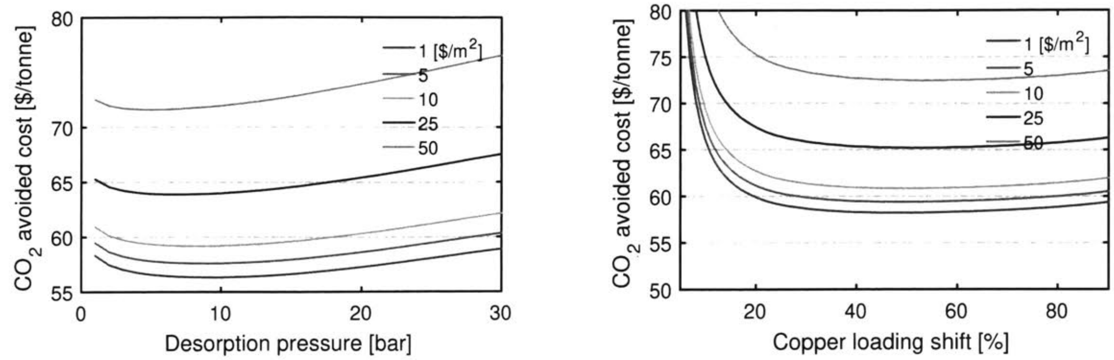

(a) Impact of desorption pressure

(b) Impact of copper loading shift

Figure 6-6: Impact of membrane cost, desorption pressure, and copper loading shift on cost of CO_2 avoided

desorption temperature, and applied overpotential. Figure 6-6 focuses on the former two, as these where the primary points of focus for Chapter 3. The conclusions are qualitatively similar to those in Chapter 3, i.e. we are content operating at a higher (>50%) copper loading shift to keep capital expenses down and desorption pressure should be roughly 10 bar.

Cost Effective EMAR Applications

As seen in Figure 6-6, the total cost per metric ton of CO_2 avoided would likely run between \$60 and \$75. When we compare the EMAR process to traditional and more novel thermal processes, we see that while comparable, EMAR will not necessarily be competitive. An apples-to-apples comparison of EMAR to thermal processes introduced by Rochelle et. al. given in Figure 6-7 shows this advantage in more detail.[46] This is not to say however, that EMAR does not have a place in

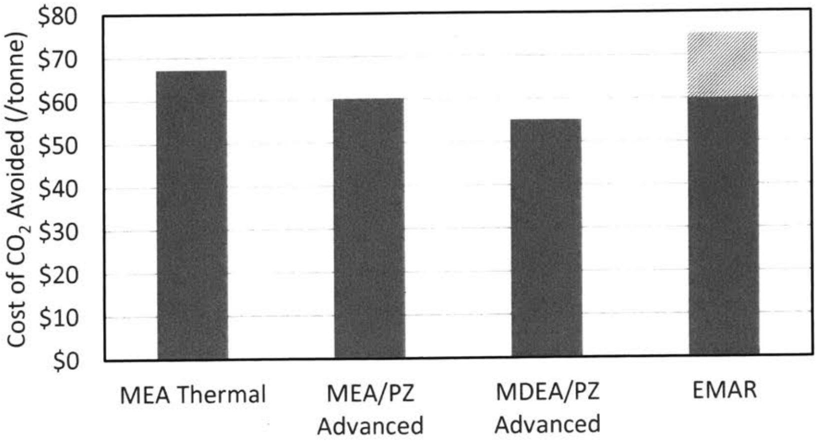

Figure 6-7: Cost comparison between EMAR and incumbent thermal amine processes.[46]

the carbon capture ecosystem. What follows therefore is a brief analysis potential targets for carbon dioxide capture and a discussion of where EMAR may be able to compete in this arena.

Eltayeb considered three broad markets within which EMAR could compete.[2] A brief description of each is given below.

Sale of CO_2 into Enhanced Oil Recovery

Enhanced Oil Recovery (EOR) is a method of extracting additional oil from a well that otherwise could not be removed via conventional processes - natural pressure or solvent based secondary recovery. In this process supercritical CO_2 is injected into an oil well, dissolving and displacing some of the remaining oil. EOR is by far the largest consumer of CO_2, demanding roughly 2/3's of the 80 million tons per year of CO_2 consumed. EOR is therefore a natural potential buyer of carbon dioxide captured from anthropogenic sources.

There are two headwinds facing EMAR in the sale of captured carbon dioxide into EOR. The first, discussed above, is the expectation that more novel thermal amine approaches will be more economical in traditional power plant capture than EMAR (more niche applications where EMAR has an advantage will be discussed below). This will of course allow CO_2 captured from these sources to undercut CO_2 captured from an EMAR process. The second is a headwind facing all captured anthropogenic carbon dioxide sources. CO_2 is naturally occurring, may be produced industrially, and is sold generally via a network of pipelines - see Figure 6-8. CO_2 price is tied to oil prices and transportation costs, but can be estimated at roughly around \$40 per metric ton.[47] This is well below the costs of CO_2 avoided presented in Figure 6-7 and therefor would need an additional regulatory revenue driver (see discussion below) to operate profitably.

Emissions Mitigation

National parties representing 56% of global greenhouse gas (GHG) emissions, have, in response to the Paris Agreement, implemented or are planning to implement carbon pricing to mitigate GHG emission. The total value of these carbon taxes for 2018 was \$82 billion.[49] While the carbon price varies wildly by geography, with Sweden currently implementing the highest price of \$139 / tCO_2e (metric ton of CO_2 equivalent), the EU Emissions Trading System (EU ETS) provides a middle of the road estimate of carbon dioxide prices. Figure 6-7 provides historical carbon costs from EU ETS, which at the time of this writing (January 2019) are between 20 and 25 €/tCO_2e (22 to 29 \$/tCO_2e).

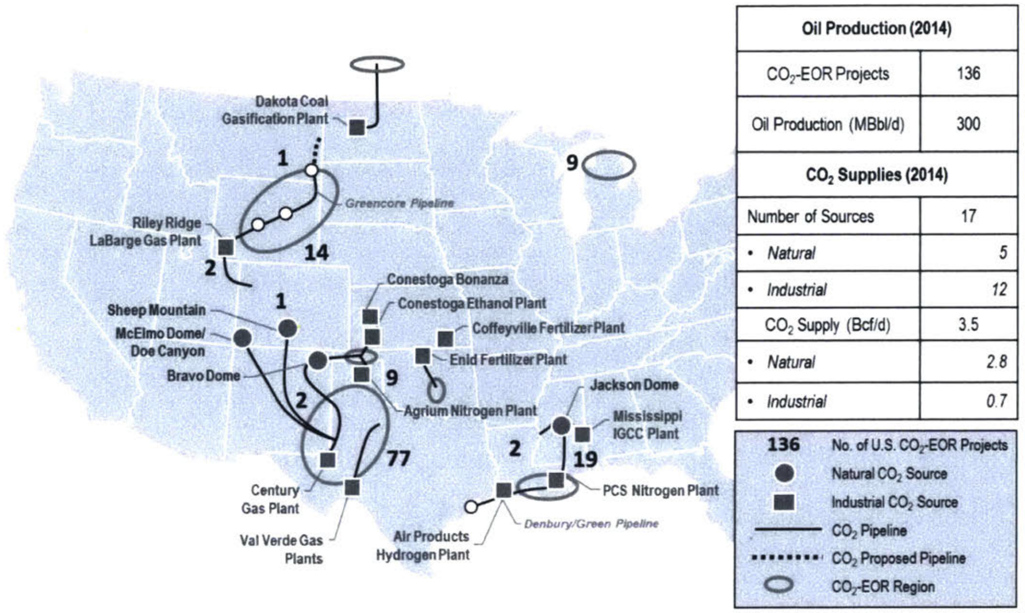

Oil Production (2014)	
CO_2-EOR Projects	136
Oil Production (MBbl/d)	300
CO_2 Supplies (2014)	
Number of Sources	17
• *Natural*	5
• *Industrial*	12
CO_2 Supply (Bcf/d)	3.5
• *Natural*	2.8
• *Industrial*	0.7

Source: Advanced Resources International, Inc., based on Oil and Gas Journal, 2014 and industry sources

Figure 6-8: US CO_2 pipelines for enhanced oil recovery[48]

Figure 6-9: European carbon dioxide emission allowances price (€/tCO_2e) on EU Emissions Trading System (EU ETS)[50]

Carbon dioxide producers, like the coal fired power plant analyzed above, could use CO_2 capture technologies to capture and store or sell emissions rather than pay the above carbon prices. With the exception of outliers like Sweden, Figure 6-7 shows that it is unlikely that carbon capture could be justified on emissions mitigation alone. There are some cases however, where a combination of regulatory pressures and EOR sales opportunities make CO_2 capture economically viable. In those cases, Figure 6-7 also shows that more advanced thermal amine schemes would likely be preferable to EMAR. It is expected that some niche applications exists, say those that require frequent start-up and shut-down of that do not have access a sizable boiler (perhaps cement production), where EMAR can compete economically with advanced thermal amine schemes.

CO_2 Separation as a Service

One, potentially more promising approach to EMAR commercialization is to consider carbon dioxide removal not in the context of CO_2 sales or emission mitigation, but as a service to remove an unwanted impurity (CO_2) from an otherwise valuable stream. These applications are of particular interest, because they may value ease of deployment over CO_2 avoidance cost. Eltayeb suggests potential applications for EMAR in this area, which are summarized below.[2]

Life-Support Systems for Confined Spaces Consider a confined living space such as a submarine or space craft. In order to mitigate carbon dioxide buildup in the air, which needs to be kept below 0.5% by volume, thermal swing zeolite systems or lithium hydroxide canisters are employed as CO_2 adsorbents. While EMAR does offer continuous removal without the need for thermal swing, which would be attractive in this application, headwinds in this case include both a small market and the fact that EMAR is liquid state (as compared to the previously described adsorption processes which are solid state), making stability of paramount concern.

Building Energy Consumption Mitigation Buildings, like the confined spaces above, need to maintain low concentrations of carbon dioxide. This is completed by exchanging air with the environment, taxing the HVAC system. It's conceivable that this exchange could be mitigated by using a plug-and-play EMAR process to remove the CO_2 directly, and thereby minimize the work to be done by the HVAC system. However, the same effect can be generated using a simple air to air cross-flow heat exchanger; presumably at a much lower capital cost and a non-existent operating expense.

Natural Gas Sweetening Removal of acid gases (like carbon dioxide or hydrogen sulfide) from natural gas is required to meet pipeline specifications. A number of natural gas sources contain potentially high levels of carbon dioxide to be treated. These include: sites where natural gas is a byproduct and is flared, biogas upgrading facilities, and high CO_2 concentration natural gas wells. Tailwinds for such natural gas sweetening include a large and growing market and a large pool of customers which are not currently or could not ever reasonably be served by thermal separation processes or other substitute purifications like pressure based systems.

Note on H_2S impact on EMAR Process

The astute reader may notice that hydrogen sulfide will adversely affect the EMAR process by removing copper (the electrochemically active blocking agent) from solution and by protonating (and thereby rendering inactive) the amine in the absorber. This may be an issue for treating high H_2S streams, however the flowing method may be employed to recover copper lost to small amounts of H_2S in a treatment stream.

Amine protonation and copper removal

$$\begin{array}{l}
\mathrm{H_2S(g)} \rightleftharpoons \mathrm{H^+(aq)} + \mathrm{HS^-(aq)} \\
\mathrm{H^+(aq)} + \mathrm{EDA(aq)} \rightleftharpoons \mathrm{EDAH^+(aq)} \\
\mathrm{HS^-(aq)} + \mathrm{Cu^{2+}(aq)} \longrightarrow \mathrm{CuS(s)} + \mathrm{H^+(aq)} \\
\hline
\mathrm{H_2S(g)} + 2\,\mathrm{EDA(aq)} \longrightarrow 2\,\mathrm{EDAH^+(aq)} + \mathrm{CuS(s)}
\end{array}$$

Reversing the effects using CuO and heat

$$\begin{array}{l}
\mathrm{CuS(s)} + \tfrac{3}{2}\mathrm{O_2(g)} \xrightarrow{\Delta} \mathrm{CuO(s)} + \mathrm{SO_2(g)} \\
2\,\mathrm{EDAH^+(aq)} + \mathrm{CuO(s)} \rightleftharpoons 2\,\mathrm{EDA(aq)} + \mathrm{Cu^{2+}(aq)} + \mathrm{H_2O} \\
\hline
\mathrm{CuS(s)} + \tfrac{3}{2}\mathrm{O_2(g)} + 2\,\mathrm{EDAH^+(aq)} \xrightarrow{\Delta} \mathrm{SO_2(g)} + 2\,\mathrm{EDA(aq)} + \mathrm{Cu^{2+}(aq)} + \mathrm{H_2O}
\end{array}$$

Strategic Analysis and Commercialization Thesis - A Five Forces Analysis

As the above analysis makes clear, applying the EMAR process to natural gas sweetening may be the most economically viable option for commercialization. The central reason for this is separation as a service can take advantage of EMAR's plug-and-play nature without being unnecessarily brought down by EMAR's slightly higher cost in traditional carbon capture applications. On top of that natural gas usage is growing on the back of advances in hydraulic fracturing technology. What follows then, is a brief analysis of the natural gas treatment market and strategic suggestions for EMAR's implementation in that market.

There are three sections of this market worth exploring.[2]

Oil Production Sites Which Flare Sour Methane Many oils wells (targeting liquid hydrocarbons) have small amount of sour natural gas byproduct. In 2012, more than 100 billion cubic meters of gas were flared globally, resulting in the emission of greater than 350 million metric tons of CO_2.[51] These came from for than 7,000 flares predominantly in the USA and Russia.[52] Given the relatively small size of these flares and potentially remote geographies, thermal amine process tend not to be economically feasible, whereas a plug-and-play EMAR process may be feasible. At current natural gas prices, $3.16 per MMBTU (million btu) (note 1000 cubic feet is approximately 1 MMBTU), this is a total potential market of $12 billion per year or $1.6 million per flare per year.

CO_2 Heavy Natural Gas Reservoirs Globally 4 trillion cubic meters net of hydrocarbon gas has CO_2 content between 15% and 80%. Significantly more natural gas reserves, roughly half of the 27 trillion cubic meters, have 2% or more CO_2 content.[53] Considering only the very sour gas reserves (15% to 80% CO_2) leaves $300 billion in sour natural gas. Again, EMAR may have an advantage here over thermal processes and incumbent membrane processes thanks to high selectivity and minimal to no dependence on steam.

Biogas Upgrading Biogas, generally to product of anaerobic digestion of waste, can be upgraded to a higher caloric value my removing carbon dioxide, which can make up 25% - 50% of the raw biogas mixture. While this segment is smaller than the above, the required small scale deployment makes EMAR potentially attractive.

An enterprise centered around EMAR technology could serves the above segments by focusing on separations that can take advantage of two benefits EMAR offers over Thermal Amine namely: plug and play (requiring little to minimal steam) and able to handle significant variability by starting-up and shutting down more easily than Thermal Amine.

Porter's Five Forces

In order to analyze the natural gas purification in which EMAR could play, we will use a framework developed by Michael Porter of the Harvard business school known as "The Five Competitive Forces."[54] Porter states that five forces describe the competitive landscape of a market. These forces are:

Bargaining Power of Buyers The buyers in this market are the natural gas producers from any of the above segments. They buy a service, natural gas purification, from EMAR or any potential competitor. A powerful customers base may have the ability to force down prices cutting into profitability. It will be shown below, that customer bargaining power is likely minimal.

Rivalry Among Existing Competitors In this case, we will define competitors as thermal amine processes, other separation processes will be addressed in the "Threat of Substitute Products or Services" section as these other processes are demonstrably different from amine based processes. It will be shown that in order to minimize rivalry among existing competitors, which can decrease profitability across the board, it will be important that EMAR to focus on greenfield projects, where thermal amine does not/cannot compete.

Threat of Substitute Products or Services There are a number of possible substitute services, these include: membrane separation systems, pressure swing adsorption, or simply doing nothing. In this case there is a moderate through of substitutes, which will need to be mitigated through diversification or, as above, through targeted project work.

Bargaining Power of Suppliers Suppliers provide the key raw materials required for construction and operation of EMAR processes. We will see that suppliers have little power to capture significant value created by EMAR, with the exception membrane producers who provide a unique, vital, and potentially expensive product for EMAR.

Threat of New Entrants New entrants are an ever-present threat especially in new or evolving markets like this one. Discussed below are barriers to entry which may be erected against new entrants.

The following sections analyze each of these five forces in detail.

Bargaining Power of Buyers

The bargaining power of buyers is of paramount concern, because a powerful customers base may have the ability to force down prices cutting into profitability. The natural gas producers (buyers in this market) have relatively weak bargaining power for three reasons.

Buyers have fairly low concentration, but its growing Concentrated markets, with only a few buyers, have the ability to push down prices – much like a monopoly supplier can push up prices. The case of flared methane we have more than 7,000 flares across more than 20 countries (though the USA and Russia dominate).[52] Further, biogas upgrading brings in waste treatment/removal market, which decreases the dominance of oil/gas buyers. Still, upstream oil and gas has seen growing concentration, especially in the US since the 1990s[55] as seen by Exxon's dominance.

Products are very differentiated between vendors and switching cost are high This thesis has detailed the differences between carbon dioxide separation technologies. These stark differences bring down buyer power because they do not allow for standardization across vendors. There is therefore no opportunity to play one vendor off of another, driving down prices. Further, the high capital costs of CO_2 separation technologies make switching between vendors, should a lower cost technology emerge, quite difficult.

Figure 6-10: Natural gas price in \$/MMBTU over the last 10 years as reported by NASDAQ

Buyers cannot easily back integrate EMAR technology Buyers could drive down prices by threatening to perform the separation themselves. This threat is not credible because electrochemistry is not historically a strength of either the oil and gas industry or the waste management industry.

While natural gas producers may have weak bargaining power, their price sensitivity is also of interest when considering their behavior in this market. As shown in Figure 6-10, the price of natural gas varies significantly in time. Over the last 10 years prices have varied between \$2 and \$5.50 per MMBTU. This is roughly \$100 to \$300 per metric ton of natural gas. Consider then a case where a natural gas stream has 33% CO_2 in it. Given the cost reported in Figure 6-7 above, CO_2 removal would cost \$35 per met ton of natural gas produced. At a low natural gas price this is likely excessive (30% of total revenue), however at a high natural gas price this is likely acceptable (10% of total revenue). As will be discussed below EMAR's ability to easily go from off-line to on-line (and vice versa) can take advantage of this significant variation.

Rivalry Among Existing Competitors

While rivalry will certainly exist between EMAR and Thermal Amine Scrubbing, this is unlikely to be disruptive to profitability. There are two reasons for this. First, competition between EMAR and Thermal Amine Scrubbing will occur on different dimensions. Thermal Amine appears to be a low cost provider, suitable for natural gas sources that have a large boiler readily available and do not need to bring the separation train up or down regularly. EMAR on the other hand may have a higher cost, but is more plug-and-play and is suitable for natural gas sources that need flexibility on separation train and cannot support/do not have available a boiler. Second, despite high capital costs, both solutions have significant marginal costs. If marginal costs are low pressure is created to force prices down. Thermodynamics (as discussed throughout this thesis) forces marginal costs to be significant, eliminating this downward pressure on prices. Since, it appears thermal amine has a cost advantage in areas where is currently competes, it will be important to focus on greenfield projects, where thermal amine does not/cannot compete. This will avoid rivalry eroding potential profits.

Threat of Substitute Products or Services

A number of substitute products exist to treat CO_2 laden natural gas streams. These include: membrane separation systems, pressure swing adsorption, or simply doing nothing (not treating the sour methane). In this case there seems to be a moderate threat of substitutes driven, in opposite directions, by the two following factors.

A price/performance trade-off exists with the potential substitutes Customers have the option of choosing from multiple performances levels. For example, membrane separation offers low capital requirements, but provides low selectivity (up to 1/3 of natural gas loss) and moderate operating expense (roughly in line with Thermal Amine). Pressure swing adsorption on the other hand may provide higher selectivity than membrane separation, but at a high capital cost and low throughput. Taking this point to it's extreme, potential buyers may also elect to not perform a separation (instead flaring for example). These varying substitute options threaten to both pull down prices and erode total addressable market

Switching cost is high The price/performance optionality is mitigated slightly by high switching costs. As discussed above, the high capital costs will prevent erosion of existing business to substitutes.

It will be important to moderate this threat by either diversifying (teaming up with a substitute product) or as above, moving to greenfield/niche projects less at risk of substitutes.

Bargaining Power of Suppliers

Powerful suppliers can demand a larger portion of the value created by EMAR, thereby eroding potential profits from the beginning. There are a number of key suppliers for the EMAR process. These include:

- Chemical companies, who provide the amines
- Material suppliers, for material like copper, stainless steel, graphite, and other auxiliary materials
- Engineering/Construction companies, who would be required to build the plant
- Membrane suppliers, as we saw above membrane costs are critical to the overall cost of EMAR
- Power suppliers, who provide power to the electrochemical desorption

These suppliers fall into two camps: those who supply undifferentiated products and those who supply unique and vital products. For most suppliers (all but membrane producers), the products offered are nearly interchangeable and switching costs are nearly zero. For example, it does not matter to the EMAR process if the amines are produced by DOW or Eastman Chemical. This gives the option to play one supplier off of the other to extract a lower price. Membrane suppliers are the obvious exception as they have significant product knowhow and patent protection in addition to providing a product that is unique and vital to the EMAR process.

In order to keep supplier bargain power low, it will be important to keep operating in an environment where suppliers have low margin and products an interchangeable. Therefore, if possible it is best to avoid non-commodity materials like amines or amine mixes under patent. Membrane companies represent a significant risk that could be mitigated by negotiating bulk discounts or long term partnerships. A similar approach may be taking with power suppliers by negotiating long term contracts.

Threat of New Entrants

New entrants are an ever-present threat especially in new or evolving markets like this one as they can drive down prices or erode market share. While this analysis will not attempt to guess at what new technologies may take hold in the future, we will discuss barriers to entry which may be erected against these new entrants.

Two barriers to entry exist or may be erected which may mitigate the threat of new entry in the long term. The first which may be built is the use of long term contracts, which buyers should be amenable to since buyers experience high switching costs. These contracts could help bare the entry of new competition. The second, preexisting barrier, is high capital costs. As discussed before the high capital costs associated with CO_2 removal from natural gas provide their own barriers to entry.

Five Forces Summary

This is a market characterized by buyers (natural gas producers/suppliers) that have a low concentration and a regularly subjected to price variation, strong competition or threat of substitutes that may be mitigated through targeted project execution, and suppliers who's influence ranges from marginal to vitally important. EMAR has a two advantages which make this market potentially attractive: (1) the ability to easily go from off-line to on-line (and vice versa) in order to take advantage of process or market variation and (2) a plug-and-play system design which does not require an intrusive boiler. Still, in order to operate profitably in this market, EMAR needs to make a few key strategic decisions. These include:

- Focus on greenfield projects, where thermal amine or other substitutes do not/cannot compete, especially those that can benefit most from the two above EMAR advantages
- If possible, moderate the threat of substitutes and spread risks by diversifying (example: teaming up with an adsorption process)
- Avoid non-commodity materials like an amines or amine mixes under patent
- If possible, mitigate the risk presented by membrane prices by negotiating bulk discounts or long term partnerships
- If possible, sign long term contracts with both buyers and power suppliers

Summary and Conclusions

Previous chapters have introduced the reader to the EMAR process and have touched on its thermodynamics, its mass and heat transport, and its design. This final chapter frames this work in an economics context in order to establish (1) the costs associated with carbon dioxide removal via the EMAR process and (2) potential markets for the EMAR process.

We see that the two major costs drivers for the bill of materials in the EMAR process are membrane area, which is a function of current density, and mass of copper required, which is a function of switching time (the time elapsed before an anode must be regenerated). The cost of materials model presented here was employed by

Wang and Gençer (to be presented in a forthcoming publication). In a summary of this work, it is shown that the total cost per metric ton of CO_2 avoided would likely run between \$60 and \$75, which is slightly more expensive than advanced thermal amine processes. Further, we see that this cost is driven by a few key factors (most of which have been covered in this thesis), namely: membrane costs, desorption pressure, copper loading shift, desorption temperature, and applied overpotential.

With costs in hand, we examine three broad markets for EMAR. (1) Sale of carbon dioxide into enhanced oil recovery (EOR) is rejected, because of the expectation that more novel thermal amine approaches will be more economical in traditional capture scenarios and naturally occurring carbon dioxide is likely less expensive than that captured from anthropogenic sources. (2) Emissions mitigation while potentially promising especially in concert with sales into EOR, is not yet viable given most current carbon prices and advanced thermal amine's potentially more dominate cost position. (3) Carbon dioxide separation as a service, however, is shown to be attractive when applied to the treatment of sour natural gas.

Finally, we see that should EMAR wish to compete in the natural gas treatment market, it will have two key advantages which make this market potentially attractive: (1) the ability to easily go from off-line to on-line (and vice versa) in order to take advantage of process or market variation and (2) a plug-and-play system design which does not require an intrusive boiler. As seen in the summary above, this is a market characterized by buyers (natural gas producers/suppliers) that have a low concentration and a regularly subjected to price variation, strong competition or threat of substitutes that may be mitigated through targeted project execution, and suppliers who's influence ranges from marginal to vitally important. It is therefore important to EMAR's success that it compete on greenfield projects, where thermal amine or other substitutes do not/cannot compete, and enter into long term contracts or partnerships with natural gas producers, membrane producers, and power suppliers.

This economic analysis brings into sharp relief that which was discussed in Chapter 3 ("EMAR Thermodynamics"). Namely, the three stage process employing anodic absorption, but decoupling cathodic absorbent activation and absorption of carbon dioxide, may be significantly improved though the use of a cathodic absorber. The above analysis portrays EMAR in its current state as potentially competitive in niche markets. This is largely driven by costs, which if improved by roughly 10%, would significantly change EMAR's competitive position. This is within the realm of possibilities for a two-stage EMAR process. EMAR's applicability and viability in more broad markets then may be significantly improved by incorporating such a cathodic absorber.

THIS PAGE INTENTIONALLY LEFT BLANK

Bibliography

[1] Michael C. Stern. *Electrochemically-Mediated Amine Regeneration for Carbon Dioxide Separations*. PhD thesis, Massachusetts Institute of Technology, February 2014.

[2] Aly O. Eltayeb. *Analysis and Design of Electrochemically-Mediated Carbon Dioxide Separation*. PhD thesis, Massachusetts Institute of Technology, Cambridge, Massachusetts, USA, June 2017.

[3] Pieter Tans and Ralph Keeling. ESRL Global Monitoring Division - Global Greenhouse Gas Reference Network. `https://www.esrl.noaa.gov/gmd/ccgg/trends/data.html`, April 2017.

[4] Shaun A. Marcott, Jeremy D. Shakun, Peter U. Clark, and Alan C. Mix. A Reconstruction of Regional and Global Temperature for the Past 11,300 Years. *Science*, 339(6124):1198–1201, March 2013.

[5] Susan Solomon, Gian-Kasper Plattner, Reto Knutti, and Pierre Friedlingstein. Irreversible climate change due to carbon dioxide emissions. *Proceedings of the National Academy of Sciences*, 106(6):1704–1709, October 2009.

[6] Naomi Oreskes. The Scientific Consensus on Climate Change. *Science*, 306(5702):1686–1686, December 2004.

[7] National Academy of Sciences. *Climate Change: Evidence and Causes*. February 2014.

[8] Lori Perkins, Gavin A. Schmidt, Robert B. Schmunk, Reto A. Ruedy, Patrick Lynch, Michèlle Handleman, Leslie McCarthy, and Matthew R. Radcliff. SVS:

Five-Year Global Temperature Anomalies from 1880 to 2015. `https://svs.gsfc.nasa.gov/4419`, January 2016.

[9] U.S. EPA. Inventory of U.S. Greenhouse Gas Emissions and Sinks: 1990-2014, April 2016.

[10] B Metz, O. R. Davidson, P. R. Bosch, and L. A. Meyer, editors. *Contribution of Working Group III to the Fourth Assessment Report of the Intergovernmental Panel on Climate Change, 2007.* Cambridge University Press, Cambridge, United Kingdom and New York, NY, USA, 2007.

[11] National Research Council. *America's Climate Choices.* May 2011.

[12] International Energy Agency. Energy Technology Perspectives 2010: Scenarios and Strategies to 2050. Technical report, 2010.

[13] U.S Energy Information Adminstration. Annual Energy Outlook 2017 with projections to 2050. Technical report, 2017.

[14] Global CCS Institute. Accelerating the Uptake of CCS: Industrial Use of Captured Carbon Dioxide, March 2011.

[15] Matthias Finkenrath, Julian Smith, and Dennis Volk. CCS Retrofit: Analysis of the Globally Installed Coal-Fired Power Plant Fleet. Technical report, International Energy Agency, 2012.

[16] O. R. Ganiev, R. F. Ganiev, and L. E. Ukrainsky. *Enhanced Oil Recovery: Resonance Macro- and Micro-Mechanics of Petroleum Reservoirs.* John Wiley & Sons, Inc., Hoboken, NJ, USA, December 2016.

[17] M. Mercedes Maroto-Valer, editor. *Carbon Dioxide (CO2) Storage and Utilisation.* Number Vol. 2 in Developments and innovation in carbon dioxide (CO2) capture and storage technology. CRC Press [u.a.], Boca Raton, Fla., 2010. OCLC: 846386237.

[18] Jennifer Wilcox. *Carbon Capture.* Springer, New York, 2012.

[19] B. J. P. Buhre, L. K. Elliott, C. D. Sheng, R. P. Gupta, and T. F. Wall. Oxy-fuel combustion technology for coal-fired power generation. *Progress in Energy and Combustion Science*, 31(4):283–307, January 2005.

[20] Gary T. Rochelle. Amine Scrubbing for CO2 Capture. *Science*, 325(5948):1652–1654, September 2009.

[21] E. S. Kikkinides, R. T. Yang, and S. H. Cho. Concentration and recovery of carbon dioxide from flue gas by pressure swing adsorption. *Industrial & Engineering Chemistry Research*, 32(11):2714–2720, November 1993.

[22] Burcu Gurkan, Fritz Simeon, and T. Alan Hatton. Quinone Reduction in Ionic Liquids for Electrochemical CO2 Separation. *ACS Sustainable Chemistry & Engineering*, 3(7):1394–1405, July 2015.

[23] Jihyun An and Nathaniel L. Rosi. Tuning MOF CO2 Adsorption Properties via Cation Exchange. *Journal of the American Chemical Society*, 132(16):5578–5579, April 2010.

[24] Douglas Aaron and Costas Tsouris. Separation of CO2 from Flue Gas: A Review. *Separation Science and Technology*, 40(1-3):321–348, January 2005.

[25] Lloyd M. Robeson. The upper bound revisited. *Journal of Membrane Science*, 320(1):390–400, July 2008.

[26] L. B. Gregory and W. G. Scharmann. Carbon Dioxide Scrubbing by Amine Solutions. *Industrial & Engineering Chemistry*, 29(5):514–519, May 1937.

[27] Michael C. Stern, Fritz Simeon, Howard Herzog, and T. Alan Hatton. Post-combustion carbon dioxide capture using electrochemically mediated amine regeneration. *Energy & Environmental Science*, 6(8):2505–2517, July 2013.

[28] Paul Feron, editor. *Absorption-Based Post Combustion Capture of Carbon Dioxide*. Elsevier, Waltham, MA, 1st edition edition, 2016.

[29] Yu-Jeng Lin, Eric Chen, and Gary T. Rochelle. Pilot plant test of the advanced flash stripper for CO2 capture. *Faraday Discussions*, 192(0):37–58, October 2016.

[30] Matthew E. Boot-Handford, Juan C. Abanades, Edward J. Anthony, Martin J. Blunt, Stefano Brandani, Niall Mac Dowell, José R. Fernández, Maria-Chiara Ferrari, Robert Gross, Jason P. Hallett, R. Stuart Haszeldine, Philip Heptonstall, Anders Lyngfelt, Zen Makuch, Enzo Mangano, Richard T. J. Porter, Mohamed Pourkashanian, Gary T. Rochelle, Nilay Shah, Joseph G. Yao, and Paul S. Fennell. Carbon capture and storage update. *Energy Environ. Sci.*, 7(1):130–189, 2014.

[31] Patricia A. Terry, H. Jeremy Walis, Richard D. Noble, and Carl A. Koval. Electrochemically modulated complexation process for gas removal and concentration. *AIChE Journal*, 41(12):2556–2564, December 1995.

[32] Patricia A. Terry, Richard D. Noble, Daniel Swanson, and Carl A. Koval. Electrochemically modulated complexation process for ethylene/ethane separation. *AIChE Journal*, 43(7):1709–1716, July 1997.

[33] W. L. Bell, A. Miedaner, J. C. Smart, D. L. DuBois, and C. E. Verostko. Synthesis and Evaluation of Electroactive CO2 Carriers. SAE Technical Paper 881078, SAE Technical Paper, Warrendale, PA, July 1988.

[34] Paul Scovazzo, Joe Poshusta, Dan DuBois, Carl Koval, and Richard Noble. Electrochemical Separation and Concentration of <1% Carbon Dioxide from Nitrogen. *Journal of The Electrochemical Society*, 150(5):D91–D98, January 2003.

[35] A. E. Sherwood and J. M. Prausnitz. The heat of solution of gases at high pressure. *AIChE Journal*, 8(4):519–521, September 1962.

[36] Peter Linstrom and W.G. Mallard. *NIST Chemistry WebBook, NIST Standard Reference Database 69.* National Institute of Standards and Technology, 1997.

[37] Kakusaburo Onda, Eizo Sada, Takeshi Kobayashi, Shigeharu Kito, and Kunimitsu Ito. Salting-Out Parameters of Gas Solubility in Aqueous Salt Solutions. *Journal of Chemical Engineering of Japan*, 3(1):18–24, 1970.

[38] Shan Zhou, Xi Chen, Thu Nguyen, Alexander K. Voice, and Gary T. Rochelle. Aqueous Ethylenediamine for CO2 Capture. *ChemSusChem*, 3(8):913–918, August 2010.

[39] William M. Deen. *Analysis of Transport Phenomena.* Topics in chemical engineering. Oxford University Press, New York, 2nd ed edition, 2012.

[40] S. M. Lindsay. *Introduction to Nanoscience.* Oxford [England] ; New York : Oxford University Press, 2010., 2010.

[41] Jonathan Law and Richard Rennie. Joule heating. *A Dictionary of Physics*, 2015.

[42] Bernhard Tjaden, Samuel J Cooper, Daniel JL Brett, Denis Kramer, and Paul R Shearing. On the origin and application of the Bruggeman correlation for analysing

transport phenomena in electrochemical systems. *Current Opinion in Chemical Engineering*, 12:44–51, May 2016.

[43] L. Fabbrizzi, P. Paoletti, and A. B. P. Lever. Relation between electronic spectra and heat of formation of some copper-polyamine complexes and the macrocyclic effect. *Inorganic Chemistry*, 15(7):1502–1506, July 1976.

[44] Michael C. Stern and T. Alan Hatton. Bench-scale demonstration of CO2 capture with electrochemically-mediated amine regeneration. *RSC Advances*, 4(12):5906–5914, January 2014.

[45] G. Kear, B. D. Barker, and F. C. Walsh. Electrochemical corrosion of unalloyed copper in chloride media—a critical review. *Corrosion Science*, 46(1):109–135, January 2004.

[46] Kevin S. Fisher, Katherine Searcy, Gary T. Rochelle, Sepideh Ziaii, and Craig Schubert. Advanced Amine Solvent Formulations and Process Integration for Near-Term CO2 Capture Success. Technical Report DOE/ER/84625-1 Final Report, Trimeric Corporation, June 2007.

[47] Industrial Carbon Dioxide Supply Crucial For EOR. https://www.aogr.com/magazine/editors-choice/industrial-co2-supply-crucial-for-eor.

[48] Matthew Wallace, Lessly Goudarzi, Kara Callahan, and Robert Wallace. A Review of the CO2 Pipeline Infrastructure in the U.S. Technical Report DOE/NETL-2014/1681, National Energy Technology Laboratory, April 2015.

[49] State and Trends of Carbon Pricing 2018. Technical report, World Bank Group, May 2018.

[50] finanzen net GmbH. CO2 European Emission Allowances Price. https://markets.businessinsider.com/commodities/co2-emissionsrechte.

[51] Jeff Tollefson. 'Flaring' wastes 3.5% of world's natural gas. *Nature News*.

[52] Christopher D. Elvidge, Mikhail Zhizhin, Kimberly Baugh, Feng-Chi Hsu, and Tilottama Ghosh. Methods for Global Survey of Natural Gas Flaring from Visible Infrared Imaging Radiometer Suite Data. *Energies*, 9(1):14, January 2016.

[53] W. F. J. Burgers, P. S. Northrop, H. S. Kheshgi, and J. A. Valencia. Worldwide development potential for sour gas. *Energy Procedia*, 4:2178–2184, January 2011.

[54] Michael E Porter. The Five Competitive Forces That Shape Strategy. *harvard business review*, page 16, 2008.

[55] U. S. Government Accountability Office. Energy Markets: Effects of Mergers and Market Concentration in the U.S. Petroleum Industry. (GAO-04-96), May 2004.

Appendix A

EMAR 8.x Engineering Drawings

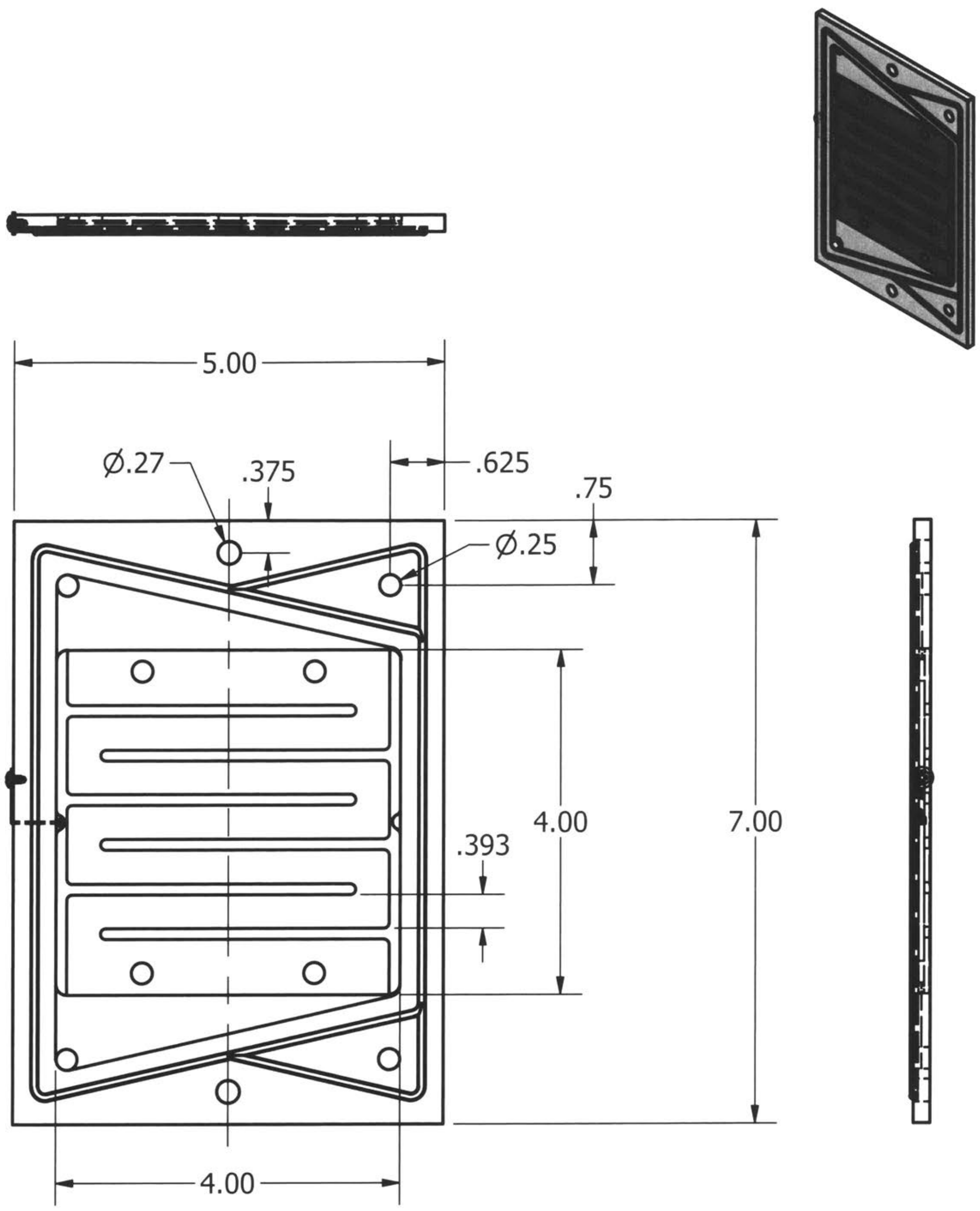

DRAWN Ryan Shaw	8/2/2017	
CHECKED		TITLE
QA		EMAR 8.1 Electrode Plate
MFG		
APPROVED		
		SIZE A · DWG NO · REV
		SCALE 1 / 2 · SHEET 1 OF 1

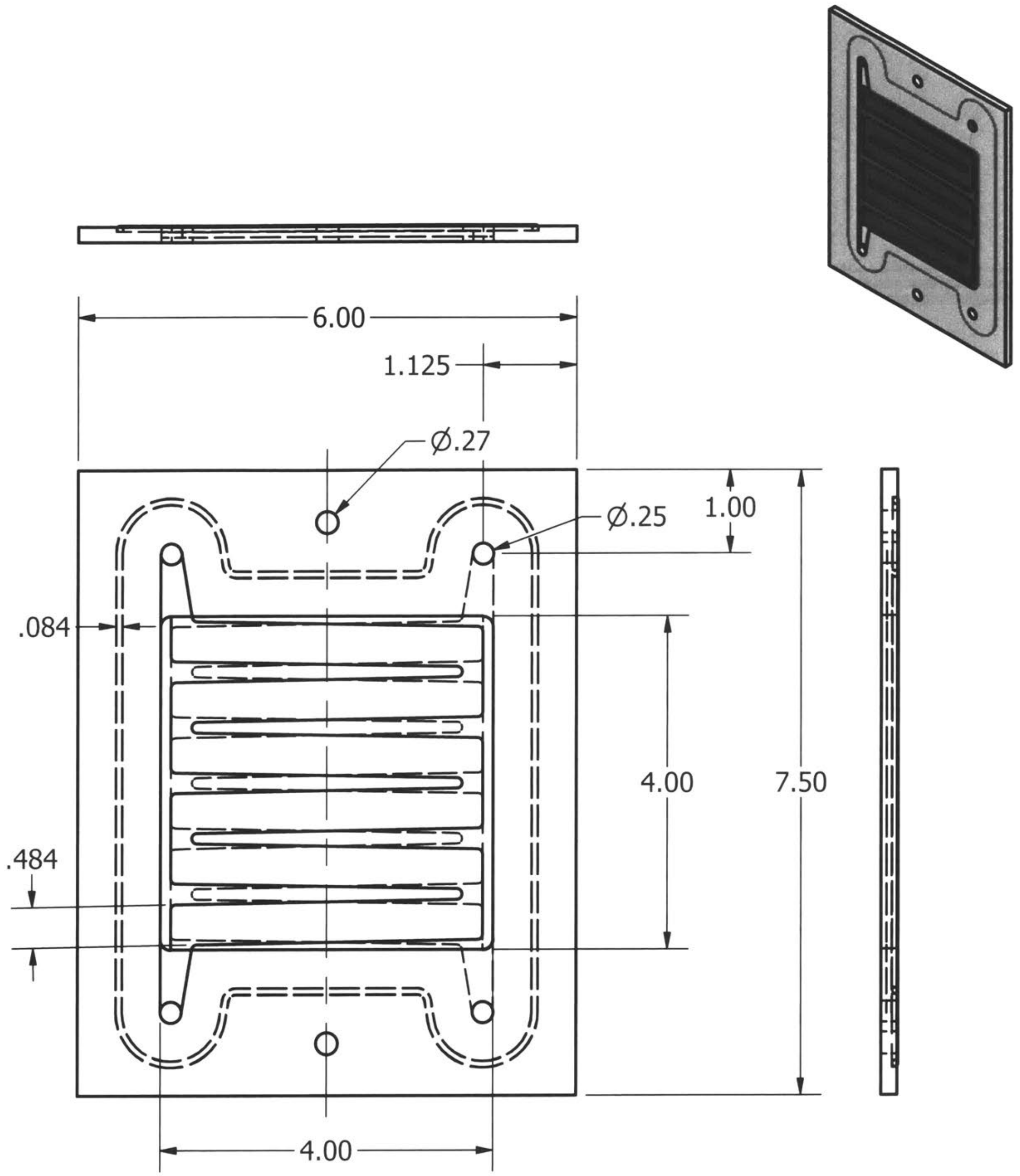

DRAWN Ryan Shaw	8/2/2017			
CHECKED		TITLE EMAR 8.2 Electrode Plate		
QA				
MFG				
APPROVED		SIZE A	DWG NO	REV
		SCALE 1 / 2		SHEET 1 OF 1

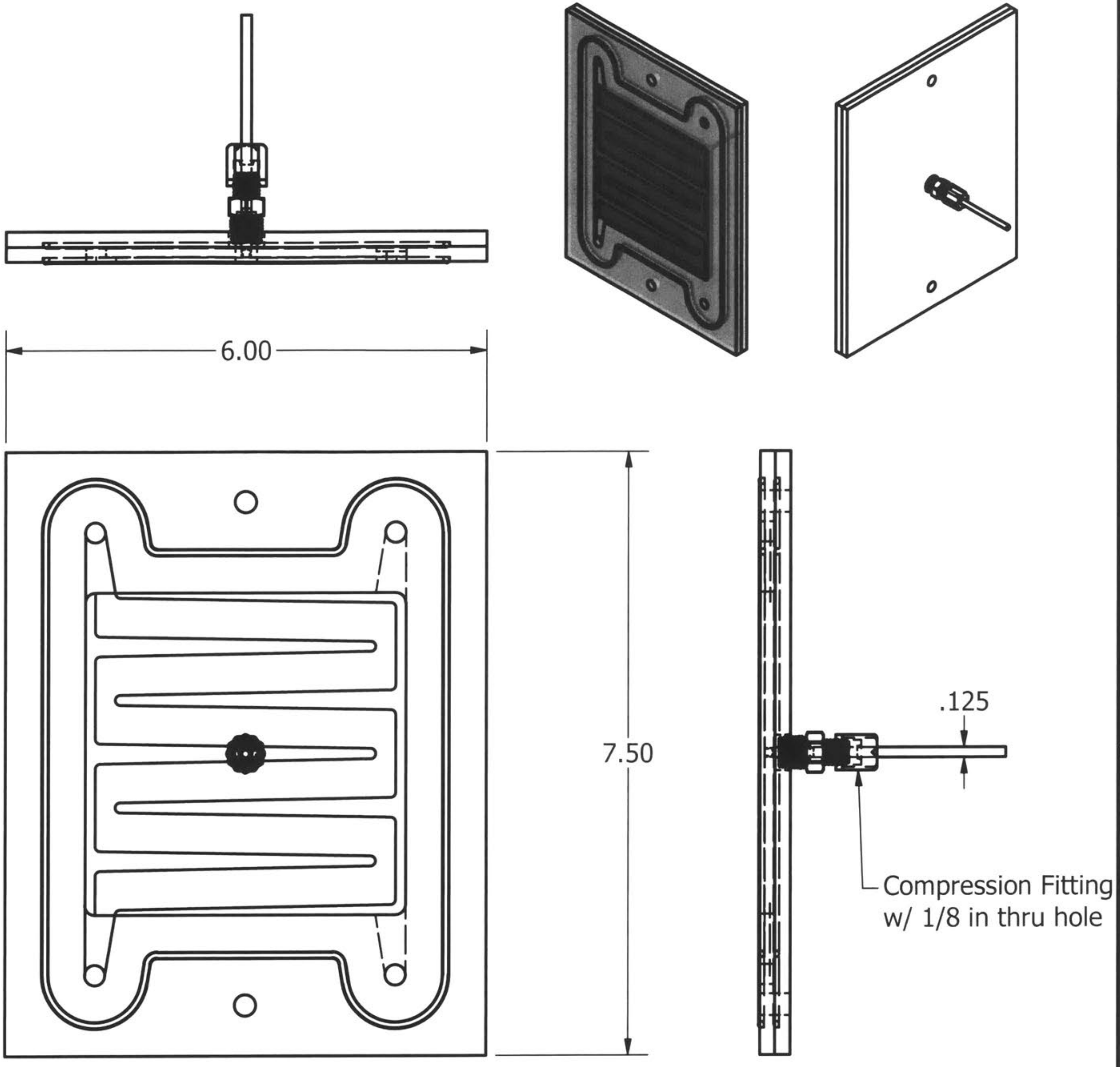

DRAWN Ryan Shaw	8/4/2017
CHECKED	
QA	
MFG	
APPROVED	

TITLE

Electrode End Plate Assembly

SIZE A	DWG NO	REV
SCALE 1 / 2		SHEET 1 OF 1

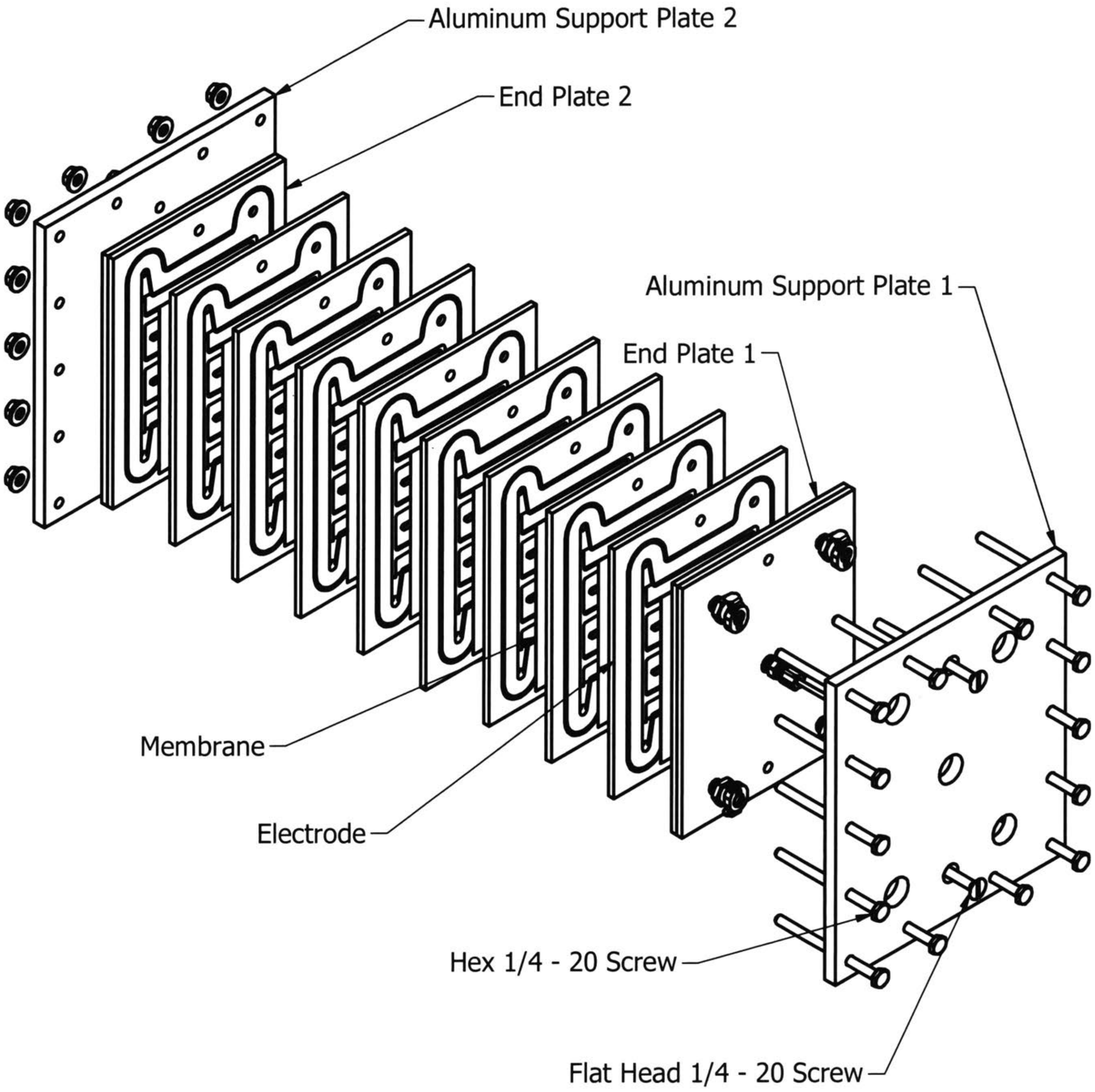

DRAWN Ryan Shaw	8/2/2017
CHECKED	
QA	
MFG	
APPROVED	

TITLE

EMAR 8.2 Stack Assembly

SIZE A

DWG NO

REV

SCALE 1 / 4

SHEET 1 OF 1

THIS PAGE INTENTIONALLY LEFT BLANK

Appendix B

Open Circuit Potential Derivations

EMCS Inactive Absorbent in Solution

Open Circuit Potential

Electrochemical	$\mathrm{A(aq) + me^- \rightleftharpoons A^{m-}(aq)}$
	$E = E^\circ - \frac{RT}{mF} \ln\left(\frac{C_{A^{m-}}}{C_A}\right)$
Homogeneous	$\mathrm{A^{m-}(aq) + mCO_2(g) \rightleftharpoons A(CO_2)_m{}^{m-}(aq)}$
	$K_{CO_2} = \frac{C_{A(CO_2)_m^{m-}}}{C_{A^{m-}}} \left(\frac{P_0}{P_{CO_2}}\right)^m$
Overall	$\mathrm{A(aq) + me^- + mCO_2(g) \rightleftharpoons A(CO_2)_m{}^{m-}(aq)}$

$$A_0 = C_A + C_{A^{m-}} + C_{A(CO_2)_m^{m-}}$$

$$x_{A'} = \frac{C_{A^{m-}} + C_{A(CO_2)_m^{m-}}}{A_0} \quad .$$

$$\begin{aligned}
C_A &= A_0 - \left(C_{A^{m-}} + C_{A(CO_2)_m^{m-}}\right) \\
&= A_0 - x_{A'} A_0 \\
&= \left(1 - x_{A'}\right) A_0
\end{aligned}$$

$$A_0 - C_A = x_{A'} A_0$$

$$\begin{aligned}
K_{CO_2} &= \frac{C_{A(CO_2)_m^{m-}}}{C_{A^{m-}}} \left(\frac{P_0}{P_{CO_2}}\right)^m \\
&= \frac{A_0 - C_A - C_{A^{m-}}}{C_{A^{m-}}} \left(\frac{P_0}{P_{CO_2}}\right)^m \\
&= \left(\frac{A_0 - C_A}{C_{A^{m-}}} - 1\right) \left(\frac{P_0}{P_{CO_2}}\right)^m \\
&= \left(\frac{x_{A'} A_0}{C_{A^{m-}}} - 1\right) \left(\frac{P_0}{P_{CO_2}}\right)^m
\end{aligned}$$

$$1 + K_{CO_2} \left(\frac{P_{CO_2}}{P_0}\right)^m = \frac{x_{A'} A_0}{C_{A^{m-}}}$$

$$C_{A^{m-}} = \frac{x_{A'} A_0}{1 + K_{CO_2} \left(\frac{P_{CO_2}}{P_0}\right)^m}\ .$$

$$
\begin{aligned}
E &= E^{\circ} - \frac{RT}{mF} \ln\left(\frac{C_{A^{m-}}}{C_A}\right) \\
&= E^{\circ} - \frac{RT}{mF} \ln\left(\left(\frac{x_{A'} A_0}{C_A}\right) \frac{1}{1 + K_{CO_2}\left(\frac{P_{CO_2}}{P_0}\right)^m}\right) \\
&= E^{\circ} - \frac{RT}{mF} \ln\left(\left(\frac{x_{A'} A_0}{(1 - x_{A'})\, A_0}\right) \frac{1}{1 + K_{CO_2}\left(\frac{P_{CO_2}}{P_0}\right)^m}\right) \\
&= E^{\circ} - \frac{RT}{mF} \ln\left(\left(\frac{x_{A'}}{1 - x_{A'}}\right) \frac{1}{1 + K_{CO_2}\left(\frac{P_{CO_2}}{P_0}\right)^m}\right) \\
&= E^{\circ} - \frac{RT}{mF} \left[\ln\left(\frac{x_{A'}}{1 - x_{A'}}\right) - \ln\left(1 + K_{CO_2}\left(\frac{P_{CO_2}}{P_0}\right)^m\right)\right]
\end{aligned}
$$

$$
\begin{aligned}
E - E_0 &= E - E|_{P_{CO_2}=0} \\
&= \left(E^{\circ} - \frac{RT}{mF}\left[\ln\left(\frac{x_{A'}}{1 - x_{A'}}\right) - \ln\left(1 + K_{CO_2}\left(\frac{P_{CO_2}}{P_0}\right)^m\right)\right]\right) \\
&\quad - \left(E^{\circ} - \frac{RT}{mF}\left[\ln\left(\frac{x_{A'}}{1 - x_{A'}}\right)\right]\right) \\
&= E^{\circ} + \frac{RT}{mF} \ln\left(1 + K_{CO_2}\left(\frac{P_{CO_2}}{P_0}\right)^m\right)
\end{aligned}
$$

CO_2 Mass Balance

$$
A_0 = C_A + C_{A^{m-}} + C_{A(CO_2)_m^{m-}}
$$

$$
x_{A'} = \frac{C_{A^{m-}} + C_{A(CO_2)_m^{m-}}}{A_0}
$$

$$
CO_{2,0} = C_{CO_2} + mC_{A(CO_2)_m^{m-}}
$$

$$P_{CO_2} = \frac{C_{CO_2}}{k_{h,CO_2}}$$

$$x_{CO_{2,0}} = \frac{CO_{2,0}}{mA_0}$$

$$\begin{aligned} C_A &= A_0 - \left(C_{A^{m-}} + C_{A(CO_2)_m^{m-}}\right) \\ &= A_0 - x_{A'}A_0 \\ &= \left(1 - x_{A'}\right)A_0 \end{aligned}$$

$$A_0 - C_A = x_{A'}A_0$$

$$\begin{aligned} K_{CO_2} &= \frac{C_{A(CO_2)_m^{m-}}}{C_{A^{m-}}}\left(\frac{P_0}{P_{CO_2}}\right)^m \\ &= \left(\frac{C_{A(CO_2)_m^{m-}}}{A_0 - C_A - C_{A(CO_2)_m^{m-}}}\right)\left(\frac{P_0}{P_{CO_2}}\right)^m \\ &= \left(\frac{C_{A(CO_2)_m^{m-}}}{x_{A'}A_0 - C_{A(CO_2)_m^{m-}}}\right)\left(\frac{P_0}{P_{CO_2}}\right)^m \end{aligned}$$

$$K_{CO_2}\left(x_{A'}A_0 - C_{A(CO_2)_m^{m-}}\right) = C_{A(CO_2)_m^{m-}}\left(\frac{P_0}{P_{CO_2}}\right)^m$$

$$K_{CO_2}x_{A'}A_0 = C_{A(CO_2)_m^{m-}}\left(K_{CO_2} + \left(\frac{P_0}{P_{CO_2}}\right)^m\right)$$

$$\begin{aligned} C_{A(CO_2)_m^{m-}} &= x_{A'}A_0\left(\frac{K_{CO_2}}{K_{CO_2} + \left(\frac{P_0}{P_{CO_2}}\right)^m}\right) \\ &= x_{A'}A_0\left(\frac{K_{CO_2}\left(\frac{P_{CO_2}}{P_0}\right)^m}{1 + K_{CO_2}\left(\frac{P_{CO_2}}{P_0}\right)^m}\right) \end{aligned}$$

$$
\begin{aligned}
CO_{2,0} &= C_{CO_2} + mC_{A(CO_2)_m^{m-}} \\
&= m x_{A'} A_0 \frac{K_{CO_2}\left(\frac{P_{CO_2}}{P_0}\right)^m}{1 + K_{CO_2}\left(\frac{P_{CO_2}}{P_0}\right)^m} + k_{h,CO_2} P_{CO_2}
\end{aligned}
$$

$$
x_{CO_{2,0}} = x_{A'} \frac{K_{CO_2}\left(\frac{P_{CO_2}}{P_0}\right)^m}{1 + K_{CO_2}\left(\frac{P_{CO_2}}{P_0}\right)^m} + \frac{k_{h,CO_2} P_{CO_2}}{m A_0}
$$

EMCS Solid Inactive Absorbent

Open Circuit Potential

Electrochemical	$\mathrm{A(s) + me^- \rightleftharpoons A^{m-}(aq)}$
	$E = E^\circ - \frac{RT}{mF}\ln\left(\frac{C_{A^{m-}}}{C_0}\right)$
Homogeneous	$\mathrm{A^{m-}(aq) + mCO_2(g) \rightleftharpoons A(CO_2)_m{}^{m-}(aq)}$
	$K_{CO_2} = \frac{C_{A(CO_2)_m^{m-}}}{C_{A^{m-}}}\left(\frac{P_0}{P_{CO_2}}\right)^m$
Overall	$\mathrm{A(s) + me^- + mCO_2(g) \rightleftharpoons A(CO_2)_m{}^{m-}(aq)}$

$$
A_0 = C_{A^{m-}} + C_{A(CO_2)_m^{m-}}
$$

$$
\begin{aligned}
K_{CO_2} &= \frac{C_{A(CO_2)_m^{m-}}}{C_{A^{m-}}}\left(\frac{P_0}{P_{CO_2}}\right)^m \\
&= \frac{A_0 - C_{A^{m-}}}{C_{A^{m-}}}\left(\frac{P_0}{P_{CO_2}}\right)^m \\
&= \left(\frac{A_0}{C_{A^{m-}}} - 1\right)\left(\frac{P_0}{P_{CO_2}}\right)^m
\end{aligned}
$$

$$
1 + K_{CO_2}\left(\frac{P_{CO_2}}{P_0}\right)^m = \frac{A_0}{C_{A^{m-}}}
$$

$$C_{A^{m-}} = \frac{A_0}{1 + K_{CO_2}\left(\frac{P_{CO_2}}{P_0}\right)^m}$$

$$\begin{aligned} E &= E^\circ - \frac{RT}{mF}\ln\left(\frac{C_{A^{m-}}}{C_0}\right) \\ &= E^\circ - \frac{RT}{mF}\ln\left(\left(\frac{A_0}{C_0}\right)\frac{1}{1 + K_{CO_2}\left(\frac{P_{CO_2}}{P_0}\right)^m}\right) \\ &= E^\circ + \frac{RT}{mF}\left[\ln\left(1 + K_{CO_2}\left(\frac{P_{CO_2}}{P_0}\right)^m\right) - \ln\left(\frac{A_0}{C_0}\right)\right] \end{aligned}$$

$$\begin{aligned} E - E_0 &= E - E|_{P_{CO_2}=0} \\ &= \left(E^\circ + \frac{RT}{mF}\left[\ln\left(1 + K_{CO_2}\left(\frac{P_{CO_2}}{P_0}\right)^m\right) - \ln\left(\frac{A_0}{C_0}\right)\right]\right) \\ &\quad - \left(E^\circ - \frac{RT}{mF}\ln\left(\frac{A_0}{C_0}\right)\right) \\ &= E^\circ + \frac{RT}{mF}\ln\left(1 + K_{CO_2}\left(\frac{P_{CO_2}}{P_0}\right)^m\right) \end{aligned}$$

$\mathbf{CO_2}$ Mass Balance

$$A_0 = C_{A^{m-}} + C_{A(CO_2)_m^{m-}}$$

$$CO_{2,0} = C_{CO_2} + mC_{A(CO_2)_m^{m-}}$$

$$P_{CO_2} = \frac{C_{CO_2}}{k_{h,CO_2}}$$

$$x_{CO_{2,0}} = \frac{CO_{2,0}}{mC_0}$$

$$
\begin{aligned}
K_{CO_2} &= \frac{C_{A(CO_2)_m^{m()-}}}{C_{A^{m-}}} \left(\frac{P_0}{P_{CO_2}} \right)^m \\
&= \frac{C_{A(CO_2)_m^{m-}}}{A_0 - C_{A(CO_2)_m^{m-}}} \left(\frac{P_0}{P_{CO_2}} \right)^m
\end{aligned}
$$

$$
\left(A_0 - C_{A(CO_2)_m^{m-}} \right) K_{CO_2} \left(\frac{P_{CO_2}}{P_0} \right)^m = C_{A(CO_2)_m^{m-}}
$$

$$
A_0 K_{CO_2} \left(\frac{P_{CO_2}}{P_0} \right)^m = \left(1 + K_{CO_2} \left(\frac{P_{CO_2}}{P_0} \right)^m \right) C_{A(CO_2)_m^{m-}}
$$

$$
C_{A(CO_2)_m^{m-}} = A_0 \frac{K_{CO_2} \left(\frac{P_{CO_2}}{P_0} \right)^m}{1 + K_{CO_2} \left(\frac{P_{CO_2}}{P_0} \right)^m}
$$

$$
\begin{aligned}
CO_{2,0} &= C_{CO_2} + mC_{A(CO_2)_m^{m-}} \\
&= mA_0 \frac{K_{CO_2} \left(\frac{P_{CO_2}}{P_0} \right)^m}{1 + K_{CO_2} \left(\frac{P_{CO_2}}{P_0} \right)^m} + k_{h,CO_2} P_{CO_2}
\end{aligned}
$$

$$
x_{CO_{2,0}} = \left(\frac{A_0}{C_0} \right) \frac{K_{CO_2} \left(\frac{P_{CO_2}}{P_0} \right)^m}{1 + K_{CO_2} \left(\frac{P_{CO_2}}{P_0} \right)^m} + \frac{k_{h,CO_2} P_{CO_2}}{mC_0}
$$

EMCCS Inactive Blocker in Solution

Open Circuit Potential

Electrochemical	$\mathrm{B^{n+} + ne^- \rightleftharpoons B}$
	$E = E^{\circ} - \frac{RT}{nF} \ln\left(\frac{C_B}{C_{B^{n+}}}\right)$
Homogeneous	$\mathrm{A + mCO_2 \rightleftharpoons A(CO_2)_m}$
	$K_{CO_2} = \frac{C_{A(CO_2)_m}}{C_A}\left(\frac{P_0}{P_{CO_2}}\right)^m$
Homogeneous	$\mathrm{\frac{n}{m}A + B^{n+} \rightleftharpoons B(A)_{n/m}}$
	$\beta = \frac{C_{B(A)_{n/m}} C_0^{n/m}}{C_A^{n/m} C_{B^{n+}}}$
Overall	$\mathrm{B(A)_{n/m} + ne^- + nCO_2 \rightleftharpoons B + \frac{n}{m}A(CO_2)_m}$

$$A_0 = C_A + C_{A(CO_2)_m} + \frac{n}{m} C_{B(A)_{n/m}}$$

$$B_0 = C_B + C_{B^{n+}} + C_{B(A)_{n/m}} \approx C_B + C_{B(A)_{n/m}}$$

$$x_B = \frac{n C_{B(A)_{n/m}}}{m A_0}$$

$$C_{B(A)_{n/m}} = \frac{m}{n} x_B A_0$$

$$x_B = \frac{n\left(B_0 - C_B\right)}{m A_0} \Rightarrow C_B = B_0 - \frac{m}{n} x_B A_0$$

$$\begin{aligned}
K_{CO_2} &= \frac{C_{A(CO_2)_m}}{C_A}\left(\frac{P_0}{P_{CO_2}}\right)^m \\
&= \frac{A_0 - \left(C_A + \frac{n}{m}C_{B(A)_{n/m}}\right)}{C_A}\left(\frac{P_0}{P_{CO_2}}\right)^m \\
&= \left(\frac{A_0 - \frac{n}{m}C_{B(A)_{n/m}}}{C_A} - 1\right)\left(\frac{P_0}{P_{CO_2}}\right)^m \\
&= \left(\frac{A_0 - x_B A_0}{C_A} - 1\right)\left(\frac{P_0}{P_{CO_2}}\right)^m \\
&= \left(\frac{(1 - x_B)\,A_0}{C_A} - 1\right)\left(\frac{P_0}{P_{CO_2}}\right)^m
\end{aligned}$$

$$1 + K_{CO_2}\left(\frac{P_{CO_2}}{P_0}\right)^m = \frac{(1 - x_B)\,A_0}{C_A}$$

$$C_A = \frac{(1 - x_B)\,A_0}{1 + K_{CO_2}\left(\frac{P_{CO_2}}{P_0}\right)^m}$$

$$
\begin{aligned}
E &= E^\circ - \frac{RT}{nF}\ln\left(\frac{C_B}{C_{B^{n+}}}\right)\\
&= E^\circ - \frac{RT}{nF}\ln\left(\frac{\beta C_A^{n/m} C_B}{C_{B(A)_{n/m}} C_0^{n/m}}\right)\\
&= E^\circ - \frac{RT}{nF}\ln\left(\frac{\beta C_B}{C_{B(A)_{n/m}}}\left[\frac{C_A}{C_0}\right]^{n/m}\right)\\
&= E^\circ - \frac{RT}{nF}\ln\left(\frac{\beta\left(B_0 - \frac{m}{n}x_B A_0\right)}{\frac{m}{n}x_B A_0}\left[\frac{(1-x_B)\frac{A_0}{C_0}}{1+K_{CO_2}\left(\frac{P_{CO_2}}{P_0}\right)^m}\right]^{n/m}\right)\\
&= E^\circ - \frac{RT}{nF}\ln\left(\beta\left(\frac{nB_0}{mx_B A_0}-1\right)\left[\left(\frac{A_0}{C_0}\right)\frac{1-x_B}{1+K_{CO_2}\left(\frac{P_{CO_2}}{P_0}\right)^m}\right]^{n/m}\right)\\
&= E^\circ - \frac{RT}{nF}\left[\ln\left(\frac{nB_0}{mx_B A_0}-1\right)+\ln\left(\beta\left[\left(\frac{A_0}{C_0}\right)\frac{1-x_B}{1+K_{CO_2}\left(\frac{P_{CO_2}}{P_0}\right)^m}\right]^{n/m}\right)\right]
\end{aligned}
$$

$$
\begin{aligned}
E - E_0 &= E - \left.E\right|_{P_{CO_2}=0}\\
&= \left(E^\circ - \frac{RT}{nF}\left[\ln\left(\frac{nB_0}{mx_B A_0}-1\right)+\ln\left(\frac{\beta\left(\frac{A_0}{C_0}\right)^{n/m}(1-x_B)^{n/m}}{\left(1+K_{CO_2}\left(\frac{P_{CO_2}}{P_0}\right)^m\right)^{n/m}}\right)\right]\right)\\
&\quad - \left(E^\circ - \frac{RT}{nF}\left[\ln\left(\frac{nB_0}{mx_B A_0}-1\right)+\ln\left(\beta\left(\frac{A_0}{C_0}\right)^{n/m}(1-x_B)^{n/m}\right)\right]\right)\\
&= \frac{RT}{nF}\ln\left(\left(1+K_{CO_2}\left(\frac{P_{CO_2}}{P_0}\right)^m\right)^{n/m}\right)\\
&= \frac{RT}{mF}\ln\left(1+K_{CO_2}\left(\frac{P_{CO_2}}{P_0}\right)^m\right)
\end{aligned}
$$

$\mathbf{CO_2}$ Mass Balance

$$A_0 = C_A + C_{A(CO_2)_m} + \frac{n}{m} C_{B(A)_{n/m}}$$

$$B_0 = C_B + C_{B^{n+}} + C_{B(A)_{n/m}} \approx C_B + C_{B(A)_{n/m}}$$

$$x_B = \frac{nC_{B(A)_{n/m}}}{mA_0}$$

$$CO_{2,0} = C_{CO_2} + mC_{A(CO_2)_m}$$

$$P_{CO_2} = \frac{C_{CO_2}}{k_{h,CO_2}}$$

$$x_{CO_{2,0}} = \frac{CO_{2,0}}{mA_0}$$

$$\begin{aligned} K_{CO_2} &= \frac{C_{A(CO_2)_m}}{C_A} \left(\frac{P_0}{P_{CO_2}} \right)^m \\ &= \frac{C_{A(CO_2)_m}}{A_0 - \left(C_{A(CO_2)_m} + \frac{n}{m} C_{B(A)_{n/m}} \right)} \left(\frac{P_0}{P_{CO_2}} \right)^m \\ &= \frac{C_{A(CO_2)_m}}{A_0 - \left(C_{A(CO_2)_m} + x_B A_0 \right)} \left(\frac{P_0}{P_{CO_2}} \right)^m \\ &= \frac{C_{A(CO_2)_m}}{(1 - x_B) A_0 - C_{A(CO_2)_m}} \left(\frac{P_0}{P_{CO_2}} \right)^m \end{aligned}$$

$$\left((1 - x_B) A_0 - C_{A(CO_2)_m} \right) K_{CO_2} \left(\frac{P_{CO_2}}{P_0} \right)^m = C_{A(CO_2)_m}$$

$$(1 - x_B) A_0 K_{CO_2} \left(\frac{P_{CO_2}}{P_0} \right)^m = \left(1 + K_{CO_2} \left(\frac{P_{CO_2}}{P_0} \right)^m \right) C_{A(CO_2)_m}$$

$$C_{A(CO_2)_m} = (1 - x_B)\, A_0 \frac{K_{CO_2}\left(\frac{P_{CO_2}}{P_0}\right)^m}{1 + K_{CO_2}\left(\frac{P_{CO_2}}{P_0}\right)^m}$$

$$\begin{aligned} CO_{2,0} &= C_{CO_2} + mC_{A(CO_2)_m} \\ &= m\,(1 - x_B)\, A_0 \frac{K_{CO_2}\left(\frac{P_{CO_2}}{P_0}\right)^m}{1 + K_{CO_2}\left(\frac{P_{CO_2}}{P_0}\right)^m} + k_{h,CO_2} P_{CO_2} \end{aligned}$$

$$x_{CO_{2,0}} = (1 - x_B)\, \frac{K_{CO_2}\left(\frac{P_{CO_2}}{P_0}\right)^m}{1 + K_{CO_2}\left(\frac{P_{CO_2}}{P_0}\right)^m} + \frac{k_{h,CO_2} P_{CO_2}}{mA_0}$$

EMCCS Solid Inactive Blocker

Open Circuit Potential

Electrochemical	$\mathrm{B^{n+} + ne^- \rightleftharpoons B}$
	$E = E^\circ - \frac{RT}{nF} \ln\left(\frac{C_0}{C_{B^{n+}}}\right)$
Homogeneous	$\mathrm{A + mCO_2 \rightleftharpoons A(CO_2)_m}$
	$K_{CO_2} = \frac{C_{A(CO_2)_m}}{C_A}\left(\frac{P_0}{P_{CO_2}}\right)^m$
Homogeneous	$\mathrm{\frac{n}{m}A + B^{n+} \rightleftharpoons B(A)_{n/m}{}^{n+}}$
	$\beta = \frac{C_{C_{B(A)^{n+}_{n/m}}} C_0^{n/m}}{C_A^{n/m} C_{B^{n+}}}$
Overall	$\mathrm{B(A)_{n/m} + ne^- + nCO_2 \rightleftharpoons B + \frac{n}{m}A(CO_2)_m}$

$$A_0 = C_A + C_{A(CO_2)_m} + \frac{n}{m} C_{B(A)_{n/m}}$$

$$B_0 = C_{B^{n+}} + C_{B(A)^{n+}_{n/m}} \approx C_{B(A)^{n+}_{n/m}}$$

$$x_B = \frac{nC_{B(A)_{n/m}}}{mA_0} \approx \frac{nB_0}{mA_0}$$

$$\begin{aligned}
K_{CO_2} &= \frac{C_{A(CO_2)_m}}{C_A}\left(\frac{P_0}{P_{CO_2}}\right)^m \\
&= \frac{A_0 - \left(C_A + \frac{n}{m}C_{B(A)^{n+}_{n/m}}\right)}{C_A}\left(\frac{P_0}{P_{CO_2}}\right)^m \\
&= \left(\frac{A_0 - \frac{n}{m}C_{B(A)^{n+}_{n/m}}}{C_A} - 1\right)\left(\frac{P_0}{P_{CO_2}}\right)^m \\
&= \left(\frac{A_0 - \frac{n}{m}\left(B_0 - C_{B^{n+}}\right)}{C_A} - 1\right)\left(\frac{P_0}{P_{CO_2}}\right)^m \\
&= \left(\frac{A_0 - \frac{n}{m}B_0 + \frac{n}{m}C_{B^{n+}}}{C_A} - 1\right)\left(\frac{P_0}{P_{CO_2}}\right)^m
\end{aligned}$$

$$1 + K_{CO_2}\left(\frac{P_{CO_2}}{P_0}\right)^m = \frac{A_0 - \frac{n}{m}B_0 + \frac{n}{m}C_{B^{n+}}}{C_A}$$

$$C_A = \frac{A_0 - \frac{n}{m}B_0 + \frac{n}{m}C_{B^{n+}}}{1 + K_{CO_2}\left(\frac{P_{CO_2}}{P_0}\right)^m}$$

$$
\begin{aligned}
E &= E^\circ - \frac{RT}{nF}\ln\left(\frac{C_0}{C_{B^{n+}}}\right) \\
&= E^\circ - \frac{RT}{nF}\ln\left(\frac{C_A^{n/m}\beta}{C_{B(A)^{n+}_{n/m}}\,C_0^{n/m-1}}\right) \\
&= E^\circ - \frac{RT}{nF}\ln\left(\frac{C_0}{B_0}\,\frac{B_0 C_A^{n/m}\beta}{C_{B(A)^{n+}_{n/m}}\,C_0^{n/m}}\right) \\
&= E^\circ - \frac{RT}{nF}\ln\left(\frac{C_0}{B_0}\,\frac{\left(C_{B^{n+}} + C_{B(A)^{n+}_{n/m}}\right)C_A^{n/m}\beta}{C_{B(A)^{n+}_{n/m}}\,C_0^{n/m}}\right) \\
&= E^\circ - \frac{RT}{nF}\ln\left(\frac{C_0}{B_0}\left(\frac{C_{B^{n+}}C_A^{n/m}\beta}{C_{B(A)^{n+}_{n/m}}\,C_0^{n/m}} + \frac{C_A^{n/m}\beta}{C_0^{n/m}}\right)\right) \\
&= E^\circ - \frac{RT}{nF}\ln\left(\frac{C_0}{B_0}\left(\cancelto{1}{\frac{C_{B^{n+}}C_A^{n/m}\beta}{C_{B(A)^{n+}_{n/m}}\,C_0^{n/m}}} + \frac{C_A^{n/m}\beta}{C_0^{n/m}}\right)\right) \\
&= E^\circ - \frac{RT}{nF}\ln\left(\frac{C_0}{B_0}\left(1 + \frac{C_A^{n/m}\beta}{C_0^{n/m}}\right)\right) \\
&= E^\circ - \frac{RT}{nF}\ln\left(\frac{C_0}{B_0}\left(1 + \frac{\beta}{C_0^{n/m}}\left(\frac{A_0 - \frac{n}{m}B_0 + \frac{n}{m}C_{B^{n+}}}{1 + K_{CO_2}\left(\frac{P_{CO_2}}{P_0}\right)^m}\right)^{n/m}\right)\right) \\
&= E^\circ - \frac{RT}{nF}\ln\left(\frac{C_0}{B_0}\left(1 + \frac{\beta}{C_0^{n/m}}\left(\frac{A_0 - \frac{n}{m}B_0 + \cancelto{0}{\frac{n}{m}C_{B^{n+}}}}{1 + K_{CO_2}\left(\frac{P_{CO_2}}{P_0}\right)^m}\right)^{n/m}\right)\right) \\
&\approx E^\circ - \frac{RT}{nF}\ln\left(\frac{C_0}{B_0}\left(1 + \frac{\beta}{C_0^{n/m}}\left(\frac{A_0 - \frac{n}{m}B_0}{1 + K_{CO_2}\left(\frac{P_{CO_2}}{P_0}\right)^m}\right)^{n/m}\right)\right)
\end{aligned}
$$

$$\begin{aligned}
E &\approx E^{\circ} - \frac{RT}{nF} \ln \left(\frac{C_0}{B_0} \left(1 + \frac{\beta}{C_0^{n/m}} \left(\frac{A_0 - \frac{n}{m} B_0}{1 + K_{CO_2} \left(\frac{P_{CO_2}}{P_0} \right)^m} \right)^{n/m} \right) \right) \\
&\approx E^{\circ} - \frac{RT}{nF} \ln \left(\frac{C_0}{B_0} \left(1 + \beta \left(\left(\frac{A_0}{C_0} \right) \frac{1 - x_B}{1 + K_{CO_2} \left(\frac{P_{CO_2}}{P_0} \right)^m} \right)^{n/m} \right) \right) \\
&\approx E^{\circ} - \frac{RT}{nF} \ln \left(\frac{C_0}{B_0} \left(1 + \beta \left(\left(\frac{A_0}{C_0} \right) \frac{1 - x_B}{1 + K_{CO_2} \left(\frac{P_{CO_2}}{P_0} \right)^m} \right)^{n/m} \right) \right) \\
&\approx E^{\circ} - \frac{RT}{nF} \left[\ln \left(\frac{C_0}{B_0} \right) + \ln \left(1 + \beta \left(\left(\frac{A_0}{C_0} \right) \frac{1 - x_B}{1 + K_{CO_2} \left(\frac{P_{CO_2}}{P_0} \right)^m} \right)^{n/m} \right) \right] \\
&\approx E^{\circ} + \frac{RT}{nF} \left[\ln \left(\frac{B_0}{C_0} \right) - \ln \left(1 + \beta \left(\left(\frac{A_0}{C_0} \right) \frac{1 - x_B}{1 + K_{CO_2} \left(\frac{P_{CO_2}}{P_0} \right)^m} \right)^{n/m} \right) \right] \\
&\approx E^{\circ} + \frac{RT}{nF} \left[\ln \left(\frac{nB_0}{mA_0} \frac{mA_0}{nC_0} \right) - \ln \left(1 + \beta \left(\left(\frac{A_0}{C_0} \right) \frac{1 - x_B}{1 + K_{CO_2} \left(\frac{P_{CO_2}}{P_0} \right)^m} \right)^{n/m} \right) \right] \\
&\approx E^{\circ} + \frac{RT}{nF} \left[\ln (x_B) + \ln \left(\frac{mA_0}{nC_0} \right) - \ln \left(1 + \beta \left(\left(\frac{A_0}{C_0} \right) \frac{1 - x_B}{1 + K_{CO_2} \left(\frac{P_{CO_2}}{P_0} \right)^m} \right)^{n/m} \right) \right]
\end{aligned}$$

$$\begin{aligned}
E &= E^0 + \frac{RT}{nF} \left[\ln (x_B) + \ln \left(\frac{mA_0}{nC_0} \right) - \ln \left(1 + \beta \left(\left(\frac{A_0}{C_0} \right) \frac{1 - x_B}{1 + K_{CO_2} \left(\frac{P_{CO_2}}{P_0} \right)^m} \right)^{n/m} \right) \right] \\
&= E^0 + \frac{RT}{nF} \left[\ln (x_B) + \ln \left(\frac{mA_0}{nC_0} \right) - \ln \left(1 + \frac{\beta \left(\frac{A_0}{C_0} \right)^{n/m} (1 - x_B)^{n/m}}{\left(1 + K_{CO_2} \left(\frac{P_{CO_2}}{P_0} \right)^m \right)^{n/m}} \right) \right] \\
&= E^0 + \frac{RT}{nF} \left[\ln (x_B) + \ln \left(\frac{mA_0}{nC_0} \right) - \ln \left(\frac{\left(1 + K_{CO_2} \left(\frac{P_{CO_2}}{P_0} \right)^m \right)^{n/m} + \beta \left(\frac{A_0}{C_0} \right)^{n/m} (1 - x_B)^{n/m}}{\left(1 + K_{CO_2} \left(\frac{P_{CO_2}}{P_0} \right)^m \right)^{n/m}} \right) \right]
\end{aligned}$$

$$
\begin{aligned}
E - E_0 &= E - E|_{P_{CO_2}=0} \\
&= \left(E^0 + \frac{RT}{nF}\left[\ln(x_B) + \ln\left(\frac{mA_0}{nC_0}\right) - \ln\left(\frac{\left(1+K_{CO_2}\left(\frac{P_{CO_2}}{P_0}\right)^m\right)^{n/m} + \beta\left(\frac{A_0}{C_0}\right)^{n/m}(1-x_B)^{n/m}}{\left(1+K_{CO_2}\left(\frac{P_{CO_2}}{P_0}\right)^m\right)^{n/m}}\right)\right]\right) \\
&\quad - \left(E^0 + \frac{RT}{nF}\left[\ln(x_B) + \ln\left(\frac{mA_0}{nC_0}\right) - \ln\left(1+\beta\left(\frac{A_0}{C_0}\right)^{n/m}(1-x_B)^{n/m}\right)\right]\right) \\
&= \frac{RT}{nF}\left[\ln\left(1+\beta\left(\frac{A_0}{C_0}\right)^{n/m}(1-x_B)^{n/m}\right) - \ln\left(\frac{\left(1+K_{CO_2}\left(\frac{P_{CO_2}}{P_0}\right)^m\right)^{n/m} + \beta\left(\frac{A_0}{C_0}\right)^{n/m}(1-x_B)^{n/m}}{\left(1+K_{CO_2}\left(\frac{P_{CO_2}}{P_0}\right)^m\right)^{n/m}}\right)\right. \\
&= \frac{RT}{nF}\ln\left(\frac{\left(1+\beta\left(\frac{A_0}{C_0}\right)^{n/m}(1-x_B)^{n/m}\right)\left(1+K_{CO_2}\left(\frac{P_{CO_2}}{P_0}\right)^m\right)^{n/m}}{\left(1+K_{CO_2}\left(\frac{P_{CO_2}}{P_0}\right)^m\right)^{n/m} + \beta\left(\frac{A_0}{C_0}\right)^{n/m}(1-x_B)^{n/m}}\right) \\
&= -\frac{RT}{nF}\ln\left(\frac{\left(1+K_{CO_2}\left(\frac{P_{CO_2}}{P_0}\right)^m\right)^{n/m} + \beta\left(\frac{A_0}{C_0}\right)^{n/m}(1-x_B)^{n/m}}{\left(1+\beta\left(\frac{A_0}{C_0}\right)^{n/m}(1-x_B)^{n/m}\right)\left(1+K_{CO_2}\left(\frac{P_{CO_2}}{P_0}\right)^m\right)^{n/m}}\right) \\
&= -\frac{RT}{nF}\ln\left(\frac{\left(1+K_{CO_2}\left(\frac{P_{CO_2}}{P_0}\right)^m\right)^{n/m}}{\left(1+\beta\left(\frac{A_0}{C_0}\right)^{n/m}(1-x_B)^{n/m}\right)\left(1+K_{CO_2}\left(\frac{P_{CO_2}}{P_0}\right)^m\right)^{n/m}}\right. \\
&\quad \left. + \frac{\beta\left(\frac{A_0}{C_0}\right)^{n/m}(1-x_B)^{n/m}}{\left(1+\beta\left(\frac{A_0}{C_0}\right)^{n/m}(1-x_B)^{n/m}\right)\left(1+K_{CO_2}\left(\frac{P_{CO_2}}{P_0}\right)^m\right)^{n/m}}\right) \\
&= -\frac{RT}{nF}\ln\left(\frac{1}{1+\beta\left(\frac{A_0}{C_0}\right)^{n/m}(1-x_B)^{n/m}} + \frac{\beta\left(\frac{A_0}{C_0}\right)^{n/m}(1-x_B)^{n/m}}{\left(1+\beta\left(\frac{A_0}{C_0}\right)^{n/m}(1-x_B)^{n/m}\right)\left(1+K_{CO_2}\left(\frac{P_{CO_2}}{P_0}\right)^m\right)^{n/m}}\right)
\end{aligned}
$$

$\beta \gg 1$, $\frac{A_0}{C_0} \sim 1$, $1 - x_B \sim 1$ therefore

$$
\beta\left(\frac{A_0}{C_0}\right)^{n/m}(1-x_B)^{n/m} \gg 1
$$

$$
\begin{aligned}
E - E_0 &= E - \left.E\right|_{P_{CO_2}=0} \\
&= -\frac{RT}{nF}\ln\left(\cancelto{0}{\frac{1}{\beta\left(\frac{A_0}{C_0}\right)^{n/m}(1-x_B)^{n/m}}} + \frac{\beta\left(\frac{A_0}{C_0}\right)^{n/m}(1-x_B)^{n/m}}{\beta\left(\frac{A_0}{C_0}\right)^{n/m}(1-x_B)^{n/m}\left(1+K_{CO_2}\left(\frac{P_{CO_2}}{P_0}\right)^{m}\right)^{n/m}}\right) \\
&= -\frac{RT}{nF}\ln\left(\frac{1}{\left(1+K_{CO_2}\left(\frac{P_{CO_2}}{P_0}\right)^{m}\right)^{n/m}}\right) \\
&= \frac{RT}{nF}\ln\left(\left(1+K_{CO_2}\left(\frac{P_{CO_2}}{P_0}\right)^{m}\right)^{n/m}\right) \\
&= \frac{RT}{mF}\ln\left(1+K_{CO_2}\left(\frac{P_{CO_2}}{P_0}\right)^{m}\right)
\end{aligned}
$$

CO_2 Mass Balance

$$A_0 = C_A + C_{A(CO_2)_m} + \frac{n}{m}C_{B(A)_{n/m}}$$

$$B_0 = C_{B^{n+}} + C_{B(A)_{n/m}^{n+}} \approx C_{B(A)_{n/m}^{n+}}$$

$$x_B = \frac{nC_{B(A)_{n/m}}}{mA_0} \approx \frac{nB_0}{mA_0}$$

$$CO_{2,0} = C_{CO_2} + mC_{A(CO_2)_m}$$

$$P_{CO_2} = \frac{C_{CO_2}}{k_{h,CO_2}}$$

$$x_{CO_{2,0}} = \frac{CO_{2,0}}{mA_0}$$

$$\begin{aligned}
K_{CO_2} &= \frac{C_{A(CO_2)_m}}{C_A}\left(\frac{P_0}{P_{CO_2}}\right)^m \\
&= \frac{C_{A(CO_2)_m}}{A_0 - \left(C_{A(CO_2)_m} + \frac{n}{m} C_{B(A)_{n/m}}\right)}\left(\frac{P_0}{P_{CO_2}}\right)^m \\
&= \frac{C_{A(CO_2)_m}}{A_0 - \left(C_{A(CO_2)_m} + x_B A_0\right)}\left(\frac{P_0}{P_{CO_2}}\right)^m \\
&= \frac{C_{A(CO_2)_m}}{\left(1 - x_B\right) A_0 - C_{A(CO_2)_m}}\left(\frac{P_0}{P_{CO_2}}\right)^m
\end{aligned}$$

$$\left(\left(1 - x_B\right) A_0 - C_{A(CO_2)_m}\right) K_{CO_2}\left(\frac{P_{CO_2}}{P_0}\right)^m = C_{A(CO_2)_m}$$

$$\left(1 - x_B\right) A_0 K_{CO_2}\left(\frac{P_{CO_2}}{P_0}\right)^m = \left(1 + K_{CO_2}\left(\frac{P_{CO_2}}{P_0}\right)^m\right) C_{A(CO_2)_m}$$

$$C_{A(CO_2)_m} = \left(1 - x_B\right) A_0 \frac{K_{CO_2}\left(\frac{P_{CO_2}}{P_0}\right)^m}{1 + K_{CO_2}\left(\frac{P_{CO_2}}{P_0}\right)^m}$$

$$\begin{aligned}
CO_{2,0} &= C_{CO_2} + m C_{A(CO_2)_m} \\
&= m\left(1 - x_B\right) A_0 \frac{K_{CO_2}\left(\frac{P_{CO_2}}{P_0}\right)^m}{1 + K_{CO_2}\left(\frac{P_{CO_2}}{P_0}\right)^m} + k_{h,CO_2} P_{CO_2}
\end{aligned}$$

$$x_{CO_{2,0}} = \left(1 - x_B\right) \frac{K_{CO_2}\left(\frac{P_{CO_2}}{P_0}\right)^m}{1 + K_{CO_2}\left(\frac{P_{CO_2}}{P_0}\right)^m} + \frac{k_{h,CO_2} P_{CO_2}}{m A_0}$$

Cell Potential from Deviation Potential

$$\begin{aligned}
\Delta E &= E_{anode} - E_{cathode} \\
&= \left(\frac{RT}{mF} \ln \left(1 + K_{CO_2} \left(\frac{P_{CO_2,anode}}{P_0} \right)^m \right) + E|_{P_{CO_2}=0} \right) \\
&\quad - \left(\frac{RT}{mF} \ln \left(1 + K_{CO_2} \left(\frac{P_{CO_2,cathode}}{P_0} \right)^m \right) + E|_{P_{CO_2}=0} \right) \\
&= \frac{RT}{mF} \left[\ln \left(1 + K_{CO_2} \left(\frac{P_{CO_2,anode}}{P_0} \right)^m \right) - \ln \left(1 + K_{CO_2} \left(\frac{P_{CO_2,cathode}}{P_0} \right)^m \right) \right] \\
&= \frac{RT}{mF} \ln \left(\frac{1 + K_{CO_2} \left(\frac{P_{CO_2,anode}}{P_0} \right)^m}{1 + K_{CO_2} \left(\frac{P_{CO_2,cathode}}{P_0} \right)^m} \right)
\end{aligned}$$

THIS PAGE INTENTIONALLY LEFT BLANK

Appendix C

EMAR Thermodynamic Derivations

Relationship Between Key Process Variables

Consider the following three definitions (Am_0, x_{Cu}, $x_{CO_{2,0}}$) and two equilibrium relationships (K_{CO_2}, P_{CO_2}).

$$Am_0 = C_{Am(CO_2)_m} + C_{Am} + \frac{2}{m} C_{CuAm^{2+}_{2/m}} \tag{C.1}$$

$$x_{Cu} = \frac{2C_{CuAm^{2+}_{2/m}}}{mAm_0} \tag{C.2}$$

$$x_{CO_{2,0}} = \frac{C_{CO_2} + mC_{Am(CO_2)_m}}{mAm_0} = \frac{CO_{2,0}}{mAm_0} \tag{C.3}$$

$$K_{CO_2} = \frac{C_{Am(CO_2)_m}}{C_{Am}} \left(\frac{P_0}{P_{CO_2}}\right)^m \tag{C.4}$$

$$P_{CO_2} = \frac{C_{CO_2}}{k_{H,CO_2}} \tag{C.5}$$

Combining equations C.1 and C.2, we have

$$1 - x_{Cu} = \frac{C_{Am(CO_2)_m} + C_{Am}}{Am_0}$$

Substituting in equation C.4

$$\begin{aligned} 1 - x_{Cu} &= \frac{C_{Am(CO_2)_m} + \frac{C_{Am(CO_2)_m}}{K_{CO_2}} \left(\frac{P_0}{P_{CO_2}} \right)^m}{Am_0} \\ &= \frac{C_{Am(CO_2)_m}}{Am_0} \left(1 + \frac{P_0^m}{K_{CO_2} P_{CO_2}^m} \right) \\ &= \frac{C_{Am(CO_2)_m}}{Am_0} \left(\frac{K_{CO_2} P_{CO_2}^m + P_0^m}{K_{CO_2} P_{CO_2}^m} \right) \end{aligned}$$

Combining equations C.3 and C.5, we have

$$x_{CO_{2,0}} = \frac{k_{H,CO_2} P_{CO_2} + m C_{Am(CO_2)_m}}{m Am_0} = \frac{k_{H,CO_2} P_{CO_2}}{m Am_0} + \frac{C_{Am(CO_2)_m}}{Am_0}$$

Combining the two above equations, we have

$$1 - x_{Cu} = \left(x_{CO_{2,0}} - \frac{k_{H,CO_2} P_{CO_2}}{m Am_0} \right) \left(\frac{K_{CO_2} P_{CO_2}^m + P_0^m}{K_{CO_2} P_{CO_2}^m} \right)$$

$$x_{CO_{2,0}} - \frac{k_{H,CO_2} P_{CO_2}}{m Am_0} = (1 - x_{Cu}) \left(\frac{K_{CO_2} P_{CO_2}^m}{K_{CO_2} P_{CO_2}^m + P_0^m} \right)$$

Define $\tilde{k}_{h,CO_2} = \frac{k_{h,CO_2} P_0}{m Am_0}$

$$x_{CO_{2,0}} - \tilde{k}_{h,CO_2} \left(\frac{P_{CO_2}}{P_0} \right) = (1 - x_{Cu}) \left(\frac{K_{CO_2} P^m_{CO_2}}{K_{CO_2} P^m_{CO_2} + P_0^m} \right)$$

Define $\tilde{P}_{CO_2} = \frac{P_{CO_2}}{P_0}$

$$x_{CO_{2,0}} - \tilde{k}_{h,CO_2} \tilde{P}_{CO_2} = (1 - x_{Cu}) \left(\frac{K_{CO_2} \tilde{P}^m_{CO_2}}{1 + K_{CO_2} \tilde{P}^m_{CO_2}} \right) \tag{C.6}$$

This equation C.6 gives a relation between $x_{CO_{2,0}}$, x_{Cu}, and $\tilde{P}_{CO_2}$. If $x_{CO_{2,0}}$ or x_{Cu} are unknown equations C.7 and C.8 respectively may be used.

$$x_{CO_{2,0}} = (1 - x_{Cu}) \left(\frac{K_{CO_2} \tilde{P}^m_{CO_2}}{1 + K_{CO_2} \tilde{P}^m_{CO_2}} \right) + \tilde{k}_{h,CO_2} \tilde{P}_{CO_2} \tag{C.7}$$

$$x_{Cu} = 1 - \left(x_{CO_{2,0}} - \tilde{k}_{h,CO_2} \tilde{P}_{CO_2} \right) \left(\frac{1 + K_{CO_2} \tilde{P}^m_{CO_2}}{K_{CO_2} \tilde{P}^m_{CO_2}} \right) \tag{C.8}$$

An analytical solution for $\tilde{P}_{CO_2}$ exists for $m = 1$.

$$x_{CO_{2,0}} - \tilde{k}_{h,CO_2} \tilde{P}_{CO_2} = (1 - x_{Cu}) \left(\frac{K_{CO_2} \tilde{P}_{CO_2}}{1 + K_{CO_2} \tilde{P}_{CO_2}} \right)$$

$$\left(x_{CO_{2,0}} - \tilde{k}_{h,CO_2} \tilde{P}_{CO_2} \right) \left(1 + K_{CO_2} \tilde{P}_{CO_2} \right) = K_{CO_2} \left(1 - x_{Cu} \right) \tilde{P}_{CO_2}$$

$$x_{CO_{2,0}} \left(1 + K_{CO_2} \tilde{P}_{CO_2} \right) - \tilde{k}_{h,CO_2} \tilde{P}_{CO_2} \left(1 + K_{CO_2} \tilde{P}_{CO_2} \right) = K_{CO_2} \left(1 - x_{Cu} \right) \tilde{P}_{CO_2}$$

$$x_{CO_{2,0}} + x_{CO_{2,0}} K_{CO_2} \tilde{P}_{CO_2} - \tilde{k}_{h,CO_2} \tilde{P}_{CO_2} - \tilde{k}_{h,CO_2} K_{CO_2} \tilde{P}^2_{CO_2} = K_{CO_2} \left(1 - x_{Cu} \right) \tilde{P}_{CO_2}$$

$$x_{CO_{2,0}} + \left(x_{CO_{2,0}} K_{CO_2} - \tilde{k}_{h,CO_2}\right) \tilde{P}_{CO_2} - \tilde{k}_{h,CO_2} K_{CO_2} \tilde{P}^2_{CO_2} = K_{CO_2} \left(1 - x_{Cu}\right) \tilde{P}_{CO_2}$$

$$0 = \tilde{k}_{h,CO_2} K_{CO_2} \tilde{P}^2_{CO_2} + \left(K_{CO_2} \left(1 - x_{Cu}\right) - \left(x_{CO_{2,0}} K_{CO_2} - \tilde{k}_{h,CO_2}\right)\right) \tilde{P}_{CO_2} - x_{CO_{2,0}}$$

$$0 = \tilde{k}_{h,CO_2} K_{CO_2} \tilde{P}^2_{CO_2} + \left(K_{CO_2} \left(1 - x_{Cu} - x_{CO_{2,0}}\right) + \tilde{k}_{h,CO_2}\right) \tilde{P}_{CO_2} - x_{CO_{2,0}}$$

Define $b = K_{CO_2} \left(1 - x_{Cu} - x_{CO_{2,0}}\right) + \tilde{k}_{h,CO_2}$

$$0 = \tilde{k}_{h,CO_2} K_{CO_2} \tilde{P}^2_{CO_2} + b\tilde{P}_{CO_2} - x_{CO_{2,0}}$$

$$\tilde{P}_{CO_2} = \frac{-b \pm \sqrt{b^2 + 4\tilde{k}_{h,CO_2} K_{CO_2} x_{CO_{2,0}}}}{2\tilde{k}_{h,CO_2} K_{CO_2}}$$

Notice $4\tilde{k}_{h,CO_2} K_{CO_2} x_{CO_{2,0}} > 0$, so one root,$-b + \sqrt{b^2 + 4\tilde{k}_{h,CO_2} K_{CO_2} x_{CO_{2,0}}} > 0$, is positive, whereas the second root, $-b - \sqrt{b^2 + 4\tilde{k}_{h,CO_2} K_{CO_2} x_{CO_{2,0}}} < 0$, is negative. Ignore the non-physical, negative root.

$$\tilde{P}_{CO_2} = \frac{\sqrt{b^2 + 4\tilde{k}_{h,CO_2} K_{CO_2} x_{CO_{2,0}}} - b}{2\tilde{k}_{h,CO_2} K_{CO_2}} \tag{C.9}$$

Minimum Required Copper Loading Shift and Maximum Desorption Pressure

As discussed in Section 3, a minimum required copper loading shift exists for a desired desorption pressure, or similarly a maximum desorption pressure exists for a given copper loading shift. Equation 3.5 describes this relationship and is repeated below for convenience.

$$\begin{aligned}(1 - x_{Cu,in}) \left(\tfrac{K_{CO_2}\tilde{P}^m_{abs}}{1+K_{CO_2}\tilde{P}^m_{abs}}\right) + \tilde{k}_{h,CO_2}\tilde{P}_{abs} \\ > (1 - x_{Cu,out}) \left(\tfrac{K_{CO_2}\tilde{P}^m_{EMAR}}{1+K_{CO_2}\tilde{P}^m_{EMAR}}\right) + \tilde{k}_{h,CO_2}\tilde{P}_{EMAR}\end{aligned} \tag{C.10}$$

For simplicity, define the following:

$$\begin{aligned} a_{abs} &= \tfrac{K_{CO_2}\tilde{P}^m_{abs}}{1+K_{CO_2}\tilde{P}^m_{abs}} \qquad & a_{EMAR} &= \tfrac{K_{CO_2}\tilde{P}^m_{EMAR}}{1+K_{CO_2}\tilde{P}^m_{EMAR}} \\ b_{abs} &= \tilde{k}_{h,CO_2}\tilde{P}_{abs} \qquad & b_{EMAR} &= \tilde{k}_{h,CO_2}\tilde{P}_{EMAR}\end{aligned}$$

$$\Delta x_{Cu} = x_{Cu,out} - x_{Cu,in}$$

Substituting these definitions into equation C.10, we have

$$(1 - x_{Cu,in})\, a_1 + b_1 > (1 - x_{Cu,out})\, a_2 + b_2$$

$$(1 - x_{Cu,in})\, a_1 + b_1 > (1 - (x_{Cu,in} + \Delta x_{Cu}))\, a_2 + b_2$$

$$\Delta x_{Cu} > (1 - x_{Cu,in})\, \frac{a_2 - a_1}{a_2} + \frac{b_2 - b_1}{a_2}$$

Returning to the original variable set, we have

$$\Delta x_{Cu} > (1 - x_{Cu,in}) \frac{\left(\frac{K_{CO_2}\tilde{P}^m_{EMAR}}{1+K_{CO_2}\tilde{P}^m_{EMAR}}\right) - \left(\frac{K_{CO_2}\tilde{P}^m_{abs}}{1+K_{CO_2}\tilde{P}^m_{abs}}\right)}{\left(\frac{K_{CO_2}\tilde{P}^m_{EMAR}}{1+K_{CO_2}\tilde{P}^m_{EMAR}}\right)} + \frac{\tilde{k}_{h,CO_2}\tilde{P}_{EMAR} - \tilde{k}_{h,CO_2}\tilde{P}_{abs}}{\left(\frac{K_{CO_2}\tilde{P}^m_{EMAR}}{1+K_{CO_2}\tilde{P}^m_{EMAR}}\right)}$$

$$\begin{gathered}\Delta x_{Cu} > (1 - x_{Cu,in}) \left(1 - \left(\frac{\tilde{P}^m_{abs}}{\tilde{P}^m_{EMAR}}\right)\left(\frac{1+K_{CO_2}\tilde{P}^m_{EMAR}}{1+K_{CO_2}\tilde{P}^m_{abs}}\right)\right) \\ +\tilde{k}_{h,CO_2}\frac{1+K_{CO_2}\tilde{P}^m_{EMAR}}{K_{CO_2}\tilde{P}^m_{EMAR}}\left(\tilde{P}_{EMAR} - \tilde{P}_{abs}\right)\end{gathered}$$

For typical EMAR conditions, $1 \ll K_{CO_2}\tilde{P}^m_{abs} < K_{CO_2}\tilde{P}^m_{EMAR}$. Therefore, we may make the following simplifications

$$\begin{gathered}\Delta x_{Cu} \gtrapprox (1 - x_{Cu,in}) \left(1 - \left(\frac{\tilde{P}^m_{abs}}{\tilde{P}^m_{EMAR}}\right)\left(\frac{K_{CO_2}\tilde{P}^m_{EMAR}}{K_{CO_2}\tilde{P}^m_{abs}}\right)\right) \\ +\tilde{k}_{h,CO_2}\frac{K_{CO_2}\tilde{P}^m_{EMAR}}{K_{CO_2}\tilde{P}^m_{EMAR}}\left(\tilde{P}_{EMAR} - \tilde{P}_{abs}\right)\end{gathered}$$

$$\Delta x_{Cu} \gtrapprox \tilde{k}_{h,CO_2}\left(\tilde{P}_{EMAR} - \tilde{P}_{abs}\right) \tag{C.11}$$